Magneto Optical Trapping of Potassium-39 in a Ring Cavity

by

Komal Pahwa

A thesis submitted to
The University of Birmingham
for the degree of
DOCTOR OF PHILOSOPHY

Midlands Ultracold Atom Research Center
School of Physics and Astronomy
College of Engineering and Physical Sciences
The University of Birmingham

November 2014

Abstract

This thesis focuses on the construction and development of an experiment to study cold potassium atoms in an optical ring cavity. Firstly we load a potassium-39 magneto optical trap (MOT) inside the ring cavity. To achieve this a laser system, rectangular magnetic coils system and vacuum system are designed and constructed. To stabilise the laser system, a detailed study of various potassium spectroscopy techniques is undertaken and the reference laser is suitably locked to the magnetically induced spectroscopy.

We load an ensemble of $\sim 10^5$ potassium atoms inside the ring cavity mode and study their collective strong coupling with the cavity field. In the collective strong coupling regime, the photons are coherently exchanged between the atomic ensemble and cavity field. This rate of exchange is determined by the single-photon Rabi frequency '$2g$' which must be larger than the cavity field decay rate '2κ' and atomic spontaneous emission rate '2γ'. As a result of this coupling, the peak in the cavity transmission signal undergoes a splitting known as 'vacuum Rabi splitting' (or 'normal mode splitting'). The vacuum Rabi splitting has been realised and measured to be $\sim 2\pi \cdot 18$ MHz in our system.

Dedicated to my loving parents

ACKNOWLEDGEMENTS

I would first like to thank my supervisor, Dr. Jon Goldwin and the head of our group Prof. Kai Bongs for giving me the opportunity to work in this group. Jon is a terrific supervisor and he has been a constant source of inspiration for me during my PhD time. Thank you Jon for introducing me to the cold atoms field in general, as well as teaching me many useful lab skills. I am really grateful to you for your guidance, support and endless patience to answer all my questions.

Next person to thank is my labmate Lawrence Mudarikwa. Lawrence, we started our PhD at the same time and have spent a few years working together in the same lab. Thanks for being there to teach me about different types of high protein foods and work-out strategies. Jokes apart, your hard work on optical cavities was a major contribution to the experiment. By the way, I still remember your favorite tool in the lab.

Rob and Andreas, you are lovely labmates and I am sure you will take the experiment forward from this stage. I am also thankful to the whole research group for being so helpful and making these years a wonderful experience in my life.

I am very thankful to Chris Embry and Jon again for carefully reading my thesis and giving their useful suggestions and thoughts.

And last but not least, I would like to express my deepest gratitude to my amazing mother for encouraging me to pursue my academic goals at the University of Birmingham and being my moral support throughout this journey. Mummy I know you are dying to see me, don't worry I will be back soon. I am also very grateful to my father, sister and brother-in-law for always being there by my side.

CONTENTS

LIST OF FIGURES

LIST OF TABLES

CHAPTER 1

INTRODUCTION

1.1 Overview

Cavity quantum electrodynamics (QED) is at the heart of quantum mechanics and has been a great tool to explore its fundamentals [55]. For more than 30 years, it has been a subject of great interest for physicists with a wide range of applications in precision metrology and inertial sensing, cavity assisted cooling of atomic/molecular species, atom lasers, quantum memories, quantum computation and so on. The main focus of this experiment is to study the interactions of ultra cold potassium-39 (^{39}K) atoms with the light field inside a medium finesse ($F = 2100$) ring shaped optical cavity in the collective strong coupling regime of cavity QED. This thesis describes the design and construction of the experiment to load a potassium-39 magneto optical trap (MOT) at the center of cavity waist, and the observation of the vacuum Rabi splitting in the ring cavity. The occurrence of vacuum Rabi splitting is a bench-mark for the collective strong coupling regime. It was first observed in optical cavities, for an atomic ensemble in the year 1989 [80] and then later for very few atoms (N$\leq$10) in 1992 [95].

The driving idea behind this experiment is to study the collective strong coupling of the cold ensemble of ^{39}K atoms with ring cavity field. Further, this set-up can be used as a test bed to explore cavity mediated cooling techniques. Cavity cooling is based on the polarisability of the species to be cooled and not on its internal energy level structure. Hence it is very appealing idea for cooling molecules (having multiple vibrational and rotational levels) and species that can not be cooled by normal Doppler cooling techniques.

1.1.1 Why atoms in a cavity?

In free space, the probability of an atom to scatter a single photon in a laser light field is typically very small. The probability of a second scattering event involving the same atom and photon is negligible. Hence the modification of the laser light field (such as change in amplitude and/or phase) due to the back-action of atoms is too small to be observed.

By confining the laser light field in a cavity, the intracavity intensity is enhanced due to multiple reflections from the cavity mirrors and hence the dipole force on the atoms present inside the cavity is significantly enhanced. In addition to that the back action of atomic motion onto the light field is enhanced. Such a system gives rise to a non linear coupled dynamics, [101] where the dipole force on the atoms is non-conservative [43] because the optical cavity acts as an open, damped and driven system. This non-conservative dynamics is a useful tool to cool and confine the atomic motion (a phenomenon known as cavity cooling).

For an ensemble of atoms, long range interactions among atoms can be realised in an optical cavity, leading to collective effects. Based on long range atomic interactions, different collective phenomena e.g. correlated atomic motion, Dicke's sub or super-radiance[25], atomic self-organisation [88, 10] have already been realised in cavities.

Another very important feature of cavities is that they are a useful tool to modify the weak or strong coupling between atoms and light. In the weak coupling regime, the well known Purcell effect [77] demonstrates the modification of atomic spontaneous emission inside the cavity. In strong coupling regime the exchange of photons between atom and light field is a coherent and reversible process and is dominant over the dissipative effects. Furthermore, the real time non-destructive detection of atomic dynamics is possible in cavities via monitoring reflection or transmission signals [42].

1.1.2 Why Ring cavity?

In the present experiment we are using a cavity with ring shaped geometry to explore the dynamics of atom-light field system. Firstly, I will describe how a ring cavity is different from a linear cavity (or Fabry Pérot cavity). In a linear cavity formed of two mirrors (see figure 1.1(a)), a light field in resonance with the cavity mode forms a standing wave inside it. The resonance condition is given by: $2L = n\lambda$ where n is an integer, L is the length of the cavity and λ is the wavelength of the light field entering the cavity. The standing wave inside the linear cavity is stationary or in other words it has a fixed spatial phase due to boundary conditions at the dielectric mirrors. Hence, a linear cavity supports only one of the two standing wave modes, either sine or cosine. The standing wave modes are different from cavity transverse and longitudinal modes and

should not be confused with these.

In a three mirror ring cavity as shown in figure 1.1(b), the laser beam can be pumped in from two different paths and they travel in opposite directions inside the cavity. Also, there are two separate outgoing paths for these two oppositely traveling light fields which can be used for detection purposes. A ring resonator supports pairs of counter-propagating traveling wave modes (clockwise and counter-clockwise) or standing wave modes (sine and cosine). This is the main motivation to work with ring cavities. Each of these two counter-propagating modes can have their own photons separately. The counter-propagating modes of a ring cavity can be coupled due to the coherent scattering of photons by atoms from one mode to another.

In general, when an atom is interacting with a standing wave field in free space, the field affects the motion of the atom. In return, the back actions of atomic motion can change the intensity and phase of the standing wave field. In a linear resonator only the intensity is modified because the spatial phase of the standing wave has to be fixed by boundary conditions at the mirrors at all times. Whereas, in the case of a ring cavity, both the phase and intensity can be changed. This unique feature of standing wave phase shift caused by atomic back action in the ring cavities can lead to many useful phenomena such as collective atom recoil lasing (CARL) [21], spatial atomic self-organisation, optical bistability [28] and Dicke super- and sub-radiant scattering [88].

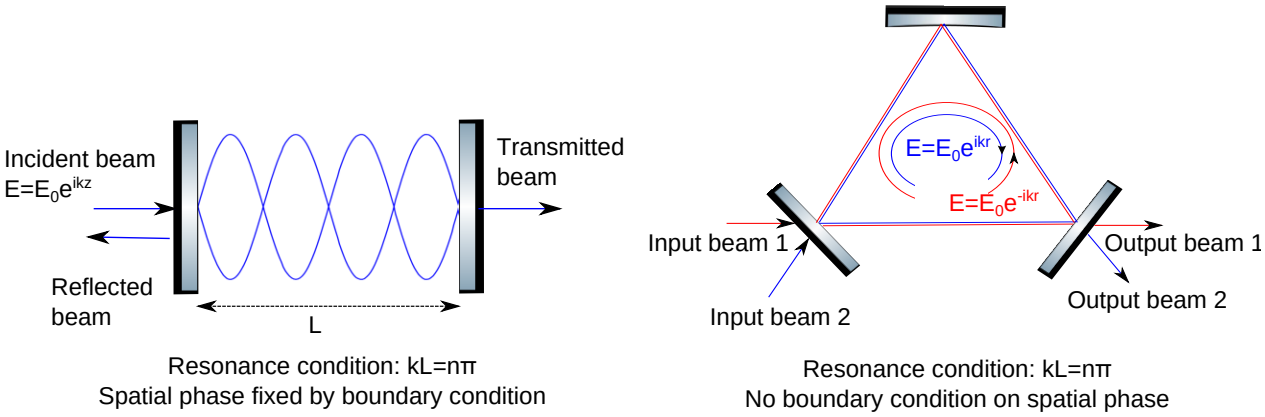

Figure 1.1: (a) A two mirror linear cavity illustrating a standing wave mode inside it. (b) A three mirror ring cavity with two incoming beams travelling in the opposite directions and two outgoing beams. The CW and CCW traveling wave modes are represented by blue and red colour respectively.

1.1.3 Thesis outline

We have already discussed the usefulness of ring cavities over linear cavities in the first section of this introduction chapter. The second section 1.2 focuses on the fundamentals of cavity QED. In this section

the simplest model of atom-cavity system known as Jaynes-Cummings model and single atom-cavity strong coupling regime are described. After this, the collective strong coupling of ensemble of N atoms with the cavity field is explained. Following that our ring cavity design and experimental parameters to achieve the collective strong coupling are discussed. Section 1.3 throws light on the basic idea of cavity cooling and theoretical predictions of enhanced cooling in our ring cavity system. These predictions suggest that having $> 2.7 \times 10^5$ atoms collectively coupled to the cavity field along with $\sim$2.7 GHz of cavity detuning can lead to enhancement of cooling effect. In this regime, we can achieve cooling beyond what is achievable in a linear cavity with similar parameters.

Chapter 2 contains the theory of laser cooling and trapping. It also describes the geometry of our MOT, design of magnetic coil system and magnetic field gradient simulations.

In Chapter 3 the design, construction and assembly of our ultra high vacuum system is described in detail. The ring cavity is placed on the bottom flange inside the vacuum.

Chapter 4 focuses on different potassium spectroscopy methods to stabilise extended cavity diode lasers (ECDL). We perform saturated absorption spectroscopy of potassium and measure the spectra for different vapour pressure to find an optimum potassium vapour pressure for good spectroscopy. Later the study of polarisation, magnetic dichroism, direct modulation and modulation transfer spetcroscopies is described.

Chapter 5 presents the MOT laser system in detail. In the first part of this chapter, the stabilisation of cooling and repump lasers using frequency offset locking scheme is discussed. The second part focuses on tapered amplifier set-up used to amplify the cooling and repump light.

Chapter 6 describes the set up of MOT imaging system, calculations of MOT atom number and density from florescence imaging. The characterisation of MOT for the magnetic field gradient and frequency detuning of cooling are repump light are also presented.

Chapter 7 first shows the preliminary results of realisation of the vacuum Rabi splitting of $\approx 2\pi \cdot 18$ MHz in our ring cavity system. Later, a few future improvements on experimental design are suggested and finally future directions of this experiment are described.

1.2 Fundamentals of Cavity QED

1.2.1 Jaynes-Cummings Model

The field of cavity QED started with the Purcell effect in a linear cavity introduced by Purcell in 1946 [77]. He demonstrated the usefulness of a cavity to enhance the spontaneous emission rate of atoms. The electro-

magnetic mode density plays an important role in the spontaneous emission process and it can be modified by confining an atom in a resonator. There is a history of many experiments on atom light interactions in cavities, first in microwave regime [103, 79, 48, 22] in early 1980's and then later in infrared [47] and optical regimes [40].

The first theoretical model on atom light interactions in a cavity was given by Jaynes and Cummings in 1963 [46]. This model describes the interactions of a single atom with a single mode cavity field. An atom is considered as a two level system and the electromagnetic field inside the cavity acts as a single harmonic oscillator. The extension of this model from a single atom to an ensemble of N atoms in a single mode cavity was discussed by Tavis and Cummings [93, 94]. For simplicity, the driving and damping terms are not considered in this model and will be considered later in the next section. The Jaynes-Cummings hamiltonian for such a system is given by the following equation.

$$H_{\mathrm{JC}} = H_{\mathrm{atom}} + H_{\mathrm{field}} + H_{\mathrm{int}}, \tag{1.1}$$

where H_{atom} is the hamiltonian for the bare atom, H_{field} gives the energy of the single mode cavity field. The term H_{int} represents atom-light interaction hamiltonian. Now, we will calculate these hamiltonians.

Consider an atom having ground state $|g\rangle$ and excited state $|e\rangle$. The energy separation between ground and excited state is given by the term $\hbar\omega_{\mathrm{a}}$. The hamiltonian for this free atom is given as following.

$$H_{\mathrm{atom}} = \hbar\omega_{\mathrm{a}}\sigma^{+}\sigma^{-}, \tag{1.2}$$

where $\sigma^{+} = |e\rangle\langle g|$ and $\sigma^{-} = |g\rangle\langle e|$ are the atomic raising and lowing operators and are derived from Pauli spin matrices (σ_x,σ_y and σ_z).

$$\sigma^{\pm} = \frac{1}{2}(\sigma_x \pm i\sigma_y), \tag{1.3}$$

where $\sigma_x = |e\rangle\langle g| + |g\rangle\langle e|$ and $\sigma_y = -i(|e\rangle\langle g| - |g\rangle\langle e|)$. For a single mode isolated cavity, the cavity field hamiltonian is given by:

$$H_{\mathrm{field}} = \hbar\omega_{\mathrm{c}}(a^{\dagger}a + \frac{1}{2}), \tag{1.4}$$

where $a^{\dagger}$ and a are creation and annihilation operators of field respectively. Here, the cavity mode is treated as a single harmonic oscillator with frequency ω_{c}. In this hamiltonian, the term $\frac{1}{2}\hbar\omega_{\mathrm{c}}$ represents zero point energy and can be omitted. This hamiltonian does not include any external pumping or damping terms as

the model considers the atom-cavity system as a closed isolated system.

To calculate the interaction hamiltonian H_{int}, we consider that the atom is placed in a laser light field. Defining the dipole moment operator of the atom; $\vec{d} = \vec{d}_{eg}\sigma^+ + \vec{d}_{ge}\sigma^-$, where $\vec{d}_{eg} = \left\langle e|\vec{d}|g \right\rangle$. Assuming the light field as a plane wave, its electric field with polarisation $\hat{i}$ can be defined as: $\vec{E}(t) = \hat{i}\sqrt{\frac{\hbar\omega}{2\epsilon_0 V}}(ae^{i(\vec{k}\cdot\vec{r}-\omega t)} + a^\dagger e^{-i(\vec{k}\cdot\vec{r}-\omega t)})$, where ω is the frequency of the light field, $\sqrt{\frac{\hbar\omega}{2\epsilon_0 V}}$ represents the field per photon, ϵ_0 is the free space permittivity and V is the volume of the space occupied by the light field which is equivalent to the cavity mode volume in the present case. The interaction hamiltonian can be written as:

$$H_{\text{int}} = -\vec{d}\cdot\vec{E}(t). \tag{1.5}$$

In the above equation, the dipole approximation has been made. This approximation assumes that the wavelength of the light field is very large in comparison to the size of the atom (i.e. $\vec{k}\cdot\vec{r} \ll 1$) so that the phase of the electric field is almost constant over the size of the atom. Under the light of this condition the $\vec{r}$ dependence can be omitted from the hamiltonian H_{int}. Substituting the values of $\vec{d}$ and $\vec{E}$ into equation 1.5 gives:

$$H_{\text{int}} = -(\vec{d}_{eg}\sigma^+ + \vec{d}_{ge}\sigma^-).\sqrt{\frac{\hbar\omega}{2\epsilon_0 V}}(ae^{i\omega t} + a^\dagger e^{-i\omega t})\hat{i}. \tag{1.6}$$

After multiplication this hamiltonian becomes:

$$H_{\text{int}} = -\sqrt{\frac{\hbar\omega}{2\epsilon_0 V}}\left[\left\langle e|\vec{d}\cdot\hat{i}|g\right\rangle(\sigma^+ae^{-i\omega t} + \sigma^+a^\dagger e^{i\omega t}) + \left\langle g|\vec{d}\cdot\hat{i}|e\right\rangle(\sigma^-ae^{-i\omega t} + \sigma^-a^\dagger e^{i\omega t})\right]. \tag{1.7}$$

The exact solution of the above equation is difficult to calculate as it involves time dependence. We transform H_{int} into a rotating frame (or interaction picture) to eliminate the time dependence. For this a unitary transformation $H^R_{int} = U^\dagger H_{int} U$ is made, here H^R_{int} represents the interaction hamiltonian in the rotating frame and $U = e^{-iH_a t/\hbar} = e^{-i\sigma^+\sigma^-\omega_a t}$ is the unitary operator. The hamiltonian $H^{\text{R}}_{\text{int}}$ contains two pairs of exponential terms evolving at different time scales; one pair evolving slowly at frequency ($\Delta = \omega - \omega_{\text{a}}$) and another pair evolving rapidly at frequency ($\omega + \omega_{\text{a}}$). Now we make the rotating wave approximation (RWA). Assuming the light field is nearly resonant with the atomic transition which means $\Delta \ll \omega + \omega_{\text{a}}$. For this time scale, the rapidly evolving pair of terms quickly averages to zero and can be omitted from the hamiltonian $H^{\text{R}}_{\text{int}}$ which then takes the form:

$$H^{\text{R}}_{\text{int}} = -\sqrt{\frac{\hbar\omega}{2\epsilon_0 V}}\left[\left\langle e|\vec{d}\cdot\hat{i}|g\right\rangle\sigma^+ae^{-i\Delta t} + \left\langle g|\vec{d}\cdot\hat{i}|e\right\rangle\sigma^-a^\dagger e^{i\Delta t}\right]. \tag{1.8}$$

After applying another unitary transformation ($U = e^{i\sigma^+\sigma^-\Delta t}$) to eliminate the remaining time dependence, the final hamiltonian has the form:

$$H_{\text{int}} = \hbar(g\sigma^+ a + g^*\sigma^- a^\dagger). \tag{1.9}$$

Here from this equation, g is defined as the atom-cavity coupling rate and its value is:

$$g = \sqrt{\frac{\omega\mu^2}{2\hbar\epsilon_0 V}}, \tag{1.10}$$

where $\mu = \left\langle e|\vec{d}\cdot\hat{i}|g\right\rangle$ is the dipole matrix element for the transition between ground and excited states of the atom and V is the cavity mode volume. Smaller mode volumes lead to stronger atom-cavity coupling constants. Having calculated the atomic, cavity field, and interaction hamiltonians above, the Jaynes-Cumming hamiltonian takes the form as given below:

$$H_{\text{JC}} = \hbar\omega_{\text{a}}\sigma^+\sigma^- + \hbar\omega_c a^\dagger a + \hbar(g\sigma^+ a + g^*\sigma^- a^\dagger). \tag{1.11}$$

Here g is for a two-level atom and represents the maximum value of atom-field interaction. For a multi-level atom, one should take into account the Zeeman splitting of the levels involved in the transition under consideration. There are different possible transitions because of different the Zeeman levels $m_{\text{F/F'}}$ and each transition has a weighted g in accordance to Clebsch-Gordan coefficients.

Now, we take into account the dressed picture for the coupled atom-cavity system. The tensor product of bare atomic states $\{|g\rangle, |e\rangle\}$ and fock states (or number states) $\{|n\rangle\}$ of cavity field gives the complete basis set for atom-cavity system can be expressed as:

$$P = \{|g,0\rangle, |e,0\rangle, |g,1\rangle, |e,1\rangle ..., |g,n\rangle, |e,n\rangle\}, \tag{1.12}$$

where n is the number of photons in the cavity mode. For a closed atom-cavity system, the absorption (or emission) of a photon from the atom should decrease (or increase) the cavity photon number by one. This generates a ladder energy structure with doublet excited states as shown in figure 1.2. As evident from this figure, the uncoupled/bare atomic and fock states mix together to generate doublet excited states. These doublet states are generated as a result of dipole-field interactions in the cavity and this ladder of doublet states is known as the Jaynes-Cummings ladder. The ground state $|g,0\rangle$ has an energy of $\frac{1}{2}\hbar\omega_{\text{c}}$ which represents the vacuum field energy of the cavity. For an uncoupled atom-cavity system ($g = 0$), the

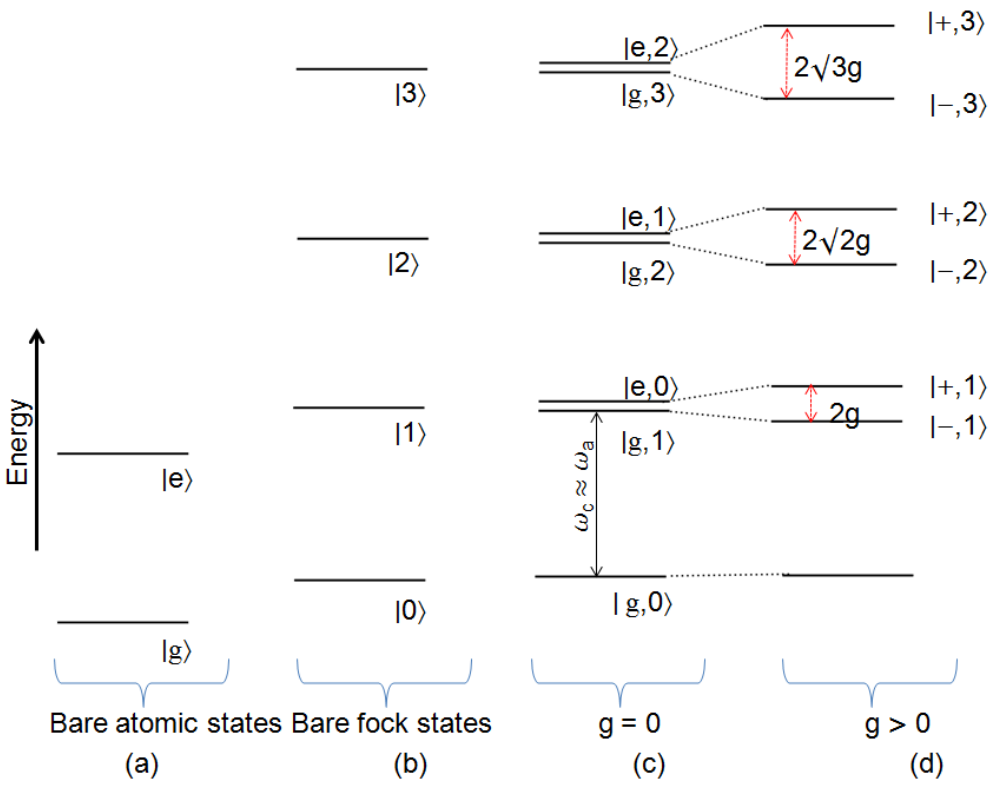

Figure 1.2: (a) The bare atomic states of a two-level atom, (b) fock/number states of the single mode cavity field having n photons. (c) A ladder of degenerate states for $g = 0$ and (d) non-degenerate states for $g > 0$ occurs because of atom-light interactions in the cavity. This is known as the Jaynes-Cummings ladder. A small splitting in the doublet excited states for $g = 0$ occurs because of non-zero detuning between atom and cavity.

doublet excited states are degenerate (a small splitting between these doublet states occurs if atom-cavity detuning is non-zero $\delta_{\rm ac} = (\omega_{\rm a} - \omega_{\rm c}) \neq 0$). When the atom-cavity system becomes coupled ($g > 0$), each pair of degenerate doublet states mix together to lift the degeneracy and new dressed states $|\pm, 1\rangle, |\pm, 2\rangle, .. |\pm, n\rangle$ are formed. The on-resonance energy splitting between these states is given by $2\sqrt{n}g$ for the n^{th} doublet.

The Jaynes-Cummings hamiltonian over the subset $|\pm, n\rangle$ in the matrix form is shown below.

$$H_{\rm JC} = \hbar \begin{bmatrix} \omega_{\rm c} n + \delta_{\rm ac} & g\sqrt{n} \\ -g\sqrt{n} & \omega_{\rm a} + \omega_{\rm c}(n-1) + \delta_{\rm ac} \end{bmatrix}. \tag{1.13}$$

The diagonalisation of this hamiltonian produces the following expressions for eigenstates/dressed states of the coupled system. These dressed states are the linear combination of the bare states $|g, n\rangle$ and $|e, (n-1)\rangle$

.

$$
\begin{aligned}
|+,n\rangle &= \sin\phi\,|g,n\rangle + \cos\phi\,|e,(n-1)\rangle\,, \\
|-,n\rangle &= \cos\phi\,|g,n\rangle - \sin\phi\,|e,(n-1)\rangle\,,
\end{aligned}
\tag{1.14}
$$

where ϕ is known as the mixing angle and is given by:

$$
\tan(\phi) = \frac{2g\sqrt{n}}{\delta_{\mathrm{ac}} + \sqrt{4g^2 n + \delta_{\mathrm{ac}}^2}}, \tag{1.15}
$$

The eigenenergies and energy splitting of n^{th} dressed states are given by:

$$
E_{\mathrm{n}}^{\pm} = \frac{\hbar}{2}(2n\omega_{\mathrm{c}} + \delta_{\mathrm{ac}} \pm \sqrt{4g^2 n + \delta_{\mathrm{ac}}^2}) \tag{1.16}
$$

$$
\Delta E_n^{\pm} = E_n^{+} - E_n^{-} = \hbar\sqrt{4g^2 n + \delta_{\mathrm{ac}}^2}) \tag{1.17}
$$

Considering the case when the system is weakly excited for which $n = 1$, meaning a single excitation is shared between ground and excited doublet eigenstates. For this case the eigenstates, eigenvalues and energy splitting expressions are given by:

$$
\begin{aligned}
|+,1\rangle &= \cos\phi\,|g,1\rangle + \sin\phi\,|e,0\rangle \\
|-,1\rangle &= -\sin\phi\,|g,1\rangle + \cos\phi\,|e,0\rangle \\
E_1^{\pm} &= \frac{\hbar}{2}(\omega_{\mathrm{a}} + \omega_{\mathrm{c}} \pm \sqrt{4g^2 + \delta_{\mathrm{ac}}^2}) \\
\Delta E_1^{\pm} &= \hbar\sqrt{4g^2 + \delta_{\mathrm{ac}}^2}
\end{aligned}
\tag{1.18}
$$

When $\delta_{\mathrm{ac}} = 0$, the atomic transition frequency is in resonance with the cavity field frequency. For such a situation, the system undergoes Rabi oscillations between these doublet eigenstates with a frequency given by g. Also, the energy splitting of the doublet states is symmetrical around the bare states and is minimum at resonance, which is given by $2g$. This splitting is known as vacuum Rabi splitting and it can even occur for a system in an initial state $|e,0\rangle$.

Figure 1.3 gives the plot of these eigenvalues with respect to atom-cavity detuning δ_{ac}. The eigenvalues for bare atom and cavity are shown by dotted lines whereas the solid lines represent eigenvalues for coupled states ($|+,1\rangle, |-,1\rangle$). An energy splitting called *avoided crossing* near the resonance is caused by the atom-

cavity coupling. The minimum energy splitting occurs at resonance ($\delta_{\rm ac}$=0) and is given by the vacuum Rabi splitting '$2g$'. Off-resonance ($\delta_{\rm ac} \neq 0$), the energy splitting increases with increase in $|\delta_{\rm ac}|$.

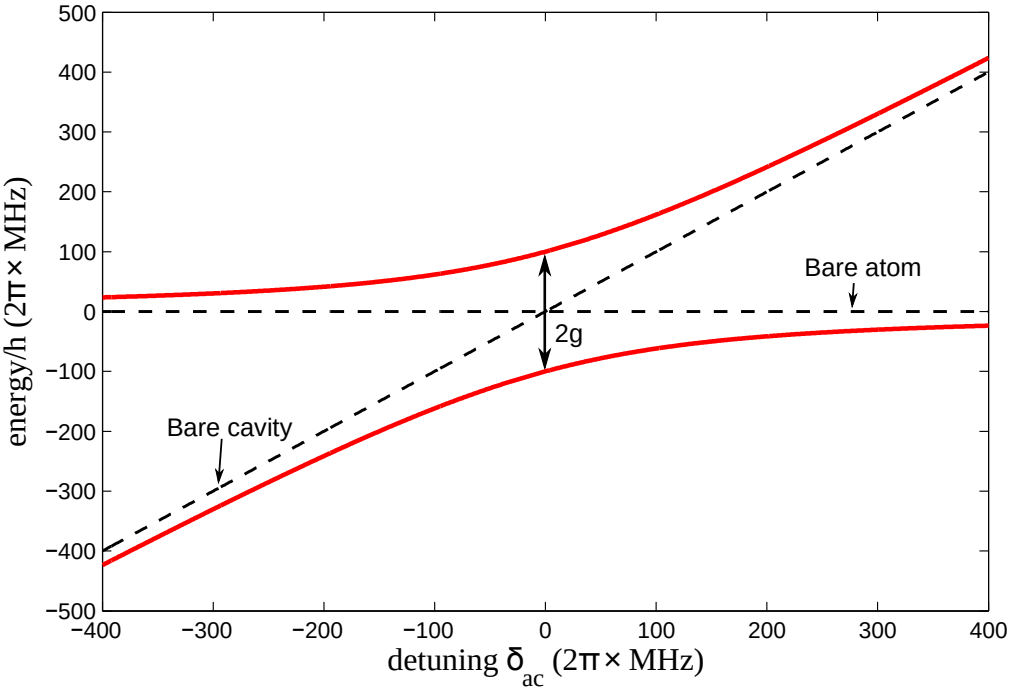

Figure 1.3: A plot of energies of uncoupled and coupled atom cavity systems with respect to the cavity detuning from the atomic resonance. The black dotted lines show the energy values for the bare atom and cavity whereas the red solid curves are for the coupled system. This theoretical plot is made for $n = 1$ and a single atom cavity system with coupling parameter $g = 2\pi \times 100$ MHz.

The damping terms describing the cavity decay rate κ and the atomic spontaneous decay rate γ have been ignored in this theoretical model. These decoherences cause the decay of the Rabi oscillations; otherwise, for an ideal system, the Rabi oscillations would continue indefinitely. In a real atom-cavity system, these terms should be included. The next section illustrates a practical atom-cavity model including driving (η) and damping terms (κ, γ).

Damped and driven atom-cavity system

Considering a realistic open quantum system as shown in figure 1.4, the photons can escape from the cavity by two mechanisms: (a) atomic spontaneous emission into the free space at a rate 2γ and (b) transmission through the cavity mirrors at a rate 2κ. Both of these processes decrease the photon number inside the cavity hence in practice, we require an external laser light source to pump the cavity mode. The pumping hamiltonian given by $H_{\rm d} = \hbar\eta(\hat{a}e^{i\omega_l t} + \hat{a}^\dagger e^{-i\omega_l t})$ is added to the Jaynes-Cummings hamiltonian H_{JC} which

has been derived in the previous section. Here η is the pumping laser field amplitude and $\omega_{\rm l}$ is the frequency of the pump laser. The total hamiltonian is given as:

$$H = H_{\rm JC} + H_{\rm d} = \hbar\omega_{\rm a}\sigma^{+}\sigma^{-} + \hbar\omega_{\rm c}a^{\dagger}a + \hbar(g\sigma^{+}a + g^{*}\sigma^{-}a^{\dagger}) + \hbar\eta(ae^{i\omega_{\rm l}t} + a^{\dagger}e^{-i\omega_{\rm l}t}). \tag{1.19}$$

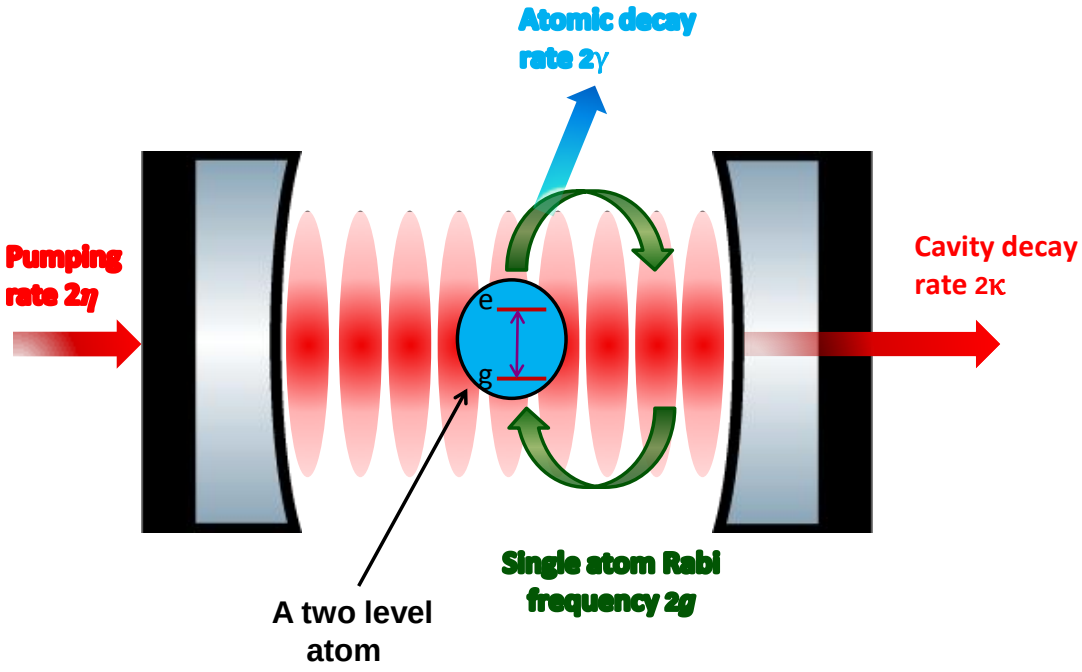

Figure 1.4: A damped and driven single atom cavity system.

To remove the time dependence from the driving term, the unitary transformation and the rotating wave approximation are used (similar to as described previously). The final time-independent hamiltonian becomes:

$$H = \hbar\Delta_{\rm a}\sigma^{+}\sigma^{-} + \hbar\Delta_{\rm c}a^{\dagger}a + i\hbar(g\sigma^{+}a + g^{*}\sigma^{-}a^{\dagger}) + \hbar\eta(a + a^{\dagger}), \tag{1.20}$$

where $\Delta_{\rm a} = \omega_{\rm l} - \omega_{\rm a}$ and $\Delta_{\rm c} = \omega_{\rm l} - \omega_{\rm c}$ are the atom and cavity detunings with respect to the frequency of the pumping laser. As mentioned before, the losses from the cavity are accounted for by two decay channels

defined by the cavity decay rate κ and atomic spontaneous emission rate γ. These terms are included in the master equation of the system:

$$\dot{\rho} = -\frac{i}{\hbar}[H, \rho] + \mathcal{L}, \tag{1.21}$$

where ρ represents the atom-cavity density matrix and the Liouville superoperator $\mathcal{L}$ is given as:

$$\mathcal{L} = \kappa(2a\rho a^\dagger - a^\dagger a\rho - \rho a^\dagger a) + \gamma(2\sigma_-\rho\sigma_+ - \sigma_+\sigma_-\rho - \rho\sigma_+\sigma_-). \tag{1.22}$$

The above master equation makes the Born and Markov approximations [14]. According to the Born approximation, the second and higher order terms of the system-environment interaction are neglected. The Markov approximation assumes that the time evolution of the density matrix ρ is independent of the history and only depends on its present value. In order to simplify the calculations for the above master equation, an approximate solution is found by using a semiclassical approach. In this approximation, the cavity field is assumed to be in a coherent state $|\alpha\rangle$[1], where α is defined as an eigenvalue of the annihilation operator a. The master equation can be solved to derive the following equations of motion:

$$\begin{aligned} \frac{d}{dt}\alpha &= -(\kappa + i\Delta_\mathrm{c})\alpha + \eta + ig\left\langle\sigma_-\right\rangle, \\ \frac{d}{dt}\left\langle\sigma_-\right\rangle &= -(\gamma + i\Delta_\mathrm{a})\sigma_- + ig\alpha\left[1 - 2\left\langle\sigma_+\sigma-\right\rangle\right], \\ \frac{d}{dt}\left\langle\sigma_-\sigma_+\right\rangle &= -2\gamma\left\langle\sigma_+\sigma_-\right\rangle + ig\left[\alpha\left\langle\sigma_+\right\rangle - \alpha^*\left\langle\sigma_-\right\rangle\right]. \end{aligned} \tag{1.23}$$

The steady state solution of these equations is given as:

$$\begin{aligned} \alpha &= \frac{1}{\tilde{\kappa}}[\eta + ig\left\langle\sigma_-\right\rangle], \\ \left\langle\sigma_-\right\rangle &= \frac{ig\alpha}{\tilde{\gamma}}[1 - 2\left\langle\sigma_+\sigma_-\right\rangle], \\ \left\langle\sigma_-\sigma_+\right\rangle &= \frac{g^2|\alpha|^2/|\tilde{\gamma}|^2}{1 + 2g^2|\alpha|^2/|\tilde{\gamma}|^2}, \end{aligned} \tag{1.24}$$

where $\tilde{\kappa} = \kappa + i\Delta_\mathrm{c}$ and $\tilde{\gamma} = \gamma + i\Delta_\mathrm{a}$ are newly defined variables. Assuming that the driving field is very

[1] A coherent state is the superposition of fock states and is a minimum uncertainty state given by $|\alpha\rangle = e^{|\alpha|^2/2}\sum_n \frac{\alpha^n}{\sqrt{n!}}|n\rangle$.

weak, the atomic excitation term $\langle \sigma_- \sigma_+ \rangle \ll 1$. Hence the steady state solution is given by:

$$\begin{aligned} \alpha &= \frac{\eta}{\tilde{\kappa}} \frac{1}{1+2\tilde{C}}, \\ \tilde{C} &= \frac{g^2}{2\tilde{\kappa}\tilde{\gamma}}, \end{aligned} \tag{1.25}$$

where $\tilde{C}$ is the single atom cooperativity, $C = g^2/\kappa\gamma$ is the on-resonance cooperativity ($\Delta_a = \Delta_c = 0$) and it defines the atom-cavity coupling strength. The mean photon number in the cavity can be calculated from the above equation of field amplitude α and is given by:

$$\langle n \rangle = |\alpha|^2 = \frac{\eta^2}{|\tilde{\kappa}|^2} \left| \frac{1}{1+2\tilde{C}} \right|^2. \tag{1.26}$$

1.2.2 Strong coupling in atom-cavity system

An open quantum system as described in the previous section interacts with the environment and dissipates incoherently. Such a system is said to be strongly coupled only if the relative strength of atom-cavity field interactions defined by g are large enough to overcome dissipation given by κ and γ. This regime is defined by the following condition:

$$g > \kappa, \gamma. \tag{1.27}$$

The phenomenon of vacuum Rabi splitting [80, 95, 6] as described before is feasible only in the strong coupling regime. In this regime, the emission of a photon from the atom becomes a reversible process meaning that the photon is reabsorbed by the atom before it leaves the cavity through dissipation processes and the coherent evolution of the system occurs. This means the excitation can be exchanged between the atom and cavity field which occurs at a rate of vacuum Rabi splitting $2g$ for a weakly pumped single atom-cavity system. Usually, in cavity QED experiments the occurrence of vacuum Rabi splitting is used as a demonstration that the system is in the strong coupling regime. Practically, this can be observed through cavity transmission signal seen by a sensitive photodiode.

1.2.3 Collective strong coupling and Rabi splitting

So far we have been discussing a single atom interacting with a single mode cavity. This section describes the Tavis-Cummings model [93, 94] for a cloud of N atoms interacting with a single mode cavity. Dicke gave the theoretical model describing a system containing N atoms coherently interacting with a single mode light field [25]. In such a system, the various atomic dipoles interact and add up to give a collective quantum system.

The theory of this system is summerised in the review paper by G.S.Agarwal [1]. The basic hamiltonian of such a system in the rotating wave approximation is given by:

$$H_{\mathrm{TC}} = \hbar\omega_{\mathrm{c}} a^{\dagger} a + \hbar\omega_{\mathrm{a}} S_z + \hbar g(a^{\dagger} S_- + a S_+), \tag{1.28}$$

where $S_{\pm,z}$ are the collective atomic spin operators of the collective quantum system and are given as:

$$\begin{aligned} S_{\pm} &= \sum_{i=1}^{N} S_{\pm}^{(i)}, \\ S_z &= \sum_{i=1}^{N} S_z^{(i)}, \end{aligned} \tag{1.29}$$

where N is the number of atoms present in the system and interacting with single mode and $S_{\pm,z}^{(i)}$ are the spin operators for N two level atoms, given as:

$$\begin{aligned} S_+^{(i)} &= |e_i\rangle \langle g_i|, \\ S_-^{(i)} &= |g_i\rangle \langle e_i|, \\ S_z^{(i)} &= \frac{1}{2}(|e_i\rangle \langle e_i| - |g_i\rangle \langle g_i|), \end{aligned} \tag{1.30}$$

where $|g_i\rangle$ and $|e_i\rangle$ represent ground and excited states of the i^{th} atom in the ensemble. In the case of weak probing the collective excitation in the atomic ensemble is weak ($n < N$) and the energy eigenvalues for excited multiplets are given as:

$$E(n, j) = \hbar \left((n - \frac{N}{2})\omega_{\mathrm{c}} - \frac{1}{2} n \delta_{\mathrm{ac}} + j\sqrt{4g^2 N + \delta_{\mathrm{ac}}^2} \right), \tag{1.31}$$

where $-n/2 \leq j \leq n/2$ and $0 \leq n \leq N$ refers to a doublet excited state. The energy splitting between the first excited doublet states ($n = 1$ and $j = \pm 1/2$) is given as:

$$\Delta E_{\pm} = \hbar(\frac{\omega_{\mathrm{a}} + \omega_{\mathrm{c}}}{2} + \sqrt{4g^2 N + \delta_{\mathrm{ac}}^2}). \tag{1.32}$$

It is evident from equation 1.32 that the on resonance ($\delta_{\mathrm{ac}} = 0$) energy splitting $\Delta E_{\pm}$ of the first excited doublet is dependent on $\sqrt{N}$. Hence the vacuum Rabi splitting for a system of N atoms interacting with single light field mode is given as:

$$2g_N = 2g\sqrt{N}. \tag{1.33}$$

The experimental measurement of this Rabi splitting is accomplished by using a weak driving laser field to probe excitation of collective system from ground to first excited doublet. When the driving laser is scanning near the resonance, the cavity transmission signal consists of two peaks (as shown in figure 1.5) evidencing the phenomenon of collective strong coupling ($g_N > \kappa, \gamma$) of atoms in the cavity. The separation between these two peaks is given by $2g\sqrt{N}$. In the absence of collective strong coupling, one would expect a single Lorentzian shaped peak in the cavity transmission signal. The cooperativity parameter as defined earlier, now takes the form:

$$C_N = \frac{g_N^2}{\kappa\gamma} = CN. \tag{1.34}$$

Hence, for a system of N atoms collectively coupled to single mode cavity field, the collective Rabi frequency splitting $2g_N$ is $\sqrt{N}$ times larger than the single atom Rabi frequency $2g$. And, the cooperativity C_N is N times the single atom cooperativity C. Therefore, the coupling can be increased by adding more atoms into the cavity mode. The typical $\sqrt{N}$ dependence of vacuum Rabi splitting evidences the presence of collective strong coupling. Recently the collective strong coupling has been realised in a single [108] and multi [107] mode cavities.

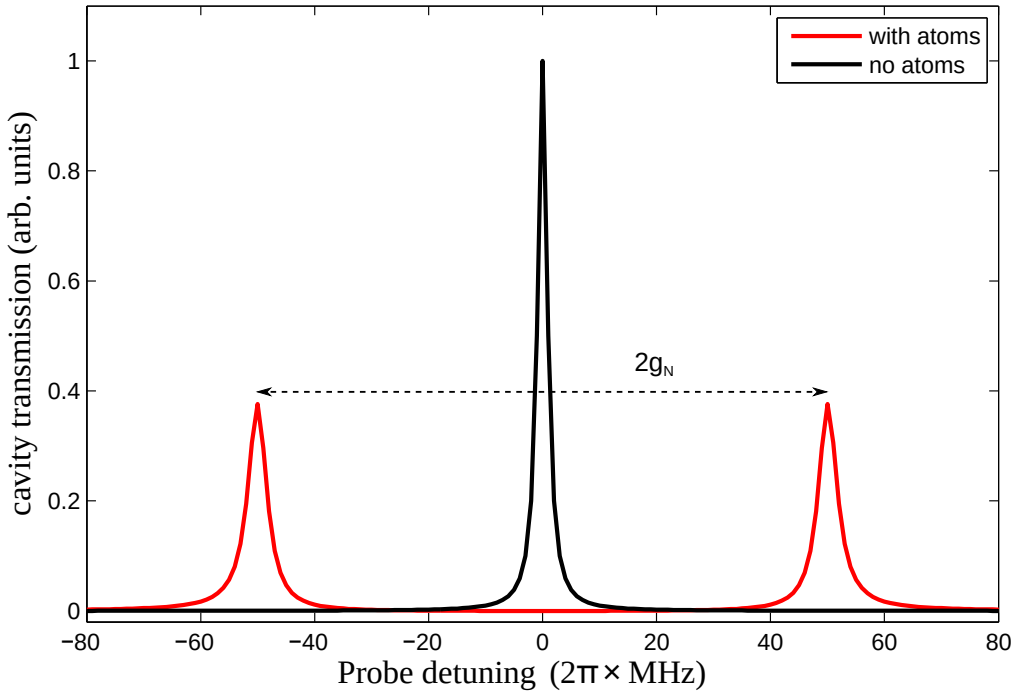

Figure 1.5: Theoretical plot of vacuum Rabi splitting in a cavity system with ensemble of N atoms. A single peak (black curve) represents empty cavity transmission whereas the twin peaks (red curve) shows the cavity transmission in the presence of atoms. The N atoms Rabi frequency is considered to be $g_N = 50$ MHz.

1.2.4 Ring Cavity design and experimental parameters

In our cavity QED experiment we are using a ring cavity and its design is shown in figure 1.6. This triangular geometry gives the degree of freedom to choose between running (cw/ccw) and standing wave modes (cos/sin), which is not possible in a linear cavity. The cavity mirrors are 6 mm diameter each. The mirrors M_2 and M_3 are identical and planar whereas M_1 is plano-concave with a radius of curvature $R = 10$ cm. The cavity has a waist in between mirrors M_2 and M_3. The cavity frame is designed to be monolithic and is made of stainless steel. The mirrors are fixed onto this frame by direct gluing into machined grooves.

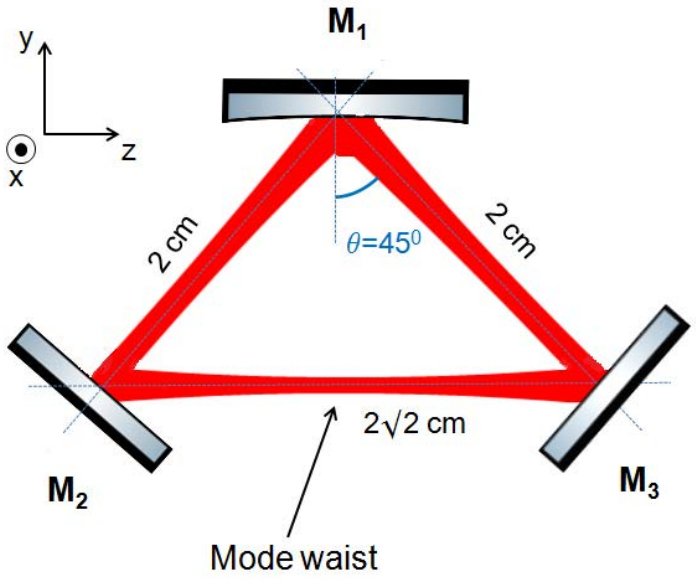

Figure 1.6: The ring cavity configuration showing the three mirror triangular cavity geometry.

The finesse is a very important parameter of the cavity, quantifying the amount of light cavity can store. A photon inside the cavity is repeatedly reflected from the mirror surfaces and it takes on average F/π cycles before it leaves the cavity through transmission. The finesse is defined as the ratio of the free spectral range to the cavity linewidth.

$$F = \frac{\nu_{\mathrm{FSR}}}{\Delta\nu} \tag{1.35}$$

where the free spectral range ν_{FSR} is the fringe separation in the transmission or reflection spectrum and cavity linewidth $\Delta\nu$ is the full width half maximum of the cavity peaks.

$$\begin{aligned} \nu_{\mathrm{FSR}} &= \frac{c}{L} \\ \Delta\nu &= \frac{2c}{\sqrt{m}L\pi} \end{aligned} \tag{1.36}$$

Table 1.1: Important ring cavity parameters.

Parameter	Value
Cavity round trip length	$L = 6.82$ cm
Radius of curvature for mirror M_2	10 cm
Mirror reflectivities (intensity) at 767 nm	$R_1 = 99.85\%$ $R_2 = R_3 = 99.85\%$
Mode waist	Sagittal $\omega_{\mathrm{x}} = 121.53$ μm Tangential $\omega_{\mathrm{y}} = 92.85$ μm
Mode volume	$V = \frac{\pi\omega_{\mathrm{x}}\omega_{\mathrm{y}}L}{2} \approx 1.21 \times 10^{-9}$ m^3
Cavity free spectral range	$\nu_{FSR} = \frac{c}{L} = 4.4$ GHz
Finesse	$F = 2100$
Cavity linewidth	$\kappa = \frac{\nu_{FSR}}{F} = 2\pi \times 1$ MHz
Single atom vacuum Rabi splitting	$g = 2\pi \times 100$ KHz

where L is the round trip length of the cavity, c is the velocity of light and m is the parameter depending on the amplitude reflectivities (r) of the mirrors. For the present three mirror triangular cavity, m is given as [7]:

$$m = \frac{4r^3}{(1-r^3)^2} \tag{1.37}$$

where r represents mirror's amplitude reflectivity. From equations 1.35 and 1.36 the finesse can be defined as a function of mirror reflectivities.

$$F = \frac{\pi\sqrt{m}}{2} \tag{1.38}$$

Equation 1.38 shows that the finesse is dependent entirely on mirror reflectivities. Table 1.1 summaries various important cavity parameters of this experiment and their corresponding values. The values of mirror reflectivities in this table are given for s-polarisation and hence all the parameters are calculated considering s-polarisation of electric field of the driving laser light. As the mirror M_1 is curved and the angle of incidence on this mirror is $\theta = 45^0$, so we should consider the astigmatism while calculating the cavity mode waist. Due to this, the mode profile is not circular but is elliptical, which leads to two different mode waists i.e. tangential ω_{x} and saggital ω_{y}. The mechanical design of the cavity was made by another PhD student on this project and further details on the design can be found in his thesis [62].

For a single atom confined in the cavity mode, the strong coupling regime is given in equation 1.27. In the optical regime, this requires a cavity with very high finesse and small mode volume. For large ensemble of atoms, the coupling constant is increased and becomes $\sqrt{N}$ times the single atom vacuum Rabi splitting ($g \rightarrow g_N = \sqrt{N}g$). Hence one can achieve collective strong coupling with large atomic ensembles instead of a single atom by using a medium finesse and mode volume. For example the single atom cavity QED experiment in the group of G. Rempe [56, 57] has a finesse of $F = 4.3 \times 10^5$. Whereas our ring cavity has a moderate finesse of $F = 2100$. Hence, we use the tool of confining large atomic ensemble in the cavity in order to enhance the coupling. For such a system, the condition to realise collective strong coupling is:

$$g_N > \kappa, \gamma \tag{1.39}$$

According to this condition we require only 10^3 atoms coupled to the cavity mode to realise the phenomenon of collective strong coupling. In our experiment, we load atoms in a magneto optical trap (MOT) at the cavity mode waist. The MOT volume does not perfectly overlap with the cavity mode volume because the MOT dimensions are larger than the mode size in the plane transverse to the cavity axis. In addition to this, the cavity field has a Gaussian profile and so atoms at different positions in the cavity mode feel different field so their coupling strength is different. Hence the effective number of atoms coupled to the cavity mode is less than the total number of atoms loaded in the MOT, $N_{\text{eff}} < N_{\text{mot}}$. The effective number of atoms coupled to the cavity can be derived as below:

$$N_{\text{eff}} = \int n_{x,y,z} \cdot \frac{I(x,y,z)}{I_0} dV, \tag{1.40}$$

where $n_{\text{x,y,z}}$ and $I(x,y,z)/I_0$ are the density of the MOT and normalised intensity of the cavity mode (TEM_{00} mode). These terms can be defined as:

$$n_{\text{x,y,z}} = n_0 e^{-\frac{1}{2}\left(\frac{x^2}{\sigma_x{}^2} + \frac{y^2}{\sigma_y{}^2} + \frac{z^2}{\sigma_z{}^2}\right)}, \tag{1.41}$$

here n_0 is the peak density of the MOT and $\sigma_{\text{x,y,z}}$ represent the MOT dimensions.

$$I(x,y,z) = I_0 e^{-2\left[\left(\frac{x}{\omega_{\text{x}}}\right)^2 + \left(\frac{y}{\omega_{\text{y}}}\right)^2\right]}, \tag{1.42}$$

Here I_0 is the peak intensity at the mode centre. After integrating the equation 1.40 takes the form,

$$N_{\text{eff}} = \frac{N_{\text{mot}}\omega_{\text{x}}\omega_{\text{y}}}{\sqrt{(4\sigma_{\text{x}}^2 + \omega_{\text{x}}^2)(4\sigma_{\text{y}}^2 + \omega_{\text{y}}^2)}} \tag{1.43}$$

The typical size of MOT in this experiment is $\sigma_x = \sigma_y = 0.31$ mm which gives,

$$N_{\text{eff}} = 0.03 \times N_{\text{mot}} \tag{1.44}$$

This means that we need a MOT of only 3.3×10^4 atoms or more to realise collective strong coupling and vacuum Rabi splitting. The number of atoms in our potassium MOT is of the order of 10^7 (calculated later in the chapter 6), which is much larger than what is required ($\sim 10^3$ atoms) to see Rabi splitting phenomenon in our system.

1.3 Cavity Cooling: The Motivation

All the conventional laser cooling methods (including Doppler cooling, sisyphus cooling, polarisation gradient cooling etc.) are dependent on repeated cycles of absorption and spontaneous emission of photons by an atom. The absorption of red detuned photons by atoms, followed by the spontaneous emission in each cycle is the key mechanism to remove the kinetic energy and hence cool the atoms. The initial velocity of the atom is much larger than to a single photon recoil, therefore this requires many absorption and scattering cycles to cool down the atoms to ultracold temperatures. So, these techniques are only successful for systems with closed (or nearly closed) transitions, e.g. alkalis. In contrast to these conventional methods, the concept of cavity cooling does not depend on the spontaneous emission rather it depends on the dipole force on the polarisable particles. Therefore this mechanism is independent of the internal structure of the particles to be cooled hence, it is a good technique to cool molecules, macroscopic objects, BECs [113], simultaneous cooling of two species and also for non-destructive cooling of qubits [35]. Molecules do not have closed transitions, this makes them difficult to cool using Doppler cooling. However there has been recent advancements to make molecule MOTs [44, 4].

There have been several cavity cooling methods proposed in the past 25 years. The theoretical idea of sub-Doppler cooling of atoms using frequency dependent vacua (or coloured vacua) within the boundaries of cavity mirrors was first introduced by M. Lewenstein *et al.* and Mossberg *et al.* in 1990s [53, 60]. In the following sections, I explain the basic idea of cavity cooling from a classical point of view, cavity cooling in

a ring resonator, and finally estimations for the cooling temperature limit in our cavity.

1.3.1 Basic idea behind cavity cooling in a linear cavity

Consider a laser light field entering in a two-mirror linear cavity, which is red detuned relative to the cavity resonance ($\omega_l < \omega_c$ and $\omega_c \approx \omega_a$). A polarisable particle induces a position dependent refractive index, depending on the local intensity at that position. Therefore, it changes cavity resonance frequency and hence the interacavity intensity depending upon its position. When the particle sits at an antinode, the cavity resonance frequency is reduced for a red detuned laser field. Therefore, the intracavity intensity becomes maximum at antinodes and minimum at the nodes. In general (for either red or blue detuned field), at minimum of the dipole potential well, the intracavity intensity is maximum, and the cavity resonance frequency is minimum. Now, we introduce the atom dynamics. Consider the atom is moving from potential

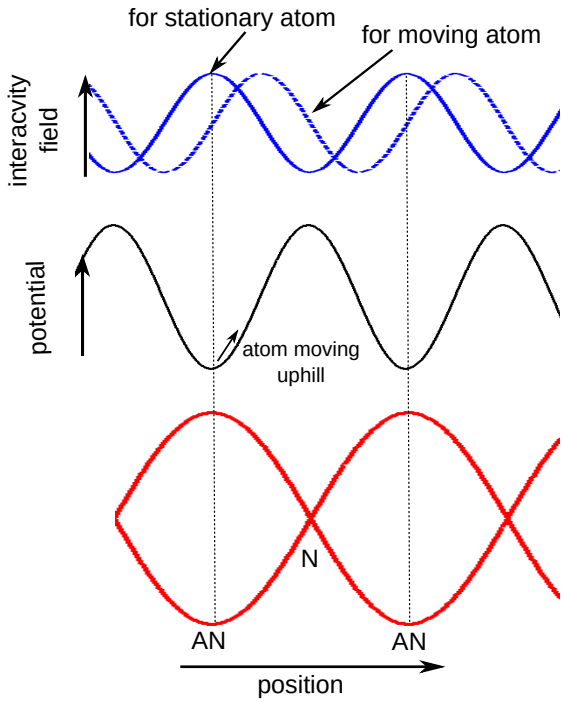

Figure 1.7: An illustration of the idea of cavity cooling in a linear cavity. At the bottom of this picture, a standing wave field is shown by red curves inside a two mirror cavity. AN=antinode and N=node. In the middle, the black curve represents the standing wave potential. For a red detuned laser field ($\omega_l < \omega_{c,a}$), the potential minima correspond to ANs and maxima correspond to Ns of the standing wave. At top the solid and dotted curves represent the intracavity intensity for a stationary and moving (with constant velocity) atom respectively.

minimum to maximum (see figure 1.7). Due to the cavity's finite response time, the intracavity intensity becomes maximum when the atom has already left the potential minimum. Hence for all times, the atom

sees a steeper potential while climbing the potential well and a shallower potential while running down the potential well. Overall, the particle loses its kinetic energy. Classically, this deceleration continues until the atom is trapped in a potential well and comes to rest. But in practice this does not happen; the final non-zero temperature depends on the cavity linewidth (2κ) and is given by:

$$k_B T = \hbar\kappa \tag{1.45}$$

This equation does not provide any lower limit on final temperature as the cavity linewidth can be made very small. However, with decrease in cavity linewidth the capture velocity range (defined as the range of atomic velocities which can be cooled down) also decreases. The capture velocity range for this cooling mechanism to work is given by $kv < \kappa$. Alternatively the cavity cooling process can be described by enhancement of coherent scattering of blue shifted photons over red shifted ones in a blue detuned cavity [102].

As free space Doppler cooling depends on the spontaneous emission rate, the final temperature is limited by the atomic linewidth γ. In contrast, the process of cavity cooling does not depend on atomic excitation or spontaneous emission. Rather it depends on the dipole force (it relies on the particle's polarisability), which has a delayed action on the particle because of the slow cavity response (or finite cavity linewidth κ). As the cavity linewidth κ can be much smaller than γ, much colder temperatures can be achieved in principle with cavity cooling techniques.

The idea of cooling a single atom using a high finesse cavity was proposed by Peter Horak *et al.* [43]. In this scheme, the cooling is explained by a sisyphus type cooling mechanism in the strong coupling regime. Cavity-mediated cooling for molecules using far-detuned laser fields and weak coupling was suggested by V. Vuletic and S. Chu in 2000 [102, 20, 41]. A review of cavity cooling is given by P. Domokos and A. Ritsch[74]. The cavity cooling was first demonstrated for Cs atomic ensemble by the group of V. Vuletic in 2003 [17]. In 2004, in the group of G. Rempe the cooling of a single atom (^{85}Rb) in a high finesse linear cavity was reported for the first time [56]. To date many groups have reported observation of cavity assisted cooling in linear cavities for single atoms [31, 66], ions [51] and atomic ensembles [17, 10]. The simultaneous cooling and trapping using a far off resonant laser field has been demonstrated in reference [100, 67].

1.3.2 Cavity cooling in a ring resonator

So far our discussion was limited to cavity cooling in the case of linear cavities. This section describes cooling in a ring shaped cavity. In a ring cavity geometry, the presence of an atom can give rise to two different effects:

1. The resonance frequencies of two counter-propagating modes are modified depending on the atom's position. This effect is similar to what was discussed above for a linear cavity and leads to cavity cooling with a final temperature limited by the cavity linewidth as demonstrated by equation 1.45.

2. The atom can scatter photons from one cavity mode to another leading to a phase shift of the standing wave in the cavity. The presence of this additional effect enhances the cooling rate in a ring cavity in comparison to a linear cavity.

The presence of both these effects together can result in achieving cooling beyond the cavity linewidth limit.

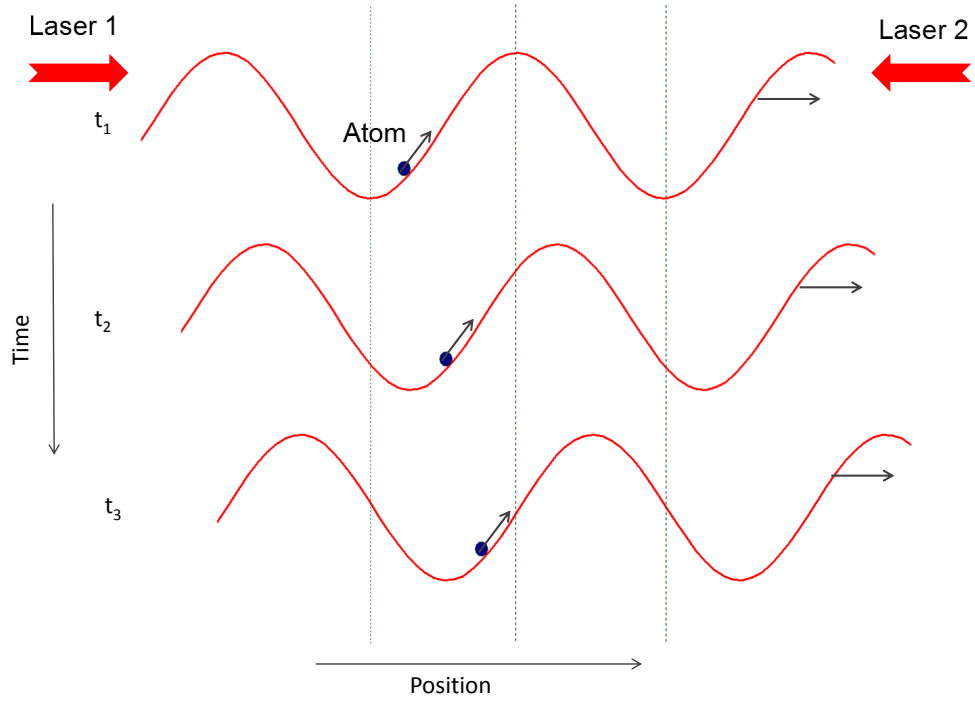

Figure 1.8: A simple picture illustrating the effect of atomic motion on the phase of the standing wave. At time t_1, the atom drags the standing wave along with itself due to photon scattering from one laser beam to the another. Due to the motion of the standing wave, the atom is continuously moving uphill at all later times t_2 and t_3.

Consider a red detuned laser field ($\omega_l < \omega_a$) inside the ring cavity. The velocity v of the atom should be

small ($kv < \kappa, \gamma$) for cavity cooling effect to occur. The dipole force generated by the standing wave in the cavity attracts the atom towards its antinode. As the phase of the standing wave field in a ring cavity can shift, the slowly moving atom drags the standing wave field along with it. Because of this the atom is always climbing the potential well and experiences an additional frictional force which gives rise to faster cooling rate. The theoretical results published by the group of Helmut Ritsch [33] support the above explanation. These results demonstrate that the cooling force originating from the spatial shift of the intracavity standing wave enhances the cooling rate in a ring cavity in comparison to a linear cavity in which the frictional force originates solely from the position dependence of the amplitude of the intracavity field. Another recent publication [84] by the same group describes that using strong pump fields, a polarisable particle can be cooled faster in a ring cavity in comparison to a linear cavity.

The above explanation becomes rather complicated if one considers an ensemble of atoms in the cavity. The motion of atoms in the ensemble should be synchronised in order to effectively shift the phase of the standing wave. Otherwise, their mutual influence on the phase will cancel out, resulting in no phase shift. This synchronisation can be achieved through the process of self organisation of atoms when they are coupled to a standing wave field of the cavity. Beginning with a uniform atomic distribution in the cavity field, the slowly moving atoms start redistributing themselves into the potential wells. The Bragg reflection from this periodic distribution of atoms increases the scattering of photons into the cavity leading to a deeper lattice potential of depth defined by: $U_0 N_{\text{eff}} = g^2 N_{\text{eff}}/\Delta_{\text{c}}$. This leads to the formation of atomic density grating and greatly enhances the collective scattering process. The threshhold [2] for atomic self organisation is given by equation 1.46. This condition states that the effective potential trap depth (or light shift $U_0 N_{\text{eff}}$) should be equal to or bigger than the cavity line width κ. Once this threshold is reached the atomic motion can effectively change the phase of the standing wave field and hence enhances the cavity cooling for an atomic ensemble in a ring cavity.

$$\mu = \frac{g^2 N_{\text{eff}}}{\Delta_{\text{c}} \kappa} \geq 1. \tag{1.46}$$

In the present experiment, one of the motivations of the ring cavity set-up is to explore enhanced cavity cooling techniques beyond the limit of cavity linewidth. The equation 1.45 defines the achievable cooling temperature solely because of the temperature limit imposed by the cavity linewidth (valid only for linear cavities) and is given as:

$$T_\kappa \approx 48 \mu\text{K}. \tag{1.47}$$

Since our cavity linewidth ($\kappa = 2\pi \times 1$ MHz) is large, hence, this temperature is not very low however is

nearly 3 times smaller than the Doppler temperature ($T_D = 145\ \mu$K). The off-resonant photon scattering rate into the cavity γ_c and the scattering rate into the free space γ_{fs} are:

$$\begin{aligned} \gamma_{\mathrm{c}} &= \frac{g^2}{\Delta_{\mathrm{c}}}, \\ \gamma_{\mathrm{fs}} &= \frac{\gamma^3}{\Delta_{\mathrm{c}}^2}, \end{aligned} \tag{1.48}$$

where $\gamma = 2\pi \times 3$ MHz is the atomic spontaneous emission rate. The cavity detuning for which the photon scattering rate into the cavity exceeds scattering rate into free space can be calculated from the following condition:

$$\begin{aligned} \gamma_{\mathrm{c}} &\geq \gamma_{\mathrm{fs}}, \\ \Delta_{\mathrm{c}} &= 2\pi \times 2.7\ \mathrm{GHz}. \end{aligned} \tag{1.49}$$

The threshold condition defined in 1.46 can be used to calculate the minimum number of atoms required to achieve self organisation at a cavity detuning of 2.7 GHz .

$$N_{\mathrm{eff}} \approx 2.7 \times 10^5. \tag{1.50}$$

These preliminary calculations show that by loading more than 2.7×10^5 atoms at around a 2.7 GHz cavity detuning, our ring cavity system is suitable to observe enhanced cavity cooling effects beyond the temperature limit of T_κ which is generally defined for linear cavities.

CHAPTER 2

ELONGATED POTASSIUM-39 MOT

In the present chapter, the first part describes the physics of laser cooling of simple two-level neutral atoms. The geometrical details of our potassium-39 MOT are explained in the later part of this chapter. Section 2.1 gives an introduction of the radiation scattering force, optical molasses and Doppler cooling limit. Section 2.2 focuses on the need of elongated magneto-optical trap (MOT) in our experiment, its shape and orientation in space with respect to the ring cavity axis, MOT beams and geometry of our rectangular magnetic field coils.

2.1 Laser cooling of neutral atoms

The idea of Doppler cooling was first suggested by Hänsch and Schawlow [37], Wineland and Dehmelt [111], and Wineland and Itano [112] in the 1980s. In 1997, the Nobel prize for physics was awarded to Claude Cohen-Tannoudji, Bill Phillips and Steve Chu for their contributions to the field of laser cooling and trapping of atoms. The principle of this method is based on the fact that the radiation scattering force on atoms can be made velocity dependent using Doppler shift and therefore be used for cooling atoms. Apart from the Doppler cooling, there are a number of other methods of laser cooling and those include: Sisyphus cooling, resolved sideband cooling, cavity cooling, sympathetic cooling and Zeeman slower. The theory in this section has been followed from references [59, 52].

2.1.1 The scattering force

The radiation scattering force that a laser light field exerts on an atom arises because of momentum exchange. When an atom absorbs a photon from the laser beam, atomic momentum is changed from $\vec{p}_{\text{atom}} = m\vec{v}$ to $\vec{p}_{\text{atom}} = m\vec{v} + \hbar\vec{k}$, where $\hbar\vec{k}$ is the momentum of the photon absorbed, $\vec{v}$ is the velocity of the atom, $\vec{k}$ is the

light wave vector with $|\vec{k}| = 2\pi/\lambda$ and λ is the wavelength of the light. If $\vec{k}$ and $\vec{v}$ are anti parallel then the momentum, and hence the velocity of the atom are decreased. Thus, when the atom and photon are moving towards each other, the atom is decelerated. When the excited atom decays to ground state via spontaneous emission, it receives a second momentum kick. However the process of spontaneous decay is isotropic (the photon is emitted in a random direction), hence results in zero momentum change by averaging over many such events. As the atoms are in motion, the laser frequency is shifted by the Doppler shift $\omega_{\mathrm{D}} = -\vec{k}.\vec{v}$. For the maximum absorption and scattering rate, the Doppler shifted laser frequency in the moving atom's frame should match atomic transition frequency ω_{a}. This scattering rate is given by:

$$\gamma_{\mathrm{p}} = \frac{s_0\gamma/2}{1 + s_0 + [2(\delta + \omega_{\mathrm{D}})/\gamma]^2} \tag{2.1}$$

where $\delta = \omega_{\mathrm{l}} - \omega_{\mathrm{a}}$ is the laser detuning from resonance, ω_{l} is the laser frequency, ω_{a} is the atomic transition frequency, $\gamma \equiv 1/\tau$ is the spontaneous transition rate of the atom and $s_0 = I/I_{\mathrm{s}}$ is the ratio of the laser beam intensity and the saturation intensity $I_{\mathrm{s}} = \pi hc/3\lambda^3\tau$. Maximum deceleration of an atom requires fulfillment of the condition $(\delta + \omega_{\mathrm{D}}) << \gamma$. The average scattering force exerted on an atom by the laser beam is given by multiplying the scattering rate and the momentum transfer to the atom for a single atom-photon interaction event.

$$\vec{F} = \hbar\vec{k}\gamma_p \tag{2.2}$$

2.1.2 Optical molasses

Equation 2.2 gives the scattering force on atoms moving in a single laser beam. If the atoms are moving in two laser beams with equal intensities and detunings directed opposite to one another, the net radiative force on atoms is given by the sum of the scattering forces $\vec{F}_+$ and $\vec{F}_-$ by each of the two laser beams.

$$\vec{F}_{\pm} = \pm\frac{\hbar\vec{k}\gamma}{2}\frac{s_0}{1 + s_0 + [2(\delta \mp \omega_D)/\gamma]^2}, \tag{2.3}$$

and

$$\vec{F}_{\mathrm{OM}} = \vec{F}_+ + \vec{F}_- \cong \frac{8\hbar k^2\delta s_0\vec{v}}{\gamma(1 + s_0 + (2\delta/\gamma)^2)^2} \equiv -\beta\vec{v} \tag{2.4}$$

where $\vec{F}_{\mathrm{OM}}$ is the net force on an atom in one dimensional optical molasses and β is the damping constant.

It is evident from the above equation that there is no net force acting on the atoms at rest. However a moving atom experiences a net force (given by equation 2.4) proportional to its velocity, whose sign depends

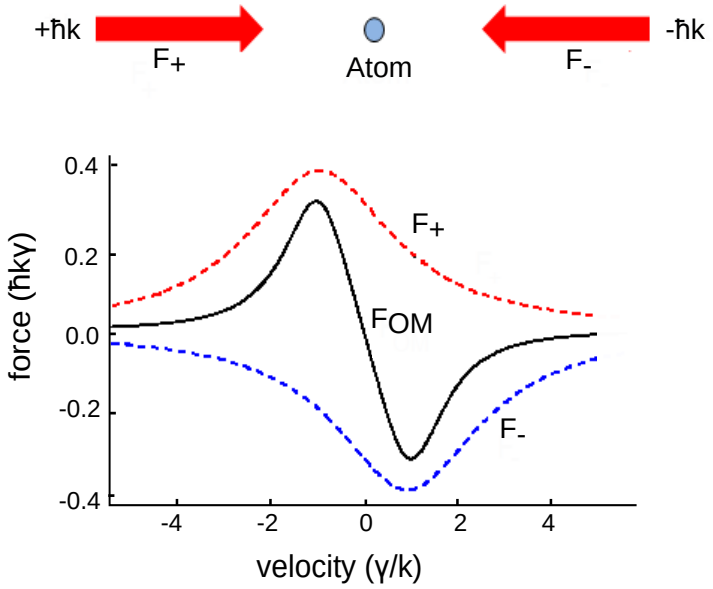

Figure 2.1: Doppler cooling force on a moving atom with two counter propagating red-detuned laser beams. Solid curve shows the net force on the atom, whereas red and blue dotted curves correspond to forces F_+ and F_- respectively. The net force $F_{\rm OM}$ is a pure damping force over a restricted velocity range [59].

on the frequency of the laser. If the laser beams are red detuned (from the atomic resonance), the atom will be in resonance with the laser beam moving opposite to atomic motion. Whereas, the atoms will be out of resonance with the beam parallel to the atomic motion. Therefore, for a red detuned laser, the interaction of the atoms is stronger with the laser beam that opposes their velocity, hence atoms are decelerated. This technique of decelerating atoms is known as 'optical molasses' (OM). If the laser field consists of three intersecting orthogonal pairs of counter propagating beams, then motion of atoms experiences a viscous damping in all three dimensions. Therefore atoms can be collected and cooled in the region of intersection of the six beams. This is known as 3D optical molasses.

2.1.3 Doppler cooling limit

If the atomic motion was only under the influence of damping force (given by equation 2.4), then all the atoms would quickly come to rest with the atomic sample at a temperature $T = 0$K. However this is not the case. There are some heating effects associated with the random nature of emission and absorption of photons by the atoms. The minimum temperature achievable with Doppler cooling is called the Doppler cooling limit or Doppler temperature. After balancing the Doppler cooling rate ($-\beta v^2$) by the heating rate ($4\hbar\omega_r\gamma_p$, where ω_r is recoil frequency), we get Doppler temperature.

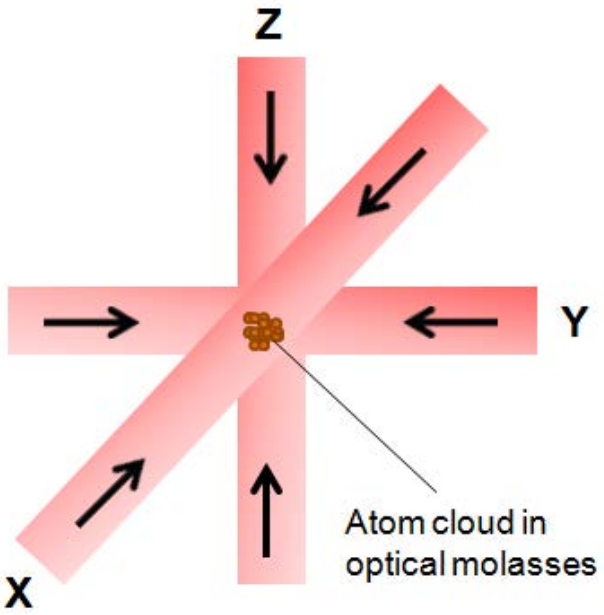

Figure 2.2: Three dimensional optical molasses with three mutually perpendicular standing waves. The standing waves are formed by three retro reflecting red detuned laser beams. The atoms experience frictional force from all the three direction.

$$T_D = \frac{\hbar\gamma}{2k_B} \tag{2.5}$$

The Doppler limit for potassium atoms is 145 μ K. The first 3D OM was observed at NIST in 1985 [20] and it was a great surprise that the measured temperature of sodium atoms in OM was nearly 10 times lower than its Doppler limit T_D=240 μK. This shows that the two level picture of OM as explained above is not sufficient for multi-level atoms. Furthermore, sub-Doppler cooling mechanisms [23] can be described by considering the optical pumping among multiple sub-levels of an atomic state (e.g. Zeeman and hyperfine) and spatial variation of the AC-stark shift due to polarization gradients. Sub-Doppler cooling can cool atomic samples down to recoil limit, typically this limit for alkali atoms is few hundreds of nK. In order to achieve temperatures below recoil limit, one can use techniques of evaporative cooling and Raman sideband cooling.

2.2 Elongated potassium-39 MOT

The cooling and damping of neutral atoms in an optical molasses takes place in the intersection region of three pairs of orthogonal beams. By adding a quadrupole magnetic field to this system and with correct combination of beam polarisations, one can obtain a magneto optical trap (MOT). It was first demonstrated

by Raab et al. in 1987 [78]. Both the optical and magnetic forces play important role in the functioning of a MOT. Nowadays a MOT has become the starting point and basic requirement for most of the atomic physics experiments. The physics behind the working of a MOT can be referred from many standard textbooks [30, 5, 59, 52].

In this section, I describe our potassium-39 MOT which is different in shape from usual MOTs. First, the requirement for special magnetic fields and the unusual orientation of MOT beams to achieve an elongated MOT is explained. Following this, the simulation, design, construction and field gradient measurements of the magnetic field coils is thoroughly discussed.

2.2.1 Need for an elongated MOT

In experiments which either aim for making a Bose Einstein Condensate (BEC) inside a cavity or have a very small sized cavity, it is common to cool and trap atoms outside and then transfer them into the cavity. This arrangement requires more than a single vacuum chamber. For the sake of simplicity we designed our system in such a way that we could directly make the MOT inside the ring cavity as shown in the figure 2.3. This allows us to have a single octagonal vacuum chamber with the ring cavity held on the bottom flange. This simplified the design and assembly of our vacuum system and saved a lot of complexity.

As explained in the section 1.2.4, we require a large ensemble of atoms and high optical density in the cavity mode in order to enter the strong coupling regime of atom-cavity system. As evident from figure 2.3, the MOT is elongated along the z-axis. We require this to allow us to load the maximum number of atoms in the cavity mode. Moreover, this geometry provides full optical access along the z-axis. The elongated MOT is achieved by having two pairs of rectangular shaped anti-helmholts coils as discussed in the next section 2.2.2.

2.2.2 MOT Geometry

In a conventional 2D MOT there are four cooling beams and 2D quadrupole magnetic field to achieve trapping along the axes containing the beams, but there is no force on the atoms along the longitudinal axis (axis perpendicular to the plane containing MOT beams) and they can move freely. Our configuration has six beams instead of four and a zero magnetic field line along the longitudinal direction as shown in figure 2.4. The zero field line along the z-axis enables us to have an elongated MOT as there is no trapping along that direction. One of the beam pairs is oriented along the x-axis and other two pairs are in yz plane. The beam pairs in yz plane are not oriented along the magnetic field symmetry axes and are aligned at a 45° angle from

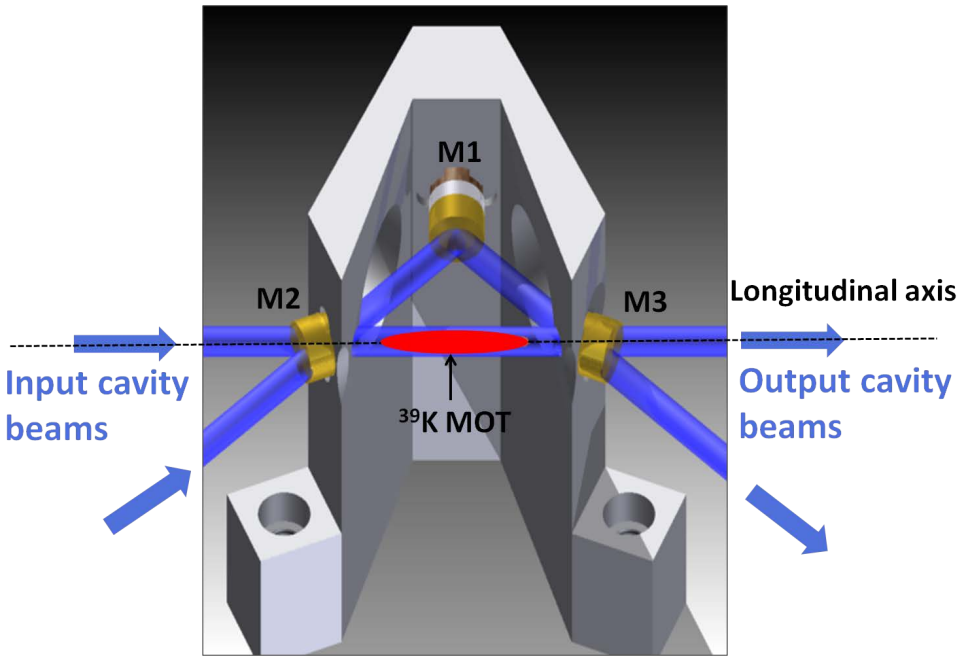

Figure 2.3: The ring cavity with potassium-39 MOT located at the center of the cavity mode and elongated along the longitudinal axis.

the z-axis. This unusual orientation of MOT beams allows us to loosely hold the atoms and compensate for no magnetic trapping along the z-axis. The idea of this modified 2D MOT with a zero magnetic field line along the longitudinal axis is inspired by the work referred to here [54, 86].

The figure 2.4 and 2.5 show the schematics of our MOT geometry from two different view planes. Here the vacuum chamber and ring cavity are not shown for the sake of clarity. There are four rectangular shaped MOT coils arranged in a cage like structure, to generate a 2D quadrupole magnetic field. The coil frames are not shown in this picture for the sake of clarity. The rectangular coils are built by wrapping a copper strip (size 14 mm×0.25 mm) on a rectangular frame (discussed in section 2.2.4). As shown in figure 2.4 the elongated MOT configuration consist of three pairs of retro-reflected MOT beams. Each beam pair consists of trapping and repump laser light in a 1:1 ratio. The trapping laser is around 8 MHz red detuned from $F = 2 \rightarrow F' = 3'$ transition frequency and the repump laser is at 2 MHz red detuning from the $F = 1 \rightarrow F' = 2'$ transition frequency. A total power of 75 mW in both the trapping and repump beams is used to create the MOT. The MOT beams have a Gaussian diameter of 7.5 mm each. Both the beams (in each pair) are either left/right circularly polarised. The right combination of beam polarisations and magnetic field direction gives rise to magneto optical trapping. According to definition, left (right) circularly polarised beam has its angular momentum parallel (anti-parallel) to the propagation axis. The same handedness of the retro-reflected beam

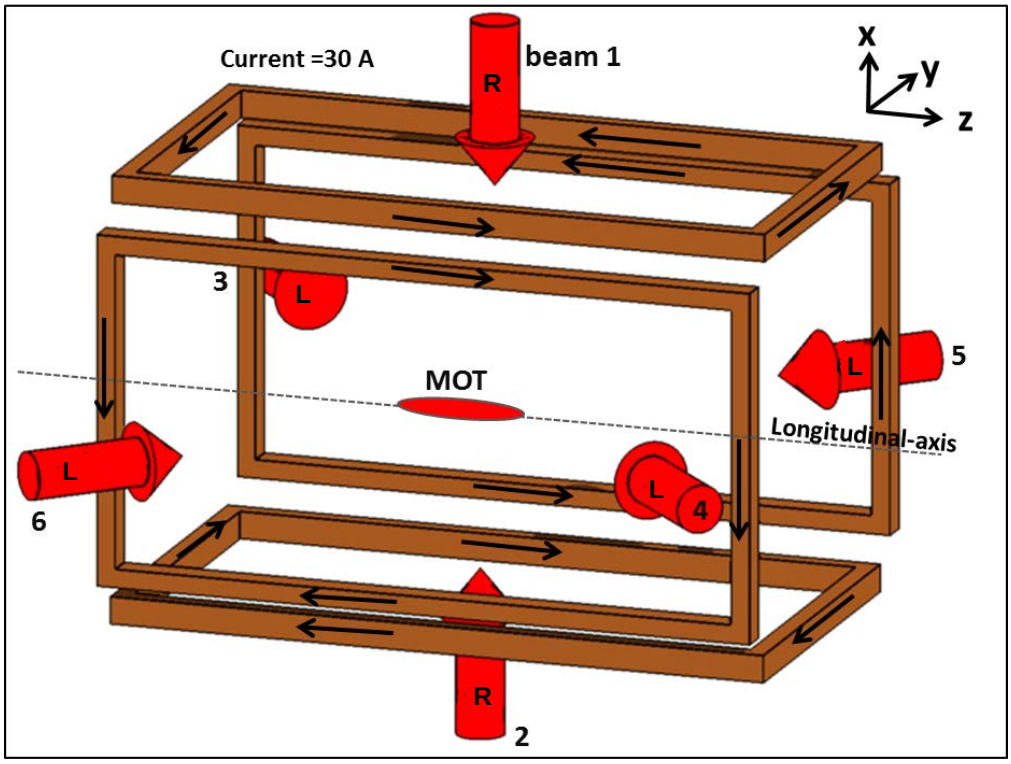

Figure 2.4: Schematic of the magnetic field coil system and laser beam polarisations and orientations to make a null line elongated MOT. This schematic gives a 3D view of the whole system, black arrows show the direction of the current in coils and big red arrows are the MOT beams.L=left and R=right handed circular polarisations. Here x-, y- and z-axes refer to magnetic field symmetry axes which are not aligned with the MOT beams axis in yz plane.

in each pair is achieved by adding a quarter wave plate before the reflecting mirror. The first beam pair is along the x-axis (beams 1,2), and the other two pairs are in yz plane and aligned at an angle of 45° clockwise (beam 3,4) and anti-clockwise (beams 5,6) relative to the z-axis (see figure 2.5). In contrast to conventional 2D and 3D MOTs, the beams 3,4,5,6 are not aligned in the axis of symmetry of the quadrupole magnetic field. The orientation of the MOT beams provides optical force in the longitudinal direction to compensate for the zero magnetic field along that line. In addition to this, it also provides a full optical access for the cavity beams along this direction of high OD. As the field gradients don't interfere with the atom-light interactions in this axis of high OD, hence we do not need to switch off the MOT field for detection purposes.

2.2.3 MOT beams

We require our MOT beams to consist of two frequencies, one near cooling ($F = 2 \rightarrow F' = 3'$) and another near repump ($F = 1 \rightarrow F' = 2'$) transition. More details on laser system are provided in chapter 5. Both the

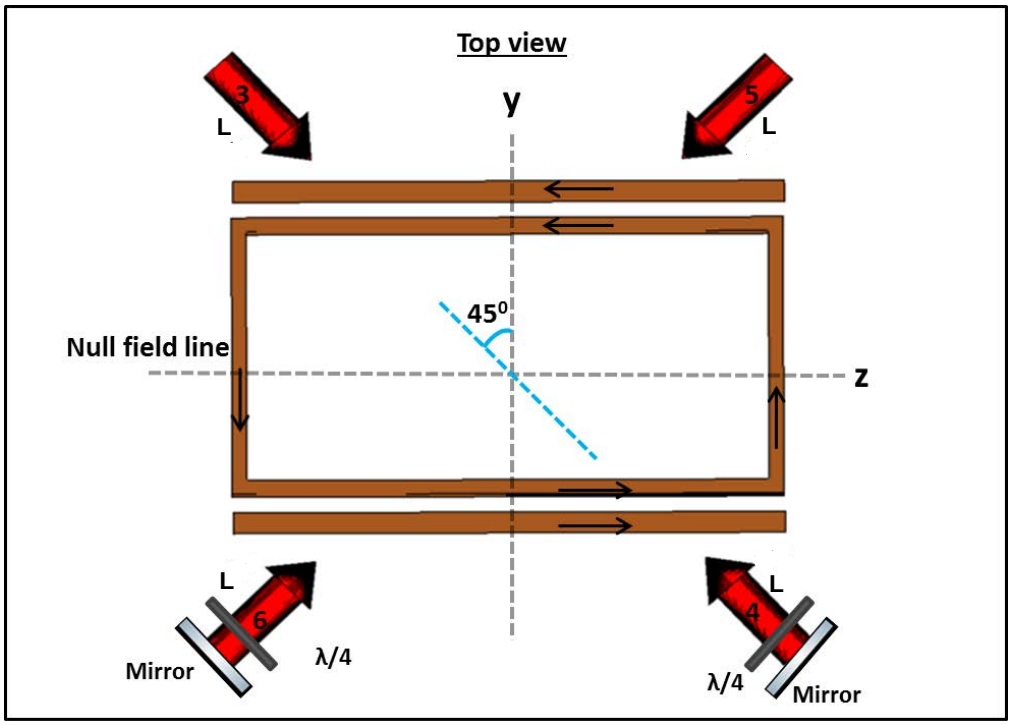

Figure 2.5: Cross-sectional view of zero-field line MOT schematic in YZ plane. Beam pair 3,4 and 5,6 are at an angle 45° from y- and z-axis respectively. L=left handed circular polarisations.

cooling and repump laser beams are simultaneously amplified using a tapered amplifier (TA) set-up which is explained in detail in section 5.3. The amplified output of the TA is approximately 400 mW for an input seed beam power of 11 mW at 1.5 A of injection current.

The amplified TA output power is divided in to three branches using waveplates, polarising beam splitters (PBS) and a mirror and coupled to three polarisation maintaining, single mode optical fibres (Thorlabs, PM310827). A waveplate in each branch is used to match the polarisation axis of the linearly polarised incoming beam with the slow axis of the optical fibres. We need polarisation maintaining fibres because polarisation of MOT beams should be fixed as described in the previous section. We use three Thorlabs fixed focus length, large beam size collimators (Thorlabs, F810SMA-780) as output couplers. Each of these collimators has a collimated beam diameter ($1/e^2$) of 7.5 mm. Each of these three large linearly polarised collimated beams is then passed through a combination of a polariser and a QWP. The polariser and QWP mounts are glued together and mounted on a single post. This system works in such a way that we could rotate the QWP individually or rotate both of them together. The optical axis of the QWP has to be fixed at an angle of ±45° with respect to the axis of the linearly polarised incoming collimated beam to achieve the correct circular polarisation. It is hard to find out the correct angle of the QWP to get circular polarised

beams and for this we make use of movie 3D glasses. In 3D glasses, each lens is a combination of a QWP and a linear polariser. We hold a 3D glass after the QWP and measure the beam intensity after the 3D glass. The QWP is rotated until we get a maximum or minimum beam intensity coming out of the 3D glass. The two angles of the QWP which give maximum and minimum beam intensities correspond to two different circular polarisations (left and right). After the polarisations are set, we can rotate the polariser and QWP together to balance the MOT beam powers. The MOT beams 1,2,3 and 4 have left handed whereas 5 and 6 have right handed circular polarisations.

2.2.4 Magnetic fields

The shape, size and current through the MOT coils decide the magnetic field gradient along the different spatial directions. The rectangular shaped magnetic field coils are designed to generate a null gradient line along z-axis as described in the section 2.2.2, and a gradient of 8-10 G/cm along the x- and y-axes. We wanted

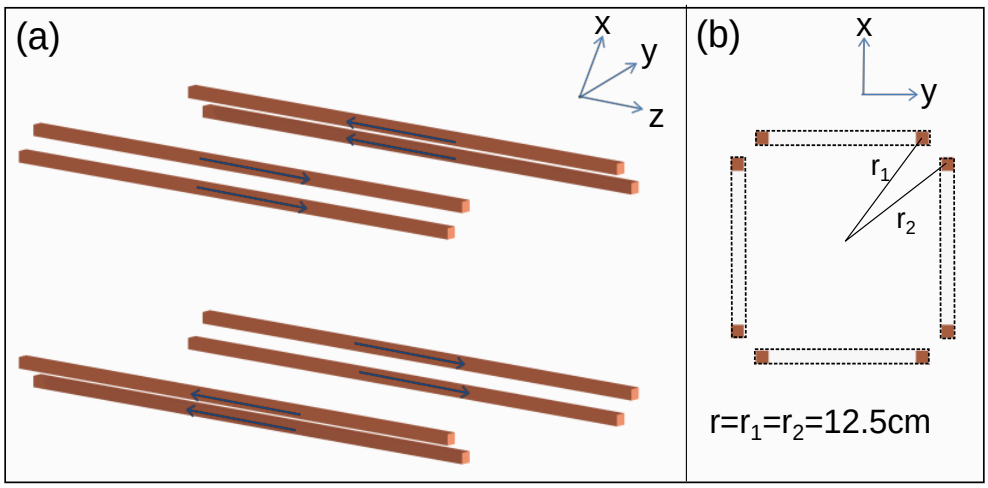

Figure 2.6: A system of eight infinite long conductors which generates field gradients similar to our system shown in figure 2.4. Each conductor has a rectangular cross-section and i is the current flowing through those, the direction of which is shown by black arrows.

to have our MOT coils outside the vacuum chamber to avoid any complexity in the system. Therefore, the separation between the top and bottom coil pair should be larger than the height of the vacuum chamber which is ≈140 mm. To maintain the symmetry of the magnetic field gradients, the separation of each coil pair (top-bottom and left-right coil pairs) should be nearly equal to the width of the coil. Also, the rectangular frame to hold the coil is designed in a way that its rectangular inner opening has a width bigger than the vacuum chamber height, so that it can easily slide over the chamber. This gives us flexibility to remove the

coils from the system if something goes wrong. The inner length l of the rectangular coil can be very large but we kept it 316 mm, otherwise the whole system would have become very big and bulky. The resistance of a coil is directly proportional to its length. Bigger the value of the resistance of coil, larger the amount of heat generation in the system, which in turn requires complicated cooling systems.

The size of our coil system is quite big and to achieve a gradient of 8-10 G/cm along x- and y-directions we need 30 A of current and 40 turns for each of the four coils. This high value of amp-turn product (IN=1200) is required because of the big size of our system which inturn is limited by the height of our vacuum chamber.

Field gradient estimation

In order to get an estimation of the field gradients generated by our coil system, we use a simple model. We simplify the problem by assuming that our coil system can be imitated by a system consisting of eight straight current carrying conductors each of infinite length arranged and oriented as shown in figure 2.6. The magnetic field due to a straight current carrying conductor is given by the following equation:

$$B = \frac{\mu_0 i}{2\pi r}, \tag{2.6}$$

where $\mu_0 = 4\pi \times 10^{-7}$ wb/A-m is the vacuum permeability, r is the distance of the infinite conductor from the point of observation and i is the current flowing through it. Therefore, the magnetic field gradient due to eight straight conductors is given by:

$$\nabla B = 8\frac{\mu_0 i}{2\pi r^2}, \tag{2.7}$$

or

$$\nabla B = Ci, \tag{2.8}$$

where C=0.01 G/cm-A is the geometrical constant of the system. This simple model shows that with i=1200 amp-turns we can achieve a gradient of $\approx$ 12 G/cm, which is high enough to make a MOT.

Field gradient simulations

In order to have a better estimate of the field gradients in x-, y- and z-directions, we simulated the coil system in the Radia software package (interfaced to Mathematica via Mathlink)[1].

[1]Radia is a software developed by European Synchrotron Radiation Facility (ESRF) to do simulation of magnetic systems. More details can be found on their website: `http://www.esrf.eu/Accelerators/Groups/InsertionDevices/Software/Radia`

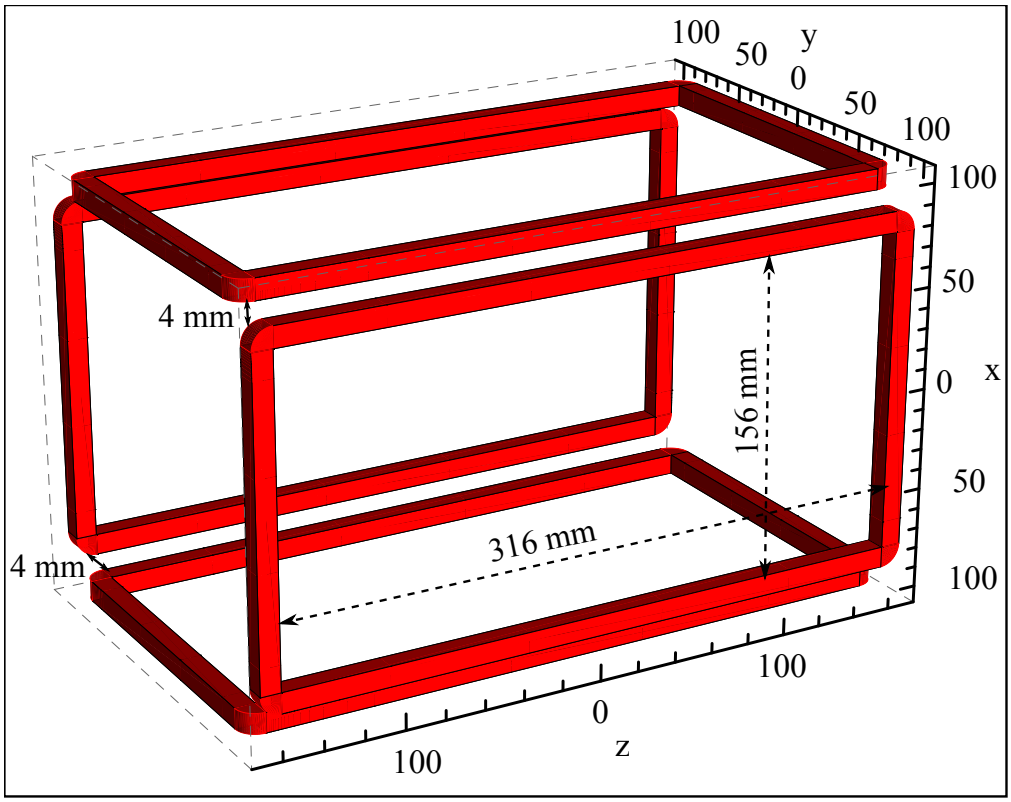

Figure 2.7: The magnetic field coils arrangement simulated in Radia software package.

Figure 2.7 shows the simulated rectangular coils arrangement. Here we simplify the calculations by assuming that each coil is made of a single turn of size 10 mm×14 mm, rather than forty turns of insulated copper strip. The inner length and breadth of each coil is 316 mm and 156 mm respectively. The current flowing in each of the four coils is i=1200 A, which gives a current density J=8.6 A/mm^2. The 4 mm space between the adjacent coils in both horizontal and vertical directions is left keeping in mind that we need rectangular frames to hold the coils in place.

Figure 2.8 shows the simulation results of the magnetic field gradient in x-, y- and z- directions respectively and the magnetic field strength in the x-y plane. This shows that by designing our coil system using the current dimensions and design parameters, a gradient of 8.54 G/cm in the x-y plane with a zero field along z-axis can be achieved. The Radia code of these simulations is shown in appendix 7.3.

Magnetic Coil Design

Our MOT field coil system consists of four coils, each of which has forty turns of copper strip of size 14 mm×0.25 mm. The dimensions of our coil design are shown in figure-2.7. The current density through

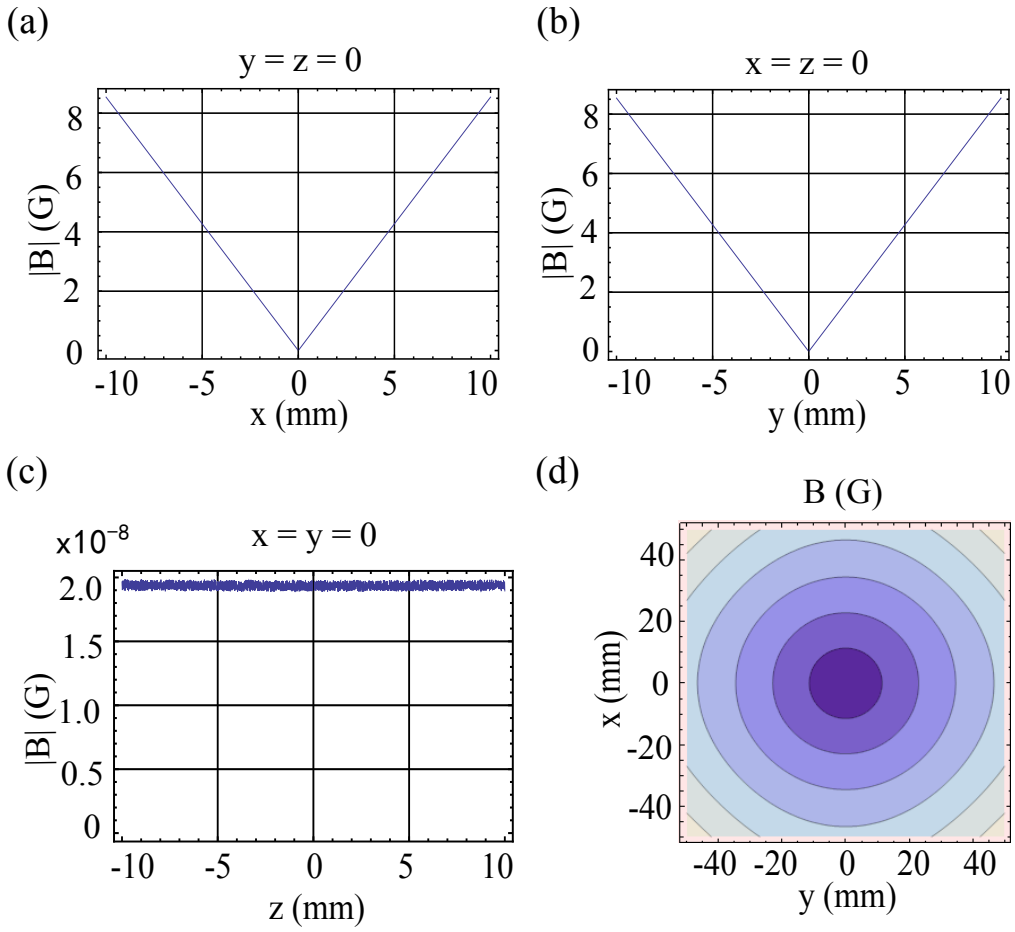

Figure 2.8: The magnetic field gradient simulation results for a current i = 1200 A and current density J = 8.6 A/mm^2 in each of the four rectangular coils, (a),(b) and (c) show the magnetic field variation with respect to position along the x-, y- and z-axis respectively. (d) shows the magnetic field strength in the x-y plane, where dark to light blue colour refers to lower to higher magnetic field.

each coil is given by $J = IN/A$, where A is the cross-sectional area of the rectangular coil i.e. 14 mm$\times$ 10 mm, this gives us a current density J=8.6 A/mm^2 for our coils. The copper strip has an insulation of kapton of thickness 0.023 mm. This keeps the coil turns insulated from each other and from the rectangular frame. Each of the four coils is wound on a rectangular structure. The coil turns are pressed against each other and wrapped tightly with the help of thermal conductive non-adhesive paste, to have an efficient heat transfer between different layers. The coils are designed to have a low value of inductance $L \approx$7 mH to achieve short switching time. The rectangular frames are designed with hollow cores for chilled water flux to avoid overheating of the coils. The water flux paths of all the four frames are connected in series using pipes and push in connectors (Festo, part number: NPQM-D-G18-Q8-P10). The design and dimensions of the rectangular frame are shown in the figure 2.9. There is a slit cut out from the rectangular frames to

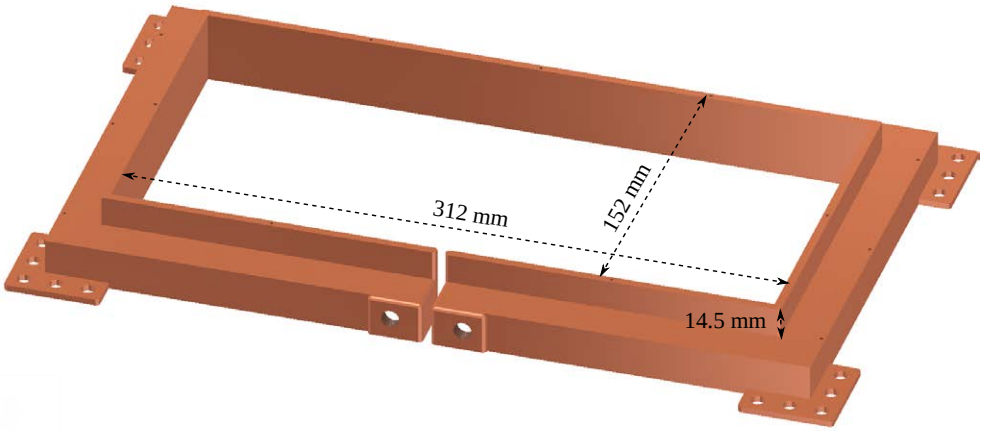

Figure 2.9: The CAD drawing of the rectangular coil frame.

avoid eddy currents. Each coil carries a current of I=30 A and turns N=40. All the four coils are connected in series and are provided power from a linear power supply, (Statron Geratetechnik: 3257.1, 0-36V/0-40A).

Figure 2.9 shows the CAD design of the rectangular frame. The actual size of the rectangular frame (with an opening hole of size of 316 mm×175 mm) is bigger than the design made in inventor (with an opening hole of size 316 mm×156 mm, this was a manufacturing fault). But this does not affect the actual field gradient in the x-y plane (8.5 G/cm at 30 A of current) in comparison to what is expected from the Radia simulations (8.54 G/cm at 30 A of current).

Figure 2.10 shows the pictures of the coil system assembly around the vacuum chamber. The vacuum system is baked and pumped out before installing the coils. The coil frames are made from copper and are very heavy. They are held on the optical table with the help of aluminum structure framing parts from Bosch Rexroth as shown in picture 2.10b.

Field-Gradient measurements

After assembling the coil structure, experimental measurements of the magnetic field (in all the three axis of interest) with respect to the distance from the centre of the system are recorded. We use a hall probe to measure the field at different positions. Figure 2.11(a), (b) show the variation of the magnetic field with distance from the centre in the x- and y-axis respectively, for a current of 20 A. These curves shows that the gradient values are constant in x- and y- directions up to a distance of 7-8 cm from the center and are given by B_x=5.4 G/cm and B_y=5.5 G/cm along the x- and y-axis respectively. For a current of 30 A, the field

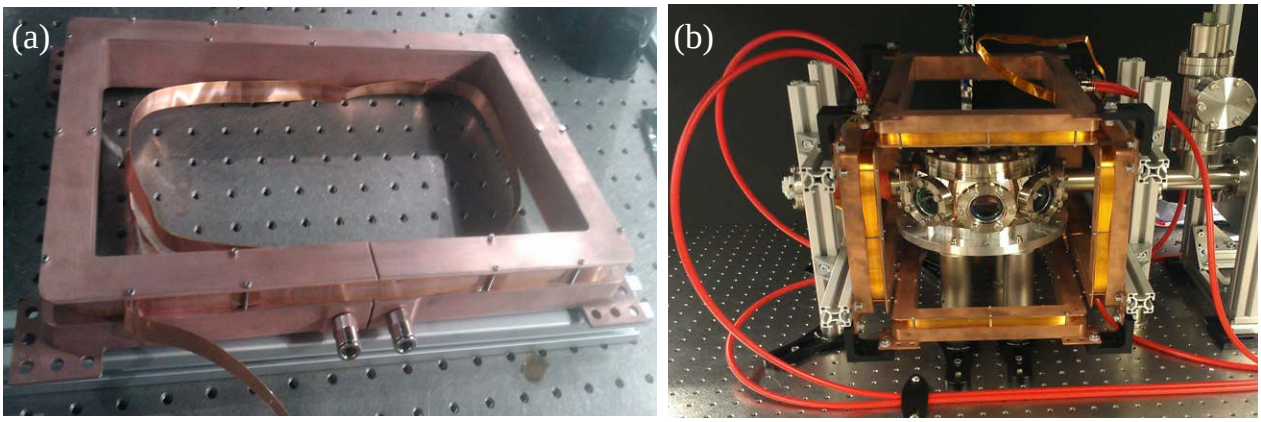

Figure 2.10: (a) Copper strip wrapped around the rectangular frame. The top plate is used to keep the coil well in place. The rectangular frame has hollow core for water cooling. (b) Magnetic field coils assembled around the vacuum chamber with the water cooling system installed.

gradient is around 8.5 G/cm (refer to figure 2.11(c)), this shows good agreement with the Radia simulation results.

Later in Section 6.3.1, it is shown that the effective number of atoms in the cavity mode starts saturating beyond a gradient of 9.46 G/cm. So our coils are capable to provide sufficient gradient to achieve a high N_{eff} of the order of 10^6.

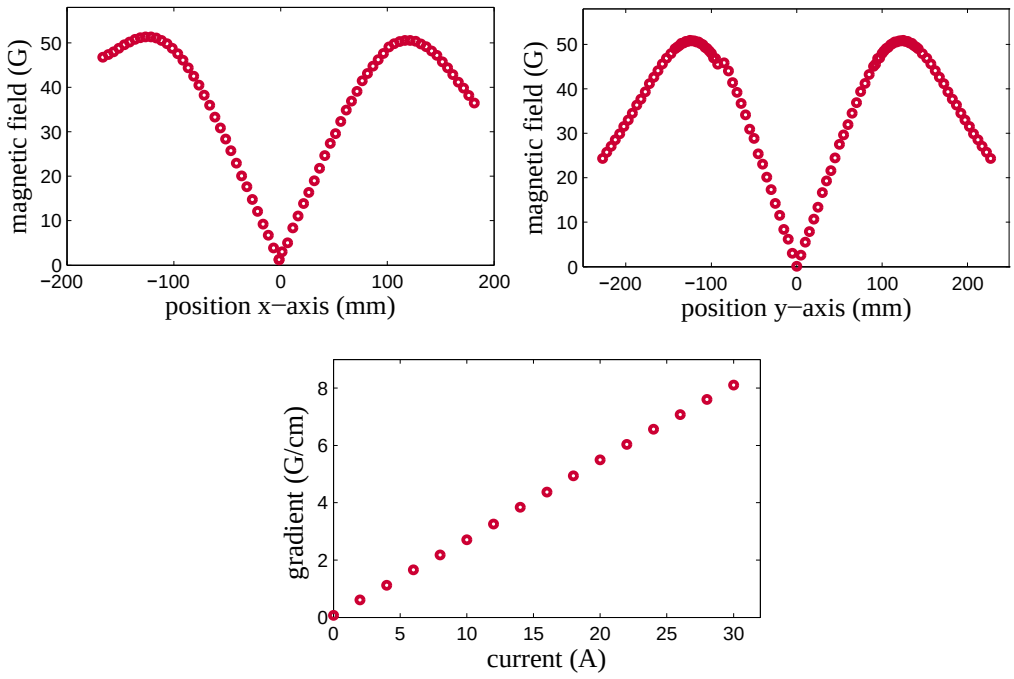

Figure 2.11: The plots (a) and (b) illustrate the variation of magnetic field generated by rectangular coil system verses position along x- and y- axes respectively, for a current of 20 A. The plot (c) shows that the field gradient is linear with the coil current upto 30 A.

CHAPTER 3

VACUUM SYSTEM

3.1 Introduction

At atmospheric temperature and pressure the atoms and molecules of a gas are randomly moving in different directions with high thermal velocities and are colliding with each other. In order to cool and trap atomic clouds at ultra low temperatures of the order of $<$ mK, we need to isolate the system containing the target atoms (potassium-39 in the present context) from thermal atoms and molecules present at room temperature and pressure. Otherwise, thermal atoms and molecules will keep on transferring their energy to the target atoms by collisions and hence no cooling and trapping would be possible to achieve. For this purpose, we built a Ultra High Vacuum (UHV) system and loaded the atomic gas to be cooled inside it. The pressure inside UHV can be of the order of 10^{-11} mbar. This vacuum system is the heart of the whole experiment and rest of the components are designed and constructed around this.

In this chapter, I will describe in detail the assembly of our vacuum system. The very first and the most important thing was the planning and putting the thoughts in place for a feasible and realistic design according to the experimental goals, requirements and constraints. I appreciate the collective advice from other members of our group and my supervisor Jon's experience and skills in this regard and also the useful information found in these references [8, 16, 83]. I describe the step by step procedure we followed to build our UHV system in the following sections.

3.2 Planning and designing the vacuum system

For the sake of simplicity, we only wanted one main science chamber in our vacuum system with the ring cavity inside it. The main components, which needed to fit inside/ outside the science chamber or require space around it were: ring cavity, turbo and ion pumps, six free glass windows for MOT beams, optical access for imaging, potassium dispensers, electric connections for piezo of the cavity mirror and dispensers and piezo connector etc. The main constraint of our system was that we had a single chamber and all these components had to somehow fit to it together. The planning of the design included looking for off the shelf vacuum components from different companies, thinking about the problems that could occur while building and assembling the vacuum system and the possible solutions for these.

3.2.1 Conductance calculations

To create a vacuum inside a vacuum chamber, it is connected to a vacuum ion pump via cylindrical pipes to pump out all the gases present inside. The pumping rate (or volume flow rate) depends on the flow resistance R of the pipe. Flow resistance occurs because of the external and internal frictions. The external friction occurs because of forces between the inner surface material and the gas molecules whereas the internal friction is caused by forces among gas molecules (this is also called viscosity). In vacuum terminology, it is common to use the conductivity C (in the units of liters/second or meter^3/hour) of the pipe which is the reciprocal of the flow resistance R. The conductance of a piece of pipe in L/sec is measured by the following formula, which is valid for nitrogen (approximately 78% in air) at room temperature (295 K) [8, 15, 68]:

$$C = \frac{12.4D^3}{L + 1.33D}, \tag{3.1}$$

where L is the length of the cylindrical pipe and D is its diameter, both in cm. For pipes with bends or non-straight shapes, L is considered as the shortest length. If the vacuum chamber is connected to the ion pump using many pieces of pipe, then the conductance of each piece is calculated individually and the total conductance C is given by:

For pipes in parallel,

$$C = C_1 + C_2 + C_3 \tag{3.2}$$

For pipes in series,

$$\frac{1}{C} = \frac{1}{C_1} + \frac{1}{C_2} + \frac{1}{C_3} \tag{3.3}$$

where C_1, C_2, C_3.. are the conductances for individual pipes connected in the system. To achieve a good vacuum, the capacity of the ion pump which is usually specified in conductance (liters/second) should be higher than the conductance of the system. But, the ion pump should be used nearly to its full capability. For example, a pump of 40 L/sec is not suitable to pump out a system with pipe conductance 15 L/sec, one should rather use a 20 L/sec pump for such a system.

For our system, we planned to have two pipes (connected in series) connecting the vacuum chamber to the ion pump. Using the formulas described above the individual conductances came out to be around 8 L/sec each, giving a total conductance C=16 L/sec. The conductance of our ion pump is 20 L/sec, which is more than the conductance of our system.

3.2.2 Vacuum components and other accessories

All the vacuum components should be chosen with care. There are few standard tips which should be kept in mind when selecting and buying vacuum components and these are listed as follows:

1. All the components which are inside the vacuum should be made of low outgasing material e.g. stainless steel and should be vacuum compatible, cleanable and bakable up to a temperature of $> 200°$. The maximum baking temperature is decided by the component with the minimum temperature limit.

2. The use of copper should be limited in a vacuum because it has a high outgasing rate and is difficult to clean. Although the gaskets used to seal the CF flanges are made of copper. They should be properly cleaned with acetone and isopropanol before use. Copper is used to make gaskets as it is a soft metal and the knife edges of two CF flanges can easily be pressed against it to create a good seal.

3. In a vacuum, the use of organic materials like plastic and rubber should be kept to minimum. The use of ceramic and glass is fine. Glass should be used with care as high temperature gradients during baking may cause cracks in it.

4. Two pieces of the same material should not be screwed together directly. Some lubricant or gold plating on one of the pieces can be used for this purpose.

5. The use of iron and magnetic materials should be limited, especially if the experiment is sensitive to magnetic fields.

6. The use of epoxies is not recommended but in case of fixing the leaks, vacuum compatible epoxies should be used. Torr seal and vacseal are recommended and are being used in other vacuum systems

in our group. The use of glue inside the vacuum should be very limited as well. We use a vacuum compatible glue called Epotek (Kummer Semiconductor Technology, ETH74/3OZ) to fix the mirrors and piezo on the stainless steel ring cavity mount. The glue has to be cured before it can go into the vacuum chamber.

7. During design, you must make sure that you are not creating any virtual leaks. Virtual leaks are created by a trapped volume of air (which slowly outgases) which make it seem like there is some actual leak in the system. Virtual leaks are usually created by screwing into a blind hole. In that case make sure that the screws are vented (hole in the middle of the screw's head all the way along its length), so that there is room for the gas to pass from the hole to the pump. Sometimes dirty materials outgas a lot and behave like virtual leaks. To avoid this the vacuum components should be chosen with care and should undergo a proper cleaning procedure as explained in the next section of this chapter.

8. There are two kinds of flanges: rotatable and non-rotatable. With rotatable flanges one has more choices for different orientations. Combining a rotatable flange to a non-rotatable flange is normal and not very difficult whereas combining two rotatable flanges is challenging and needs experience.

Our vacuum system consisted of UHV compatible components which were mainly made of stainless steel material, conflat flanges and pyrex glass windows. The various flanges were joined to the main chamber using copper gaskets. The schematic of our vacuum system design is shown in figure 3.1. Our vacuum design consisted of a single spherical octagonal chamber from Kimball Physics (MCF600m-SphOct-F2C8 6.00) with eight 2.7"CF ports and two 6.00"CF ports. Six CF35 mini-view ports (from Torr Scientific, VPZ38BBAR-LN) each of clear aperture 1.26" were connected to six of the ports of the main chamber. The windows were made of fused silica and have four layers of broadband anti-reflection (BBAR) coating. Usually, BBAR coated windows are very delicate, hence should be avoided to use if not necessary. In our system these are required to use as we do not want reflection of the ring cavity probe and detection beams. The top window (from Torr Scientific, VPZ100BBAR-LN) of clear aperture 3.5" was joined to the port-9 and the bottom flange was connected to the port-10 of the chamber. The bottom flange was custom made and constructed by our internal machine shop. The ring cavity was mounted on the bottom flange using vented screws. Also, there was a feed-through connected to the bottom flange for the power connections to the piezo. Further details on the bottom flange are discussed in the section-3.4.

The ports 1,3,4,6,9 and 10 were reserved for optical access for the MOT beams, ports 2,3,4 and 5 for the cavity beams and the bottom window (port-10) for imaging the MOT florescence by a digital camera. The

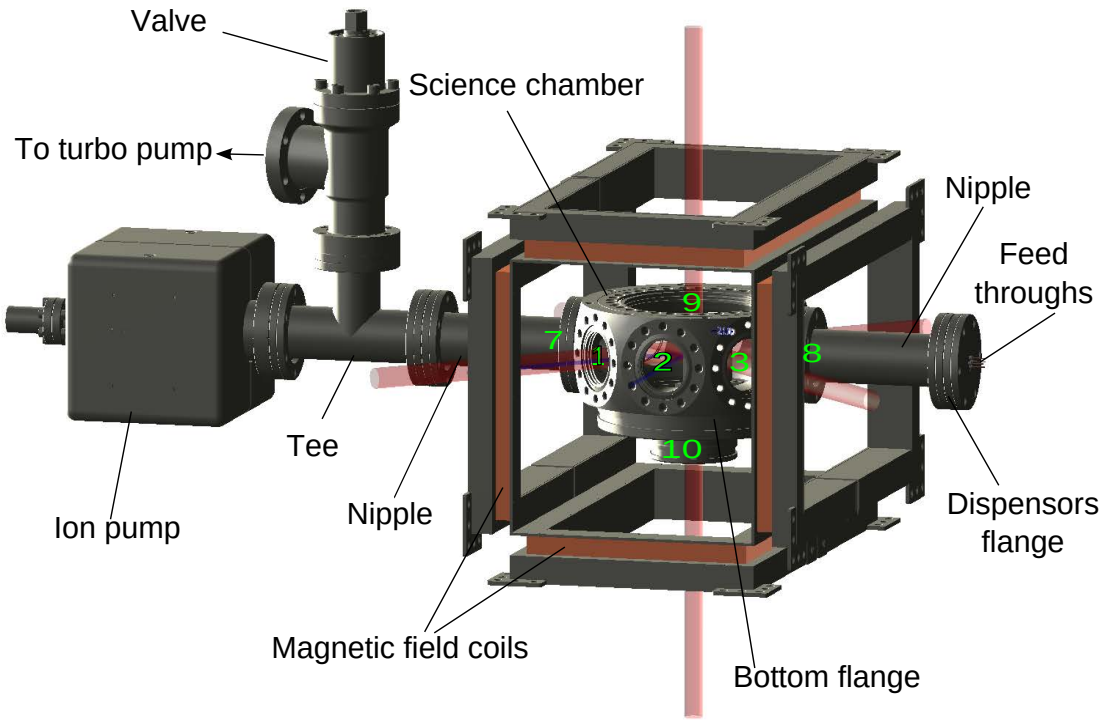

Figure 3.1: This figure illustrates the different components and the complete design of the vacuum system. Ports 1-3 and 7-10 of the octagonal chamber are labelled, ports 4-6 are at the back and are not visible in this figure.

port-7 was connected to a 2.75"CF nipple from Kurt J Lesker (FN-0275) and the other end of the nipple was connected to the dispenser flange. The dispenser flange had a feed-through power connector already installed to provide current to the dispensers. Section-3.5 contains detailed discussion on the dispensers flange. The last port number-8 was connected to the non-rotatable end of a 2.75"CF nipple from Kurt J Lesker (FN-0275) of length 4.93" and internal diameter of 1.5". There was a tee (Kurt J Lesker, T-0275-LN) and a DN40 UHV angle valve with CF-R rotatable flanges (from VAT Vacuum Products Ltd, 54132-GE02-0001) connected to the other end of nipple. The one end of the tee was connected to the rotatable end of the nipple, the second end was connected to the valve and the third end was connected to a Starcell ion pump of conductance 20 L/sec (bought from Agilent Technologies, 9191145 Vacion Plus 20). The other end of the valve was connected to the turbo pump (Pfeiffer, TSU071/MVP, 60 L/sec) via bellows. The system worked in such a way that when the valve was open the turbo pump was connected to the system and when it was closed then turbo was disconnected. The total conductance of the system depends on the path length L=L1+L2. Using equations 3.1-3.3 and the dimensions of the pipes as mentioned in the figure 3.3, we calculated the conductance of this

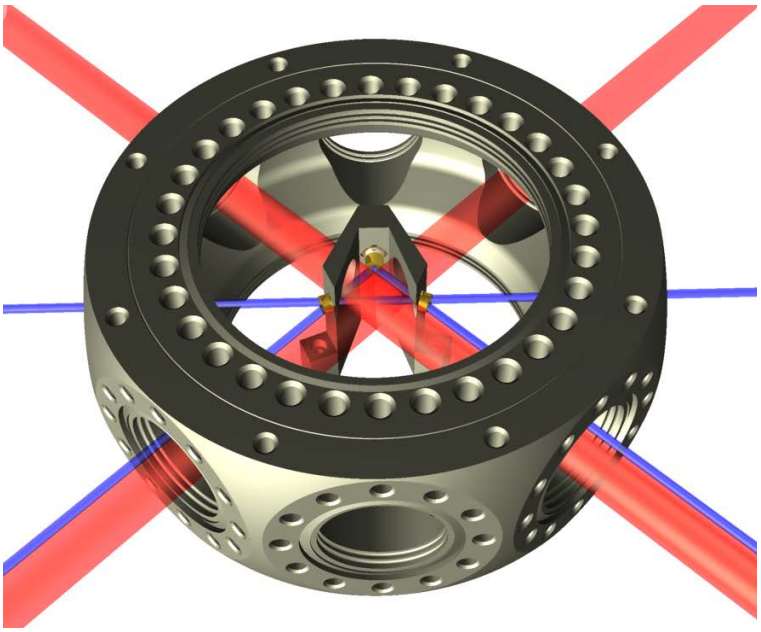

Figure 3.2: The CAD design showing the inside view of the science chamber. The thin blue coloured lines are cavity beam paths and the thick red lines are MOT beams paths. Here top and bottom MOT beam paths are not shown for clarity.

system.

$$C_1 = C_2 = 38.99 \text{ L/sec} \tag{3.4}$$

Therefore,

$$C = \frac{C_1}{2} = 19.49 \text{ L/sec} \tag{3.5}$$

Here, we have neglected the effect of the path available at 90° in the tee. This reduced the conductance of the system to the ion pump. According to these calculations, a 20 L/sec ion pump was good for our system.

The whole system was designed keeping in mind that there should be enough space for the MOT beams, cavity beams, optical access for the imaging cameras and the magnetic field coil system. There was space to install imaging system at the bottom of the vacuum chamber. The whole vacuum system was mechanically connected to the optical table by 20 cm long Thorlabs mounting posts.

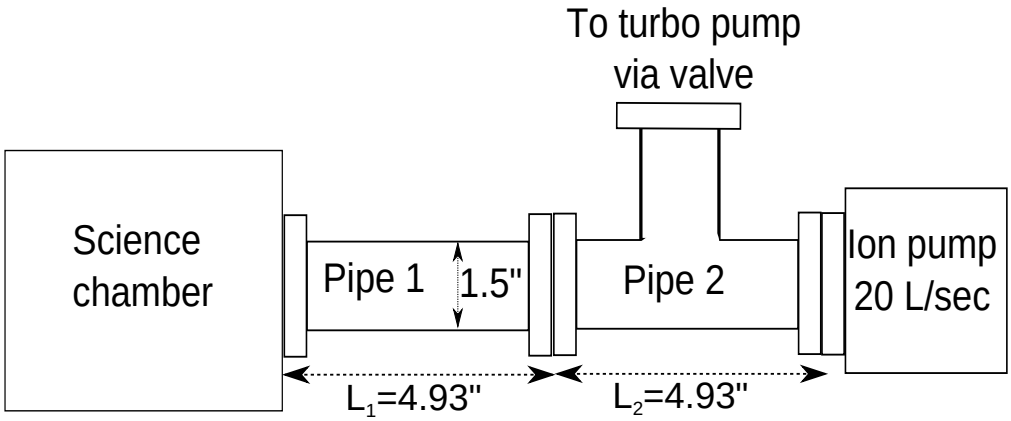

Figure 3.3: The Starcell ion pump is connected to the science chamber via a tee and a nipple. The total conductance of the system depends on the individual conductances of pipes 1 and 2. The diameters and lengths of both the pipes are same, hence they have equal conduactances. The total conductance to the ion pump is 19.49 L/sec.

3.3 Cleaning Procedure

All the components to be used in the vacuum assembly must be properly cleaned before use. This includes the main science chamber, Tee, bottom flange, ring cavity, valve, dispensers flange with feedthroughs, electric feedthroughs for piezo, nipples, ceramic beads, all the tools, screws, nuts and bolts. All the efforts done in cleaning, eventually decide the achievable pressure. Therefore, all the steps of pre-cleaning and general cleaning procedures should be followed properly.

Pre-cleaning steps:

1. Wash the components under running tap water.
2. Further, remove any visible dirt or gunk with Kimwipes (lens paper) and acetone.

General cleaning steps:

1. Ultrasound for 10 minutes in a soap solution (solution of Liquinox and water in 1:40 proportion).
2. Ultrasound for 10 minutes in distilled/deionised water. Distilled water is preferred over deionised water, but we used deionised water.
3. Ultrasound for 15 minutes in acetone.
4. Ultrasound for 15 minutes in isopropanol.

We cleaned the components with different solutions using ultrasound equipment. The ultrasonic generator has a space which is filled with tap water and a beaker containing the solution was placed inside it. This

makes a good ultrasound contact between the water and the beaker. The components which are ordered from vacuum companies usually come clean and undergo pre-cleaning and steps-2,3 and 4 of general cleaning. The components which are manufactured in the machine shop (the bottom flange, ring cavity and inline connectors) are usually oily, and must undergo all the steps of pre-cleaning and general cleaning procedures.

While in the ultrasound bath, one should make sure that all the parts are completely submersed in the solution in the beaker. Each time while repeating the ultrasound, a fresh clean solution should be used. Acetone is very harsh solvent and can dissolve a large range of dirt and contamination, however it evaporates leaving a residue behind. Isopropanol is comparatively less aggressive and it evaporates without leaving a residue behind. The knife edges of flanges should be checked carefully before cleaning. If there is any damage then the flange needs to be replaced. We used aluminium foil to store the cleaned parts. The use of oil free aluminium foil is recommended, but we used normal foil available on the market.

The windows and gaskets come very clean in the packaging and do not require the whole cleaning procedure. Before use we wiped the gaskets and the knife edges of the windows with acetone and then with isopropanol. The piezo came in a vacuum sealed packaging and did not require any cleaning. Also, the ring cavity mirrors did not undergo any solvent cleaning. The piezo and mirrors were glued onto the cleaned cavity and then pre-baked in an oven. The potassium dispensers were directly used with no cleaning or baking.

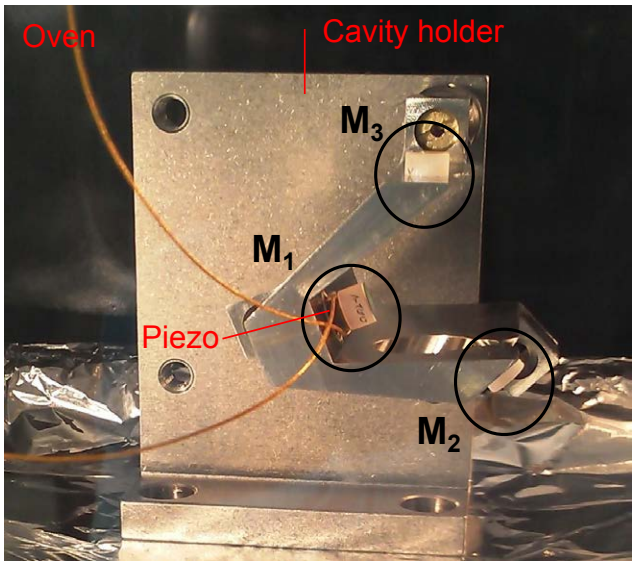

Figure 3.4: (a) The mirror M_2 glued to the ring cavity mount with Epotek epoxy and placed in an oven to cure the glue for 1 hour at 150°C. The cavity was held by a mount at the back, the central mirror M_1 was glued and cured before this.

3.4 Ring cavity and bottom flange assembly

3.4.1 Ring cavity assembly

The ring cavity mount was constructed by the machine shop. The mirrors were bought from Layertec GmbH with custom coatings and are UHV compatible. The piezo for the mirror M_1 was bought from Noliac (NAC2121-H6-C01). It was a UHV compatible piezo with a maximum baking limit 200°C and had wires insulated with kapton. We used Epotek glue to fix the mirrors and the piezo on the cavity mount. This glue has a curing time of 1 hour in an oven at 70° or 24 hours at room temperature. We chose the oven curing and repeated the curing procedure three times for three mirrors. There were three grooves on the cavity mount to glue the mirrors. The mirrors M_2 and M_3 (one at a time) were glued and set inside the grooves on the cavity mount. The cavity mount was then placed in a clean oven for curing for one hour at a temperature of 70°C. For the third groove, we first glued a disc shaped ceramic piece to it, then the piezo was glued on this ceramic piece and finally the mirror M_1 was glued on the piezo. This was then kept inside the oven for curing. The pizeo wires were connected to the electric feed-through using power inline connectors. This feedthrough was a multipin threaded and weldable feedthrough (Kurt J Lesker, IFTAG034031). The power inline connectors were from Lewvac (FHP-BECU-3IL-CON). We used ceramic beads (Kurt J Lesker, FTACERB056) to insulate the feedthrough pins for the flange and from each other.

3.4.2 Bottom flange assembly

The bottom flange was custom designed and constructed in the machine shop and then cleaned and assembled in the lab. This flange was designed to hold the assembled ring cavity on one side and a viewport on the the other. The bottom flange consists of a large DN100CF, 6"CF flange (MDCvacuum, 110025) and a small 2.75"CF flange. In the machine shop, these two flanges were joined together with a small cylindrical pipe. The cylindrical pipe was welded to these two flanges and an electric feedthrogh was attached to the bigger flange. There were three threaded holes on the bigger flange to mount the assembled ring cavity onto it using vented screws. Figure 3.5c,d shows the top and side view of the assembled bottom flange in the vacuum system.

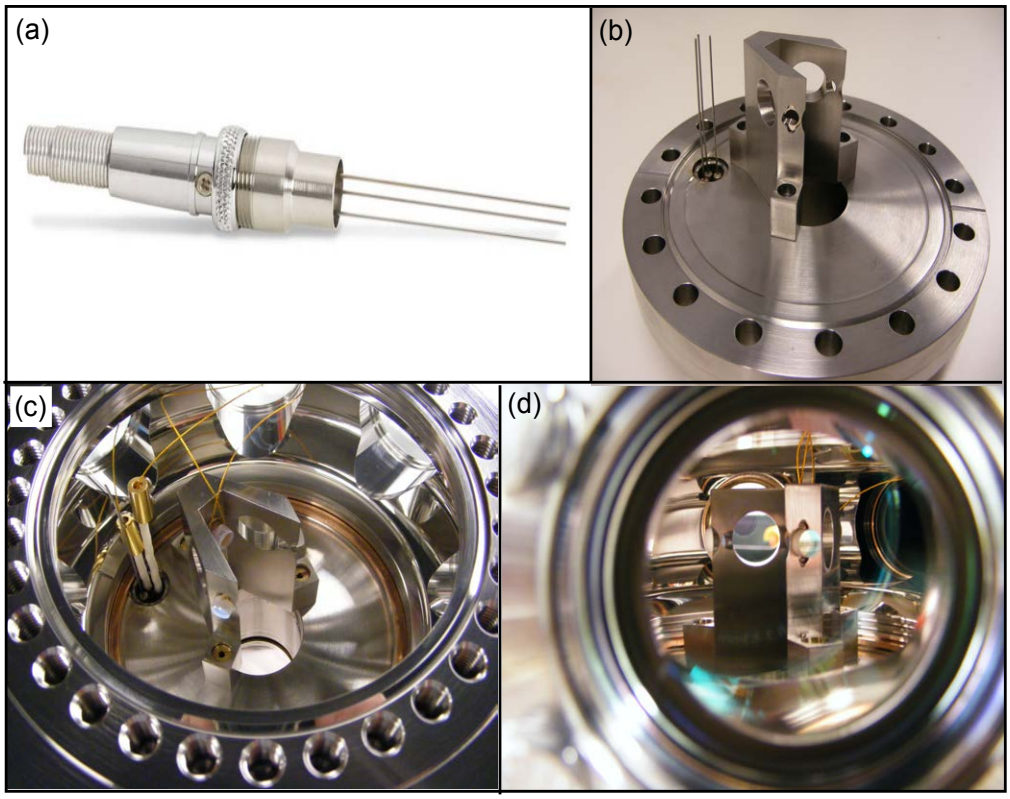

Figure 3.5: (a) The picture of the electric feedthrough for piezo which is welded to the bottom flange, (b) the bottom flange with the ring cavity mount connected to it, (c) the top view of the bottom flange through the science chamber, the ring cavity is attached to it with vented screws and the golden coloured inline connectors are used to connect the kapton coated piezo wires to the electric feedthrough pins and (d) the side view of the bottom flange through one of the 2.75"CF viewports of the octagonal chamber.

3.5 Preparing the dispenser flange

For dispensers, we used a DN35CF flange with an electric power feedthrough (Kurt J Lesker, EFT0043033) already installed on it. The coaxial electric feedthrough is made of copper pins passing through a ceramic material. Feedthrough is generally very delicate and can be easily damaged by mechanical stress, hence should be handled with care. The feedthrough had four pins, one served as ground and the rest of the three were connected to a positive voltage supply. We connected three potassium dispensers to these pins with the help of home built inline connectors as shown in figure-3.6. The potassium dispensers were bought from SAES Getters (K/NF/4.5/25 FT10+10). A dispenser (the one we used) looked like a thin trapezoidal shaped metallic body made with getter powder inside it. There was a slit along the length of the dispenser from where the potassium was released when the current was passed through it.

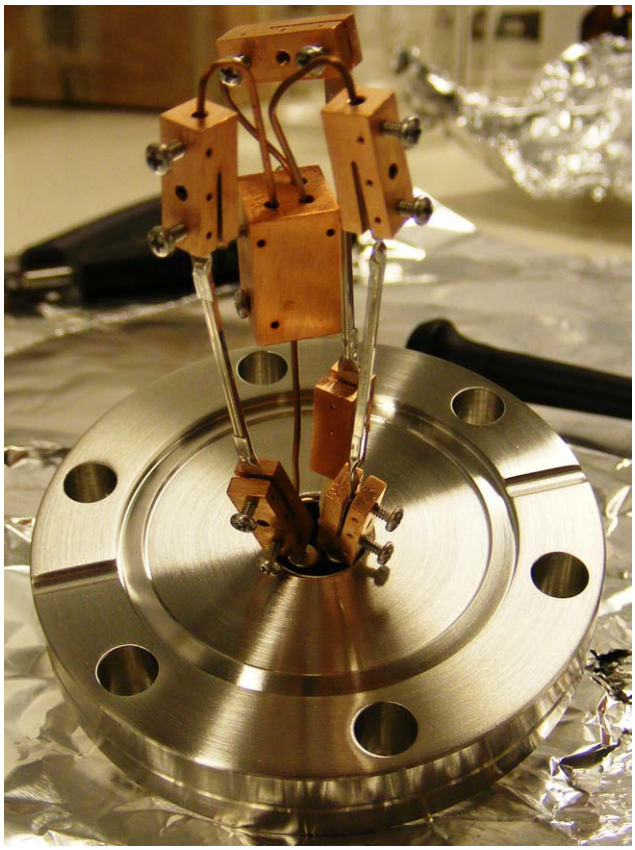

Figure 3.6: showing the potassium dispensers connected to the electric feedthrough's common ground and the +V pins on the dispenser flange. The big inline connector acts as common ground and the dispensers were connected to it via copper wires and small inline connectors. The three small inline connectors at the bottom connected the three +V pins of feedthroughs to the dispensers. The dispensers and bottom inline connectors were spaced well away from each other so that there was no electric connection between them. Only a single dispenser was used during the experiment at any one time.

3.6 Vacuum assembly procedure

Firstly, we cleaned and prepared a work space for the assembly of the vacuum chamber. We then assembled all the windows and bottom flange to the science chamber. After that we connected the tee, nipples, valve, turbo pump, ion pump and then finally the dispensers flange as described before in section:3.2. Before sealing the windows or flanges, we wiped the knife edges with acetone and then with isopropanol. Similarly, we wiped the inner glass surface of the windows as well. The copper gaskets were also wiped with the same solutions. To seal any two conflat components together, a gasket was pressed between their knife edges and then screws were finger tightened. We applied a small amount of thread lubricant/anti-seize (Kurt J Lesker, VZTL) on the screws/bolts threads before screwing them in. For a good and even seal, the screws/bolts should be tightened with the help of a torque wrench and in a particular fashion as shown in figure 3.7. An equal and

small amount of force (<20 N or 1/16th of a full turn of the wrench) should be applied on each screw in each cycle. There should always be a small space left between the flanges after sealing.

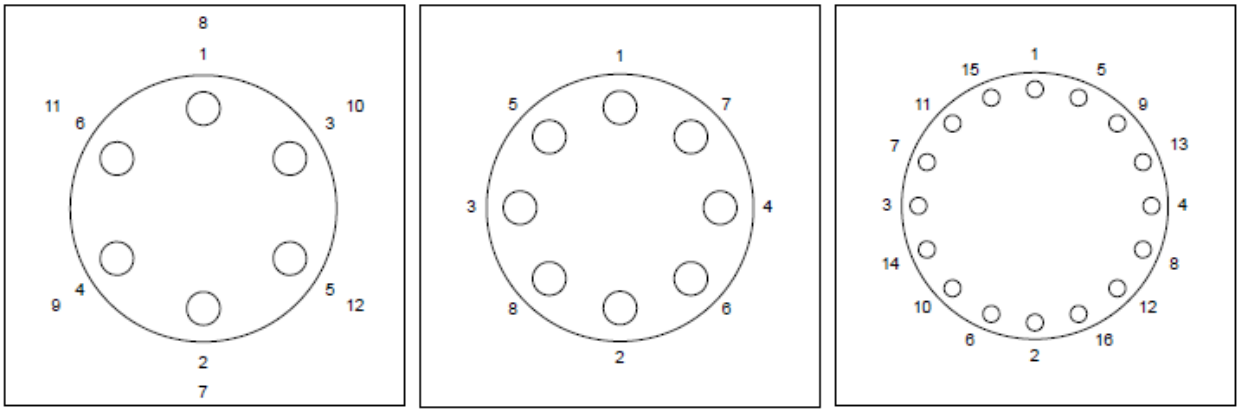

Figure 3.7: The screw tightening pattern to seal two ConFlat flanges having (a) six, (b) eight and (c) sixteen bolts/screws [8].

The turbo pump is connected to the chamber via bellows. The bellows should be pre-cleaned and baked before getting exposed to the chamber. The bellow has a 2.75"CF flange which joins to the valve.

3.7 Pumping and baking the system

In this section, I firstly describe the general pumping and baking procedures, I then explain the leak problems which we encountered during the pumping and baking of our system and how we fixed these.

After the vacuum system was fully assembled, we started pumping it down with a turbo pump. We used the turbo pump to bring the pressure down from the laboratory atmosphere pressure to $\approx 10^{-8}$ mbar. An ion pump can go down to a pressure of 10^{-13} mbar depending on the factors like conductance C of the system, how good the assembly is, virtual leaks and outgasing rate of the materials inside and vacuum chamber walls. There was a digital gauge (Pfeiffer, PTR21251) used with the turbo pump to read out the pressure in the chamber. We opened the valve and then switched the turbo pump on. The current on the digital display of the pump referred to the pumping speed and how much stress the turbo was under when it was pumping out the gases. If the current does not go down sufficiently it means that there is a leak or system is highly outgasing. Once the pressure reaches $\approx 10^{-7} - 10^{-8}$ mbar, one can start baking the system to further lower down the pressure. The ion pump has to be baked and magnets must be removed prior to baking. To bake the system we used heating strips. We wrapped the whole system with few layers of aluminium foil for homogeneous heating. The windows were covered with a few layers of aluminium foil

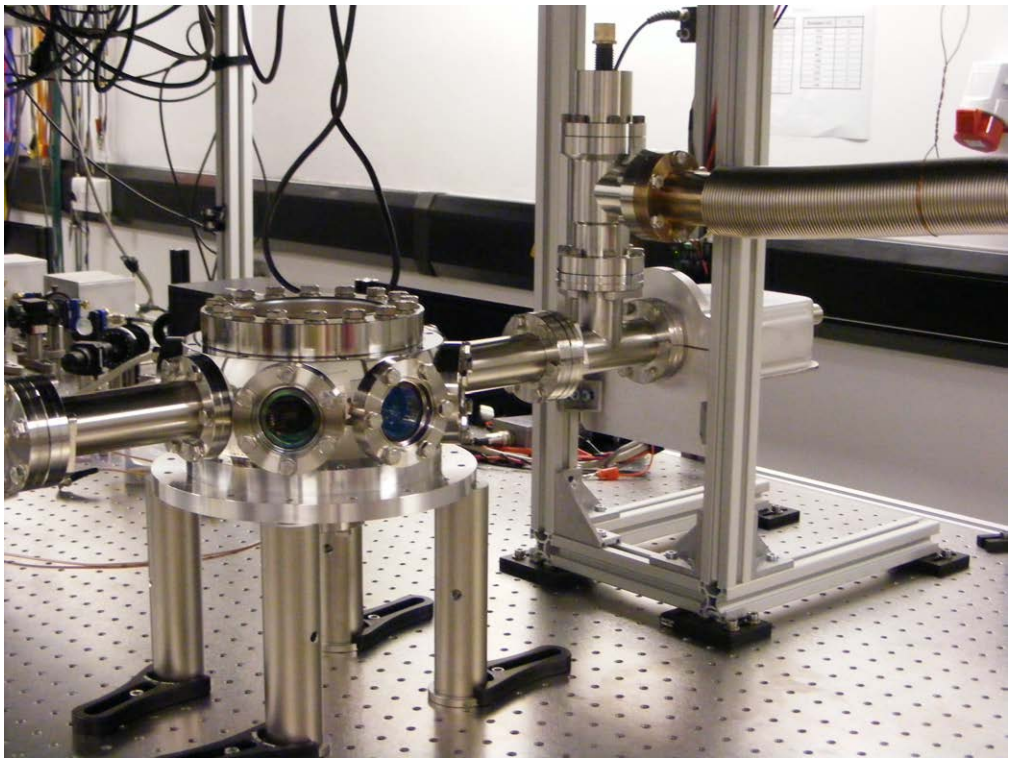

Figure 3.8: The picture of fully assembled vacuum system before baking and pumping.

to avoid direct contact with heating tapes. We used four heating tapes, the first two were wrapped over the science chamber, dispenser flange and both the nipples, the third covered the valve and bellow area and the fourth was wrapped around the ion pump. The temperature of the system was monitored and recorded using various temperature sensors which were especially connected near the glass windows, the ion pump and the dispensers flange. To maintain a uniform temperature, the current through different heating tapes was controlled separately. We varied the temperature of the system with a slow and constant rate to avoid any damage to the glass windows. The maximum baking temperature should be below the temperature limits of all the components used. After a few more layers of aluminium foil, we covered the whole surface with fibre glass sheets for insulation. And finally, it was wrapped with many layers of foil and was ready for a bake.

The first time we switched on the turbo pump, we could only go down to a pressure of 7.1×10^{-3} mbar. This indicated that there was a leak in the system. We tested all the windows and flanges by spraying acetone and monitoring the pressure on the pressure gauge. We detected a leak in the welded part of the cylindrical pipe connected to the bottom flange. We opened the system and tried to fix the leak by applying vacseal (Kurt J Lesker, KL-5) all over on the welded area. The vacseal requires a cure for a few hours in an oven at a temperature of 150°C. There was a slight improvement in the pressure value (this time 3.0 $\times 10^{-5}$ mbar),

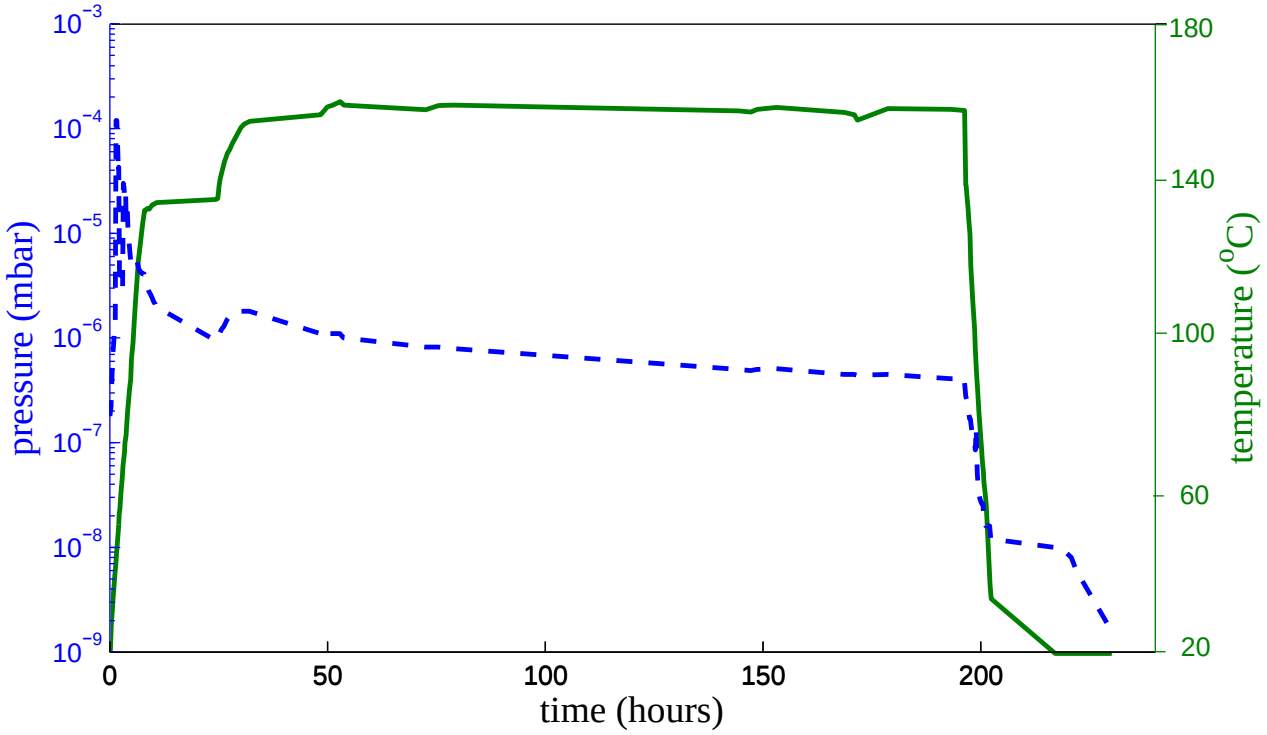

Figure 3.9: The graph showing the pressure and temperature variation verses the time during baking.

but it was not good enough. The system was baked and we concluded that the pressure was not going down at all after a 24 hour bake. We decided to weld a new cylindrical pipe of a smaller diameter to isolate the leaky outer pipe. After behaving well for a while, the inner pipe also developed a leak (pressure reading: 5.0×10^{-5} mbar). We filled the space between the inner and outer pipes with the vacseal and cured it for two days at room temperature. We also swapped the top window (connected to port 10) and bottom flange with each other, as it was convenient and easier to remove the bulky bottom flange from the top side than from the bottom. This time during pumping, the vacseal was sucked inside the small leak and finally the leak was fixed and the pressure reading on Pfeiffer vacuum gauge was 1.6×10^{-7} mbar. Hence, we started our second bake, figure 3.9 shows the trend of the pressure inside the vacuum chamber and the temperature verses time. Firstly, the pressure of the system increased because during the baking, the system was releasing many particles which were being pumped out by the turbo. After a few hours, when the temperature reached 50°C the pressure started decreasing. Our system got down to a pressure of 4.4×10^{-7} mbar at a temperature 157° (average of readings of seven different sensors, connected at different positions all over the system) while baking for ten days. Our maximum baking temperature was limited by what the piezo could handle without any damage (i.e. 200°C), hence we aimed to bake our system inbetween 150-180°C.

3.7.1 Firing the dispensers

After that, we planned to fire the dispensers. When we pass current through a dispenser for the first time, it releases a number of unwanted particles which are oxidised on its surface before potassium is released. We fired one dispenser at a time. We connected one of the dispensers to the power supply and passed a current of 1A, which did not seem to do anything. At 2A, immediately the pressure went up from 4.4×10^{-7} to 1.9×10^{-6} mbar and then it slowly came down to the same value within an hour. The dispenser was ready for use and we switched off the current through it. The same procedure was followed for the other two dispensers as well. Then we started cooling the system slowly by decreasing the current through the tapes. Alongside this, we planned to switch on the ion pump.

3.7.2 Burping the Ion pump

The ion pump is burped (switch on and off for couple of times), when it is used for the first time, and the turbo pump pumps out all the unwanted particles and substances released by it. While the system was still quite hot and the turbo was running with a pressure of 5.0×10^{-8} mbar on the Pfeiffer gauge, we unwraped the aluminium foil and the heating tapes from ion pump. The magnets were installed and we switched the ion pump on. The pressure on the turbo gauge shot up to 10^{-6} mbar and five minutes later it came back to 10^{-8} mbar. When the system was cooled down to 50°C, we removed all the foil, sensors and heating tapes. After a day, as ion pump was working fine and the current was going down, we closed the valve to disconnect the turbo pump from the system. The final current reading on the ion pump gauge was zero amperes which means the pressure of the system was as low as the ion pump could achieve.

3.7.3 Testing the dispensers

We switched on one of the dispensers by passing a current of 3A through it. We passed a laser beam (slowly scanning near potassium D2 transition) through one of the side windows of the science chamber. With the help of a viewer, a florescence of potassium atoms was observed along the laser beam. The florescence was seen with other two dispensers as well. This confirmed that the dispensers were working fine and our vacuum system was ready for the experiment.

CHAPTER 4

POTASSIUM SPECTROSCOPIC TECHNIQUES

The laser cooling and trapping of atomic species requires laser stabilisation near atomic cooling transitions with frequency fluctuations below the natural atomic linewidth (a few MHz for alkalis). Our MOT laser system consists of three home built, external cavity diode lasers (ECDL) in Littrow configuration. The frequency of the light emitted by an ECDL can drift due to fluctuations in the diode current or temperature of the laser. The laser frequency can be stabilised below the atomic linewidth using an error signal generated by a suitable sub-Doppler atomic spectroscopy method. The error signal should be dispersive shaped and approximately centered around zero volts. Using a proportional-integral-derivative (PID) feedback, we can stabilise a laser at a frequency corresponding to the zero volts of the error signal. Whenever the laser frequency fluctuates from its lock point, the voltage is shifted on the error signal. The PID loop inverts the sign of this voltage shift and feeds it to the laser in order to bring it back to the lock point.

There are a variety of well known spectroscopy methods to generate robust error signals for alkali atoms. Although there are a few groups using potassium species in cold atom experiments, there is not much work published on potassium spectroscopies for locking lasers. Therefore, we carried out a detailed study of various potassium spectroscopies near the D_2 transition at 766.7 nm. This work has already been published by our group and can be found in references [63, 69].

There are two main classes of atomic spectroscopies. The first class refers to modulation based techniques. These techniques use modulation and demodulation of light to generate a dispersion signal. We particularly focus on two different methods in this class: direct modulation and modulation transfer. Both methods utilise similar experimental set-ups but generate very different frequency discriminant signals. These techniques are very powerful but they require expensive modulators like Electro Optical Modulators(EOM) and radio frequency (RF) electronic components. The second class includes modulation-free techniques and

generally requires a simpler optical set-up and less electronics. In this class, we have investigated polarisation spectroscopy and a modified set-up of magnetic dichroism.

A typical error signal generated by atomic spectroscopy for laser stabilisation should have a linear slope crossing zero volts line near lock point. The figure of merits for laser stabilisation are determined by the slope, peak to peak amplitude, capture range and noise of the locking error signal. Here, the peak to peak amplitude is defined as the error signal height in volts. The capture range is a measure of the frequency range in the vicinity of zero crossing in which the sign of the error signal slope does not change. In this chapter I describe the study of various methods of potassium spectroscopies in detail and make a comparison between them based upon these parameters.

The outline of this chapter is as follows. In section 4.1, first the basics of Doppler broadened and saturated absorption spectra are explained for a two level atom system. Following this, the D_2 energy level diagram and properties of potassium are described. Then finally, the saturated absorption spectrum for potassium is discussed in details along with the optimisation of peak/dip heights and widths with respect to vapour pressure in the potassium cell (K-cell). In section 4.2, heterodyne spectroscopic techniques using direct probe modulation and modulation transfer from pump are explored. In section 4.3, modulation-free methods are performed which include polarisation spectroscopy and magnetic dichroism. Finally in section 4.4, a comparison between these spectroscopic methods is made based on their usefulness to effectively stabilise a laser.

4.1 Saturated Absorption Spectroscopy

4.1.1 Doppler broadening of spectral lines and Lamb dip

Consider a laser beam scanning through the resonant frequency of a two level atom, passing through a vapour cell and then entering a photodetector. The intensity I of the laser beam changes as it propagates through the sample of the resonant atoms. This change in the intensity of the laser beam is given by the amount of light scattered by the atoms per unit volume and is given by the following equation:

$$\frac{dI}{dx} = -\hbar\omega\gamma_p n, \tag{4.1}$$

where x is the direction of propagation of the laser beam through the vapour cell, n is the density of atoms in the cell, ω is the frequency of the laser beam. For a low intensity laser beam, the scattering rate is given

by:

$$\gamma_p = \left(\frac{s_0}{1+s_0}\right)\left(\frac{\gamma/2}{1+(2(\omega-\omega_0)/\gamma')^2}\right), \tag{4.2}$$

where ω_0 is the atomic transition frequency, $s_0 = (I/I_s)$ is the on-resonance saturation parameter, $I_\mathrm{s} = \pi\gamma hc/3\lambda^3$ is the on-resonance saturation intensity defined for a cyclic transition, λ is the transition wavelength, $\gamma' = \gamma\sqrt{1+s_0}$ is power broadened line width and γ is the half width half maximum (HWHM) of the atomic transition line. Equation 4.1 can be written as:

$$\frac{dI}{dx} = -\alpha I, \tag{4.3}$$

where the absorption coefficient $\alpha = \sigma_\mathrm{eg} n L(\omega)$, $L(\omega)$ is the lorentzian function of the laser detuning from the atomic resonance and σ_eg is the scattering cross section and is given by:

$$\sigma_\mathrm{eg} = \frac{\hbar\omega\gamma}{2I_\mathrm{s}} L(\omega) = \frac{3\lambda^2}{2\pi} L(\omega) \tag{4.4}$$

In the vapour cell, all the atoms move in random directions with velocities given by the Maxwell distribution $dn(v)$. Here, we are dealing with only the component of velocity parallel to the direction of propagation of the laser beam, which is denoted by v. The Maxwell distribution is given by:

$$dn(v) = \frac{n_0}{\sqrt{\pi}u} e^{-(v/u)^2} dv, \tag{4.5}$$

$$u = \sqrt{2k_B T/M}, \tag{4.6}$$

where n_0 is the total number of atoms, u is the most probable atomic speed, k_B is the Boltzmann constant, T is the temperature and M is the atomic mass of the atom. If an atom is moving with a certain velocity v then the frequency of the atomic transition in the lab frame is given by the equation:

$$\omega = \omega_0(1 + \frac{v}{c}), \tag{4.7}$$

where ω_0 is the resonant frequency of the transition. Thus the group of atoms moving with velocity v (parallel to the direction of propagation of the laser beam) will absorb blue detuned laser frequency $\nu > \nu_0$ and the group of atoms moving with velocity $-v$ (opposite to the propagation direction of the laser beam) will absorb red detuned laser frequency $\nu < \nu_0$. Therefore, the Doppler broadened spectrum can be formed by summing up the contributions from different velocity groups. The total absorption coefficient can be calculated by

taking the weighted contribution of all the absorption coefficients of different atomic velocity sub-classes. In the limit $\gamma << \Delta$, the resulting absorption coefficient for all the atoms is a Gaussian profile and is given by the following equation.

$$\begin{aligned} \alpha &= \alpha_0 \exp\left[-(\nu - \nu_0)^2/\Delta^2\right], \\ \alpha_0 &= \frac{3n\lambda^3\gamma}{4\sqrt{\pi}(2\pi\Delta)}. \end{aligned} \tag{4.8}$$

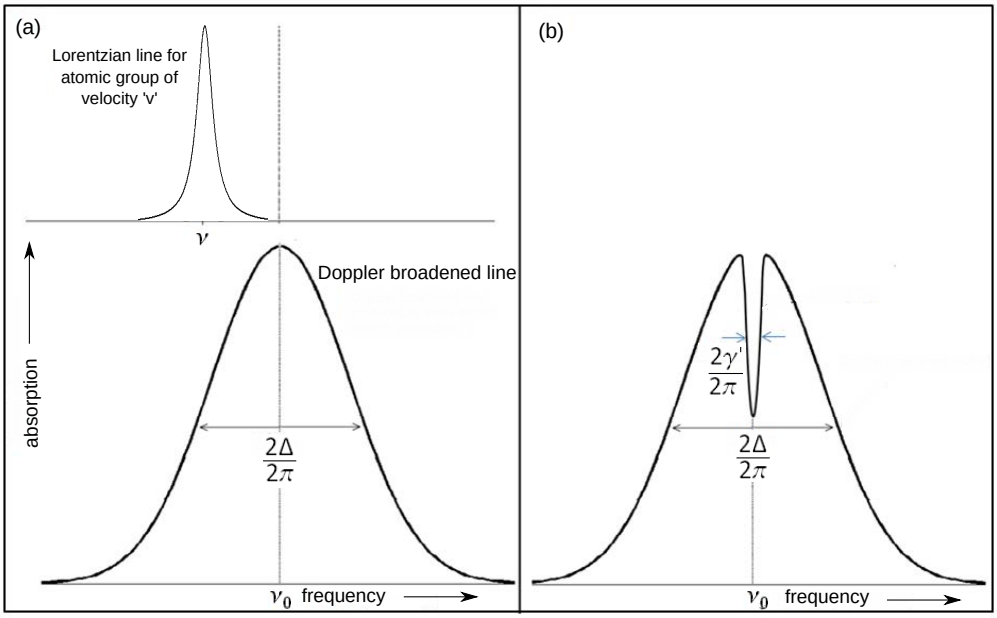

Figure 4.1: (a) The upper curve is the line shape for the atoms moving with a given velocity v. The lower curve shows the Doppler broadened profile as the weighted sum of the line shapes arising from all possible velocities. (b) Saturated absorption spectrum of a two-level atom showing the Lamb dip on the Doppler background. The width of the Lamb dip depends on power broadened linewidth $\gamma' = \gamma\sqrt{1+s_0}$.

The Doppler broadening of a spectral line of the atoms has a Gaussian profile as shown in figure 4.1(a). The half width half maximum (HWHM) of this line is a function of temperature and is given by:

$$\Delta = \frac{1}{\lambda}\sqrt{2\ln(2)kT/M}. \tag{4.9}$$

Lamb dip

The basic technique to obtain a sub-Doppler profile of a spectral line is saturated absorption [92, 36, 24]. In this technique, a relatively weak probe and a strong pump beam of the same frequency are counter-propagating through the atomic cell. The zero velocity group of atoms are resonant with both the beams

Table 4.1: Hyperfine constants for ^{39}K and ^{41}K for ground $^2S_{1/2}$ and excited states $^2P_{3/2}$. These values are taken from ref. [29].

Isotope	Natural abundance (%)	I	State	F	A	B
^{39}K	93.2581	3/2	$^2S_{1/2}$	1,2	230.868	-
			$^2P_{3/2}$	0-3	6.093	2.786
^{40}K	0.0117	4	$^2S_{1/2}$	9/2,7/2	-285.731	-
			$^2P_{3/2}$	5/2-11/2	-7.59	-3.5
^{41}K	6.7302	3/2	$^2S_{1/2}$	1,2	126.999	-
			$^2P_{3/2}$	0-3	3.363	3.351

along the optical axis. As the strong pump beam has pumped the atomic population into the excited state, the weak probe beam sees a reduced population in the ground state. This causes a reduced absorption of the probe beam near resonance and appears as a narrow dip (known as the Lamb dip [71, 5]) in the Doppler broadened background as shown in fig 4.1(b).

4.1.2 Potassium properties and energy level diagram

In cold atom experiments potassium is popular because of the existence of bosonic (^{39}K and ^{41}K) as well as fermionic (^{40}K) isotopes. Another reason is the easy availability of inexpensive semiconductor diodes at potassium cooling wavelength.

Potassium has only a single valence electron. Hence, the total electronic orbital angular momentum $\vec{L}$ and spin angular momentum $\vec{S}$ of the potassium atom are only due to this single valence electron. The spin-orbit coupling gives rise to the total angular momentum $\vec{J}$ of the atom and hence gives the fine structure splitting of the states. The different values of $\vec{J}$ lead to different energy states. The ground state and excited states are $^2S_{1/2}$ and $^2P_{1/2,3/2}$ respectively. The hyperfine structure is the splitting of fine structure levels due to the interaction of the nuclear spin $\vec{I}$ with the the total angular momentum $\vec{J}$.

$$\vec{F} = \vec{J} + \vec{I} \tag{4.10}$$

where F is the quantum number associated with angular momentum $\vec{F}$ and has values in the bound $(J-I) \leq F \leq (J+I)$. For ^{39}K and ^{41}K, the value of nuclear spin is $I = 3/2$. The hyperfine splitting of levels is generally small as compared to the fine splitting because of the small size of nuclear magnetic moment. The hyperfine frequency shift for a state with nuclear spin I and total electron spin J, is given by the following equation [59, 29, 34].

$$\Delta\nu_{hf} = \frac{1}{2}KA + \frac{1}{8}\frac{3K(K+1) - 4I(I+1)J(J+1)}{I(2I-1)J(2J-1)}B, \tag{4.11}$$

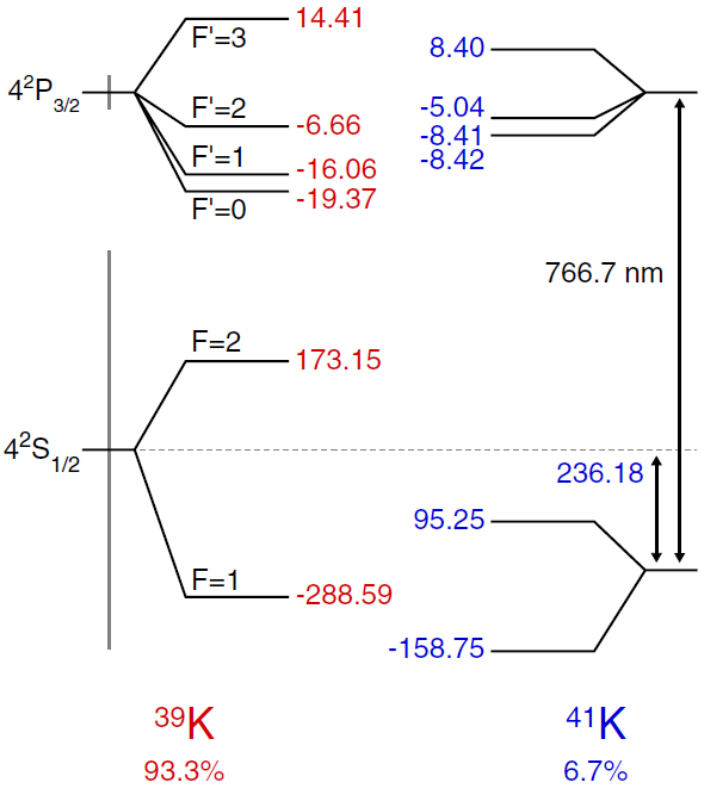

Figure 4.2: Energy level diagrams for D_2 lines of ^{39}K and ^{41}K isotopes. The frequency values for hyperfine levels are in units of MHz and extracted from [29]. On the left side, The grey lines crossing over the ground and excited levels show the Doppler linewidth ($\pm\Delta/2\pi$) and natural linewidth ($\pm\gamma/2\pi$) respectively.

where $K \equiv F(F+1) - I(I+1) - J(J+1)$ and A and B are hyperfine constants. The energies of different hyperfine levels, as shown in figure 4.2, have been calculated using the above equation. It is clear from this figure that the ground state splitting for potassium is comparable to the Doppler linewidth ($\Delta = 2\pi\times$390 MHz at 300 K), whereas the excited state splitting is very small and is comparable to the natural linewidth ($\gamma = 2\pi\times$3.017 MHz) [104].

4.1.3 Saturated absorption spectroscopy for potassium

For all the spectroscopic methods presented in this chapter, we use our home built ECDL. Later, the same laser serves as a reference for the MOT optical set-up which is described in the Chapter 5. The laser is scanning near 766.7 nm. The beam coming out of the laser is made circular using an anamorphic prism and the beam size is measured using a razor blade on a translational stage. The beam power is measured while razor (placed perpendicular to the optical axis) crosses the beam in horizontal/vertical direction. These

measurements provide $1/e^2$ radii along horizontal and vertical axes which are given by $w_{\rm h} = 1.18 \pm 0.03$ mm and $w_{\rm v} = 1.15 \pm 0.02$ mm respectively at a distance of 0.4 m from laser. After a distance 4 m the size of the beam is $w_{\rm h} = 1.59 \pm 0.03$ mm and $w_{\rm v} = 1.506 \pm 0.006$ mm. All the spectroscopies presented here were performed using this laser and at intermediate distances.

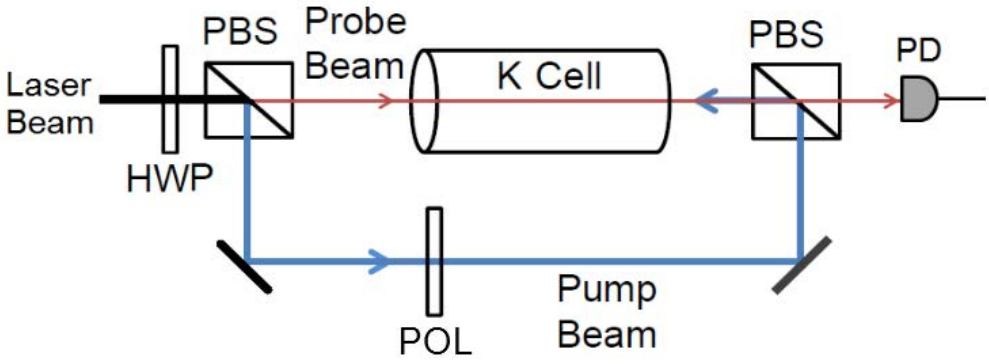

Figure 4.3: Typical lay out of our saturated absorption spectroscopy set-up. Here PBS=polarising beam splitter, PD=photodiode, POL=polariser and HWP=half wave plate.

The basic set-up of saturated absorption spectroscopy is shown in figure 4.3. It involves propagation of a pump beam and a probe beam coming from opposite directions and completely overlapping with each other in a potassium vapour cell (Thorlabs, CP25075-K) referred to as the K-cell. This is a 75 mm long, cylindrical cell made of pyrex and containing natural potassium. Potassium has a low vapour pressure at room temperature so the cell was heated using a flexible heater (Minco HK5464R14.6L12A) and then insulated using a thermal insulation wrapped around it. A thermistor (Minco S665PDZ40B) placed between the heater and cell is used to record the cell temperature. The probe is detected on a photodetector which gives the saturated absorption spectrum on a Doppler background as shown in figure 4.4(a). There are three main features for ^{39}K saturated spectrum. Each of the features A and C consist of a group of overlapping features, three appearing because of normal Lamb dips corresponding to $F \rightarrow F'$ transitions and another three appearing because of so-called crossover resonances between each pair of excited states. The negative feature B consists of two ground state crossovers and appears midway between A and C features. The existence of a negative ground state crossover can be understood as follows.

Suppose the laser frequency in the lab frame is at $\nu = (\nu_1 + \nu_2)/2$, where ν_1 and ν_2 correspond to the transition frequencies for $F = 1 \rightarrow F'$ and $F = 2 \rightarrow F'$ respectively. The pump and the probe beams are resonant with two opposite velocity groups $v_{\pm} = \pm c(\nu_2 - \nu_1)/2\nu$. For the velocity group v_+, the pump is in resonance with the $F = 1 \rightarrow F'$ transition and the probe beam is in resonance with the $F = 2 \rightarrow F'$

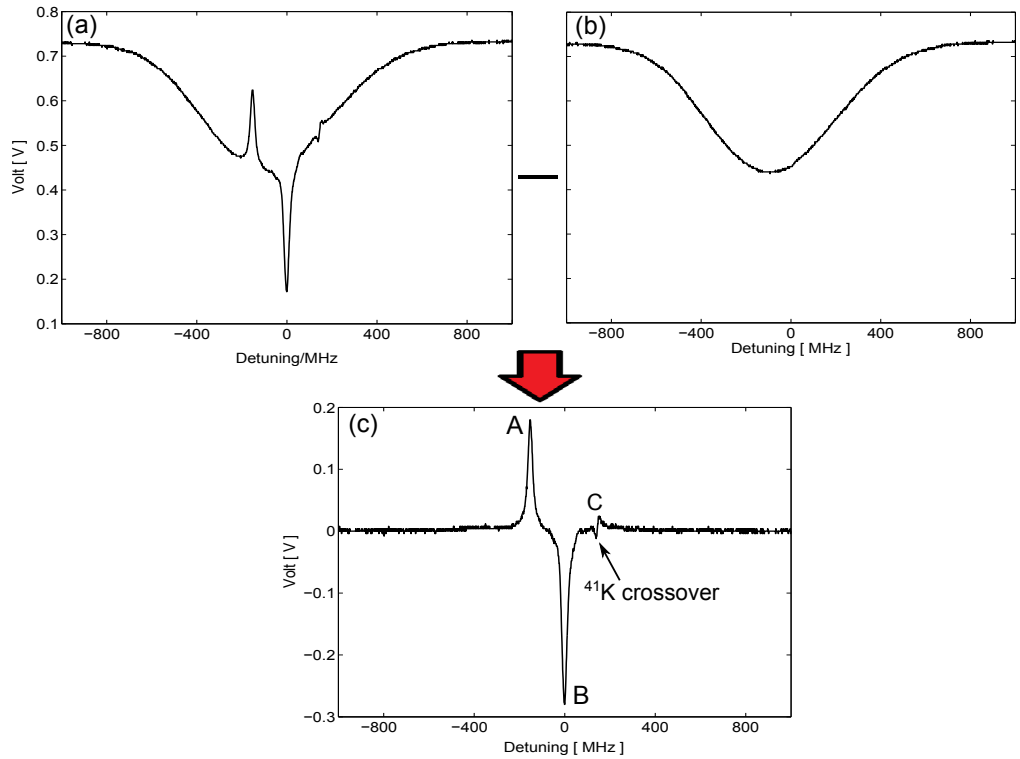

Figure 4.4: The Doppler free saturated absorption spectroscopy of Potassium D2 lines is obtained by subtracting the Doppler broadened background from the Doppler broadened saturation absorption signal. The spacing between features A and B is 224±4 MHz and is calibrated using a Fabry Perot cavity. This is used as a frequency scale for the whole experiment.

transition. The increased population of the $F = 2$ level due to optical pumping increases the probe beam absorption for this velocity group. On the other hand, for the velocity group v_-, the pump beam is resonant with the $F = 2 \rightarrow F'$ transition and the probe beam is resonat with the $F = 1 \rightarrow F'$ transition. Now, the increased population of the $F = 1$ level increases the probe beam absorption by the v_- group. Therefore, there is an enhanced absorption at ν giving rise to a crossover transition in the downward direction.

Since the isotope shift is small in comparison to the Doppler width, the associated Doppler profiles for all the transitions overlap and give rise to a single Doppler background. In this spectrum, the features for ^{40,41}K are not easily visible because of the low natural abundances of these isotopes (a very tiny feature of ^{41}K crossover is noticeable and is labelled in fig 4.4). The dominant features A and B are of interest and we focus on them for rest of the discussion.

The K-cell is heated to increase the vapour pressure and hence enhance the probe absorption which is evident from fig 4.5. The feature B corresponding to T=67°C is squashed because of the large background absorption.

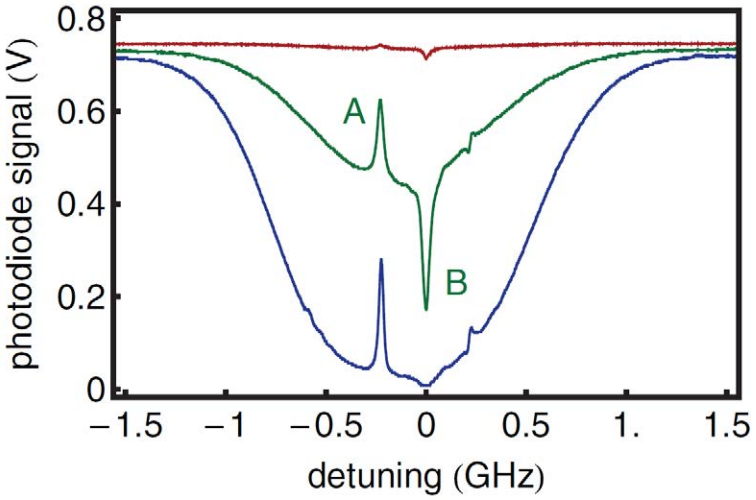

Figure 4.5: The saturated absorption spectra at three different temperatures 21°C (red trace), 50°C (green trace) and 67°C (blue trace). It is clearly seen that depth of the Doppler background and amplitudes of the absorption peaks or dips increase with rise in temperature.

We take a set of measurements to analyse the temperature dependence. At any particular temperature we record two different traces, one with the pump beam which is the saturated absorption spectrum on a Doppler background (as shown in figure 4.4(a)) and another without the pump beam, which is the pure Doppler broadened background (as shown in figure 4.4(b)). Subtracting these two, we get narrow A and B features on a flat background (see figure 4.4(c)). These features are then fitted with Lorentzian functions to obtain their heights and widths. A simple two level atom model is explained below to demonstrate the dependence of feature height and width on temperature. The transmission signal for a weak probe beam, whose intensity is less than the saturation intensity ($I_s = 1.75$ mW/cm^2) [96], propagating through a vapour cell is directly proportional to exp(-α), here α is the absorption coefficient. In the presence of a pump beam there exists a Lamb dip in the probe absorption coefficient, given as [71, 5]:

$$\alpha_{\mathrm{S}} = \alpha_{\mathrm{D}}(1 - \mathcal{L}), \tag{4.12}$$

where $\alpha_{\mathrm{D}} = a_{\mathrm{G}} P_{\mathrm{vap}}$ is the absorption coefficient without the saturating beam and is dependent on the vapour pressure (or temperature) of the cell. The parameter a_{G} is a constant for a given length of the cell. The Lorentzian function $\mathcal{L} = a_{\mathrm{L}}/(1 + \delta^2/\Gamma^2)$ represents the Lamb dip detuned by δ from the centre of the peak. The amplitude a_{L} and width Γ of the Lorentzian feature are dependent on the pump intensity. The equation

for Doppler free saturated absorption signal can be written as:

$$\Delta_{\mathrm{S}} = e^{-a_{\mathrm{G}} P_{\mathrm{vap}}} \left[e^{a_{\mathrm{L}} a_{\mathrm{G}} P_{\mathrm{vap}} / (1+\delta^2/\Gamma^2)} \right] \tag{4.13}$$

As temperature is a measure of atomic vapour pressure P_{vap} [13] therefore, equation 4.13 can be used to obtain the dependence of height and width on temperature.

Figure 4.6 shows the observed and theoretical temperature dependence of height and width of features A and B. The theory (from equation 4.13) agrees well with the observed trends. The height of feature B first increases with increasing temperature and peaks around 50°C and then squashed by deep background absorption (recall figure 4.5). Feature A has maximum height around 62°C. The widths remain almost constant until 50°C. The features are wider than the natural linewidth of 3 MHz, this is because both A and B features constitute a group of real and crossover transitions. After 50°C, the widths increase (decrease) for feature B (A), this is noticed for both our theory and experimental measurements. As our theory does not include temperature dependent mechanisms which could have broadened these features, therefore this behaviour can be attributed to the exponential nature of the transmission signal. This analysis shows that the optimum temperature is ≈48°C to obtain strong A and B features. Hence, for the rest of the work we keep the cell at this temperature. The depth of Doppler absorption background at this temperature is around 35-40% for weak probing. These results are dependant on parameters such as probe/pump intensities and the length of the vapour-cell.

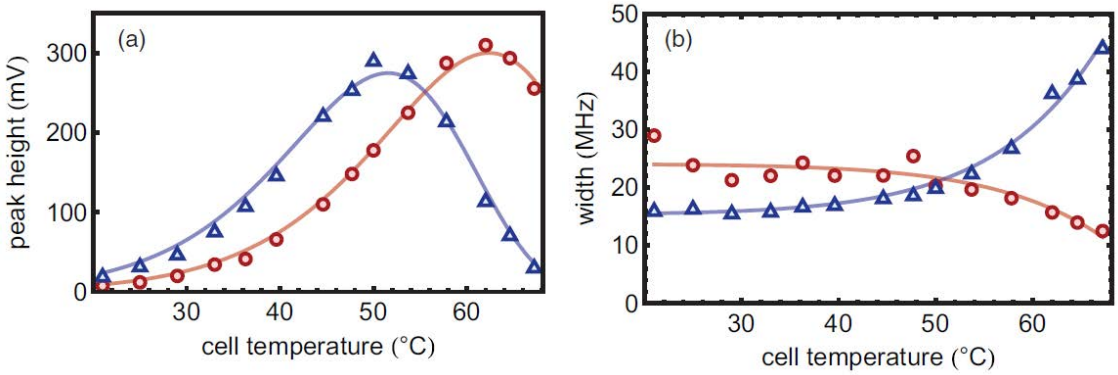

Figure 4.6: The temperature dependence of saturated absorption features. The cell temperature was controlled via the current passing through the flexible resistive heater wrapped around it. The pump and probe intensities were kept fixed at 20 ± 4 and 3.9 ± 0.7 mW/cm^2 for these measurements. (a) The peak to peak height (amplitude) variation with cell temperature, red circles are for the A feature whereas blue triangles are for the B features. The solid curves are theory plots from equation 4.13. (b) The variation of feature width (HWHM) with cell temperature.

For the laser stabilisation, we can lock at the side of one of the saturated absorption features by applying an electronic offset voltage, but these features are very sensitive to drifts in pump/probe powers, offset voltage and temperature. Hence, we consider saturated absorption spectroscopy as a frequency reference for other potassium spectroscopies discussed in this chapter.

4.2 Modulation based spectroscopies

This section describes two different spectroscopic methods based upon modulation of the frequency or phase of either the probe or pump beam [9]. We name the first method as *direct modulation* because the probe beam is directly modulated with a frequency of the order of natural linewidth. Whereas the second method is called *modulation transfer* where only the pump beam is modulated and its modulation is transferred to the probe beam via a non-linear process called *four wave mixing* [3].

4.2.1 Direct modulation spectroscopy

The set-up for the direct modulation (DM) spectroscopy is shown in figure 4.7(a) which is similar to what was presented in the reference [58]. In this technique, the phase or frequency of the probe beam is modulated and then the beam is passed through the atomic medium. The unmodulated pump beam propagates through the same medium but in the opposite direction. In our set-up both the beams are linearly polarised but orthogonal to each other to allow for easy combining and separating on polarising beam splitter. The pump beam interacts non-linearly with the atomic medium to cause different attenuation of carrier and side-bands of the probe beam. The differential absorption experienced by each side-band of the probe beam gives rise to the DM signal that is detected by an amplified silicon photodetector (Thorlabs PDA8A/M).

We used an electro-optic modulator (EOM) to generate modulation in the probe beam. This EOM device was designed by J Kronjaeger (a former member of the group) and was home-built using a $LiNbO_3$ crystal (Casix optics) of size 2 mm$\times$2 mm$\times$25 mm. The probe beam was passed through the Y-faces (anti-reflection coated) of the EOM crystal. The Z-faces were gold coated to be used as electrodes to apply an electric field across the crystal. The refractive index of the crystal depends linearly on the electric field applied across it which changes the path length for the light beam passing through it. By driving the crystal with an oscillating electric field of frequency (modulation frequency) ω_{m}, the dominant side bands ($\omega_{\mathrm{l}} \pm \omega_{\mathrm{m}}$) are obtained on both sides of the carrier (ω_{l}). A tunable resistor-inductor-capacitor (RLC) circuit along with an operational amplifier was used to generate the required driving field around the crystal. We choose a modulation frequency

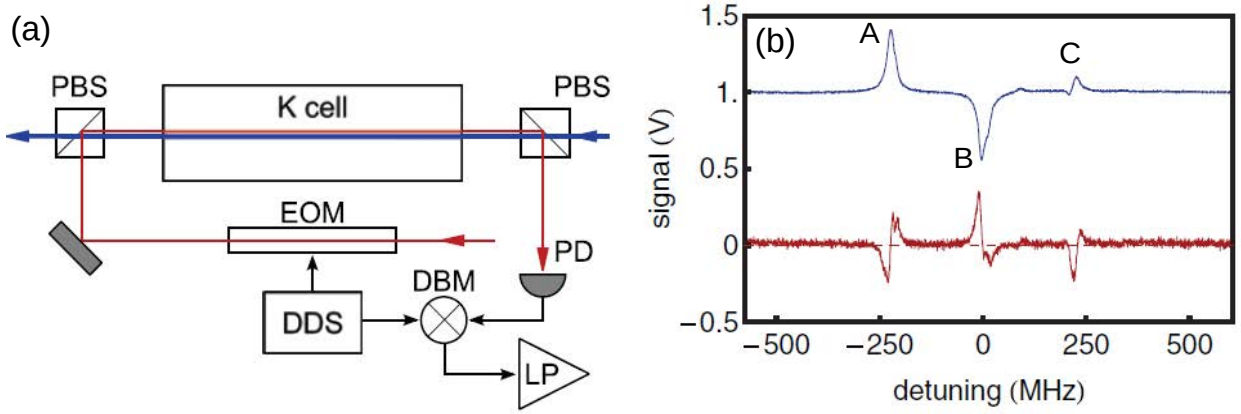

Figure 4.7: (a)A simplified set-up for the DM spectroscopy. (EOM= electro-optic modulator, DBM= double balanced mixer, LP= low pass filter, DDS= direct digital synthesizer). A telescope (not shown here) consisting two convex lenses each having a focal length $f = 150$ mm each, is used to focus the beams through the EOM. (b) The lower red coloured trace is the DM signal obtained at a modulation frequency of 9.62 MHz, with probe and pump intensities of 0.85±0.16 and 4.2±0.8 mW/cm^2 respectively. The upper blue trace is the background subtracted saturated absorption spectrum which is used as a reference here.

of ω_m=9.62 MHz, which is nearly half the linewidth of the saturated absorption features. This helps to attain a large slope and derivative like lineshape of the DM error signal [9, 11]. The photodetector output was fed to a bias-Tee (Mini-Circuits, ZFBT-4R2GW) to separate low and high frequency components. The low frequency component gave us the saturated absorption signal and was directly observed on an oscilloscope. The high frequency component was amplified using an amplifier (Mini-Circuits, ZFL-500LN) and then fed to a mixer. We used a direct digital synthesis (DDS) evaluation board (Analogue Devices, AD9959/PCBZ/ND) to generate two signals, one of which was used to drive EOM and the other was used as a local oscillator (LO) signal for a double balance mixer (DBM). The DBM (Mini-Circuits, ZRPD-1) is used to mix down the reference signal with the high frequency component of the photodetector signal. A low pass filter (Mini-Circuits, SLP-1.9+) was connected to the output of the DBM to remove the sum frequency signal. The LO power (set to 7 dBm) and phase were controlled by the DDS. For the larger LO powers (>7 dBm), the signal noise level was increasing without much gain in the signal amplitude.

In figure 4.7(b), the curve on the top is the Doppler free saturated absorption signal and is used as a reference here. The bottom curve shows the DM signal with lineshapes which look like the derivative of the absorption signal. The inner structures of the features A and B have shown up as kinks in this DM signal. An undesirable kink in the B feature appears near the zero volt crossing. This kink can be shifted away from the centre using suitable pump and probe powers. The C feature is relatively small in amplitude and asymmetrical around the zero crossing and saturates at relatively smaller pump/probe powers. Hence, we

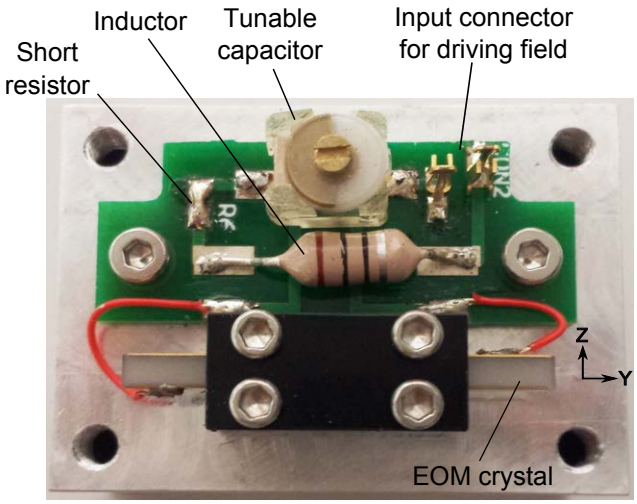

Figure 4.8: The EOM picture showing the RCL circuit and LiNbO crystal. We use inductor L=15 μH, resistor R=0 Ω and capacitor C=C_x+$C_{crystal}$ ≈17 pF. Here C_x=3-10 pF is the value of variable capacitor and $C_{crystal}$=10 pF is the capacitance of the crystal. The tunable capacitor is set to have a resonance frequency of 9.62 MHz for DM spectroscopy. This sets the Quality factor Q=37 at the resonance.

ignore it for the further analysis of DM spectroscopy. The trends of the feature slope and amplitude versus the pump power are shown in figure 4.9. For the A feature, the slope near zero crossing first increases with increase in the pump power and then it rolls down. This is because beyond a certain value of the pump power the saturated absorption amplitude starts saturating and the linewidth starts increasing leading to a decrease in slope for the derivative signal. A maximum slope of ≈70 mV/MHz is obtained near 1 mW/cm^2 pump intensity. For the B feature, a kink appears near the zero crossing for low pump intensities (to the left of blue line in figure 4.9(a)) leading to a small positive slope. The kink starts shifting away from the zero crossing after 0.85 mW/cm^2 and completely disappears as the pump intensity increases. This behaviour is also depicted in the amplitude variation as shown in figure 4.9(b). To the left of the dashed line, the amplitude of the B feature is very small and corresponds to the kink height. Whereas, to the right of this line, the amplitude is ≈300 mV_{pp} (peak to peak amplitude) and corresponds to the full height of the B feature. For the A feature, the amplitude first increases and then saturates with increasing the pump intensity.

Figure 4.10 shows the trends of slope and amplitude with the probe intensity variation keeping the pump intensity constant at 4.2±0.8 mW/cm^2. For both features, the slope and amplitude increase almost linearly with increasing probe intensity and we do not see any sign of saturation in our analysis.

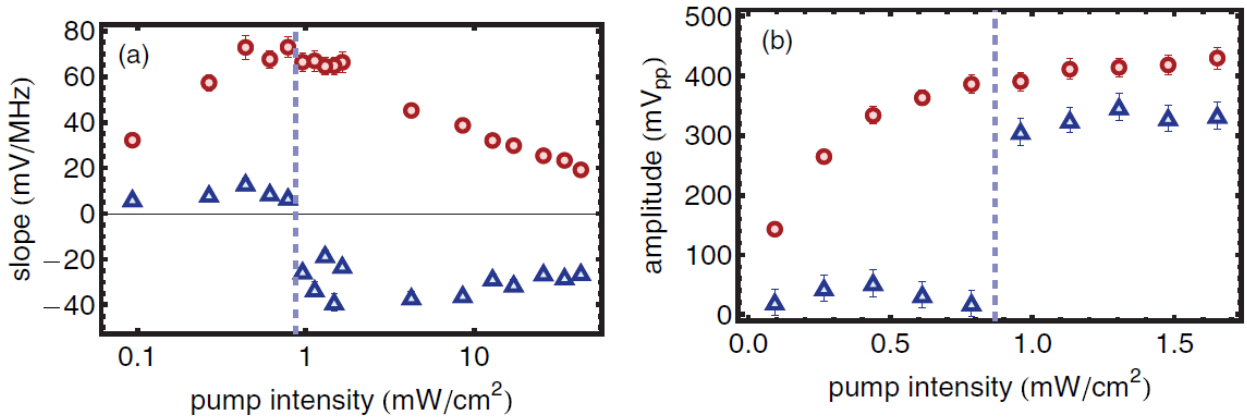

Figure 4.9: Dependence of DM signal with the pump intensity for the fixed probe intensity of 0.85±0.16 mW/cm^2. The red circles are for the A feature whereas blue triangles correspond to the B feature. (a) The trends for feature slopes. The dotted vertical line shows the turning point where the kink in the B feature starts moving away from the centre of the error signal. (b) The trends for peak to peak amplitudes. The vertical error bars correspond to the uncertainties from the data fitting.

4.2.2 Modulation transfer spectroscopy

In modulation transfer (MT) spectroscopy [87, 114, 58], the pump beam is modulated instead of the probe. The schematic for the set-up is shown in figure 4.11(a). The unmodulated probe beam acquires side-bands due to its interaction with the counter-propagating pump beam within the non-linear medium. This modulation transfer occurs because of the process known as four wave mixing [90, 27]. This arises due to the non-linearity of the absorbing medium characterised by the third order susceptibility, $\chi^{(3)}$. When two frequency components of the pump beam (such as the carrier and a side-band) combine with the probe beam, a fourth beam is generated as a side-band of the probe beam. This happens for each side-band of the pump beam. In this way, modulation gets transferred from pump to probe in the absorbing medium. These newly generated probe side-bands beat with the probe carrier to produce detectable signals. We used modulation frequencies of ω_m=1.82 MHz for this method, which is nearly half of the natural linewidth $\gamma/2\pi$=3 MHz. This selection was based on MT spectroscopy results for Rubidium published by other groups [58, 64]. We could not achieve a high Q-factor for our RLC circuit at this frequency because of the unavailability of suitable inductors. Therefore, we replaced the operational amplifier with one (Amplifier Solutions Corporation, ASC2832) having higher gain. The polarisation of pump and probe beams also play an important role to obtain a suitable MT signal. We tried circularly polarised pump (left hand circular) and probe (right hand circular) beams instead of linearly polarised beams. This enhanced the amplitude of the feature at $F = 2 \rightarrow F'$ to almost double at the cost of suppressing the B feature which was already very tiny. The polarisation dependence of MT

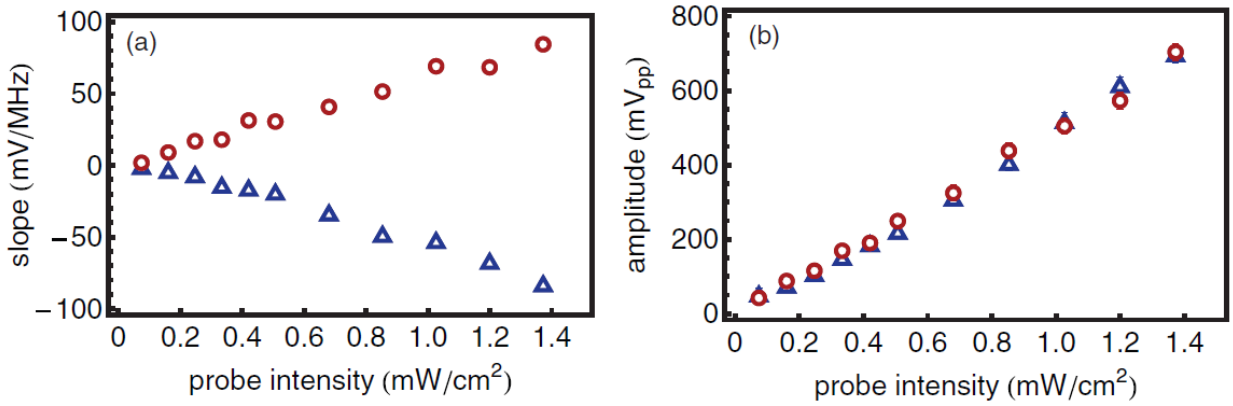

Figure 4.10: Dependence of DM signal with the probe intensity for the fixed pump intensity of 4.5±0.8 mW/cm^2. Red circles: A feature; Blue triangles: B feature. (a) The variation of feature slope.(b) The variation of feature amplitude.

signals for linear configurations of probe and pump beams has been previously studied and published in the case of ^{87}Rb [65, 114] but in our work we used a left-right circular probe-pump configuration to obtain the largest signal. For DM, using the left-right circular configuration did not give any enhancement in the signal amplitude.

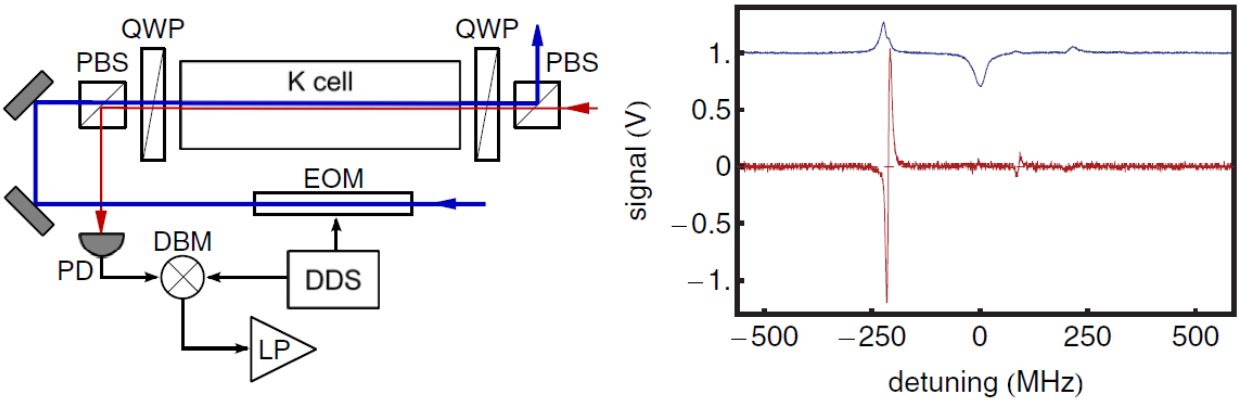

Figure 4.11: (a) A layout of the set-up to obtain the MT signal. The abbreviations for the components are the same as mentioned in figure 4.7. QWP refers to quarter wave plates.(b) An example MT spectrum (red trace) for the same pump and probe intensities as mentioned in figure 4.7. The modulation frequency used is 1.82 MHz. The saturated absorption spectrum (blue trace) is shown for comparison.

A typical MT signal is shown in figure 4.11(b). The weak four wave mixing process becomes more apparent for a closed transition due to scattering over multiple cycles [58, 65, 114]. Hence, it is very useful for locking to the closed transition if the spectrum contains a number of closely spaced hyperfine transitions. This is why our MT signal has the strongest feature near $F = 2 \rightarrow F' = 3$ line and almost negligible feature at the

crossover. This large MT feature is very narrow (corresponding to a single transition), symmetrical around the zero crossing and sits on a flat background. We will be only referring to this dominant feature for the rest of the analysis. Note that a small feature near $F = 2 \rightarrow F'$ line of ^{41}K is also noticeable and is slightly bigger than the ^{39}K crossover feature.

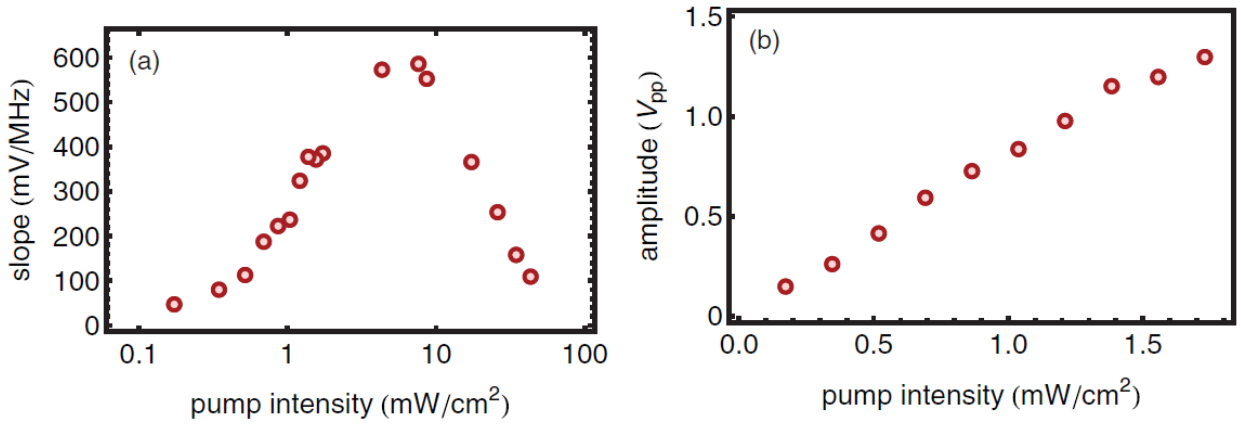

Figure 4.12: Dependence of the MT signal ($F = 2 \rightarrow F'$ feature) on the pump intensity. The value of fixed probe intensity used for these measurements was 0.85±0.16 mW/cm^2. (a) The trend for feature slope. (b) The trend for peak to peak amplitude.

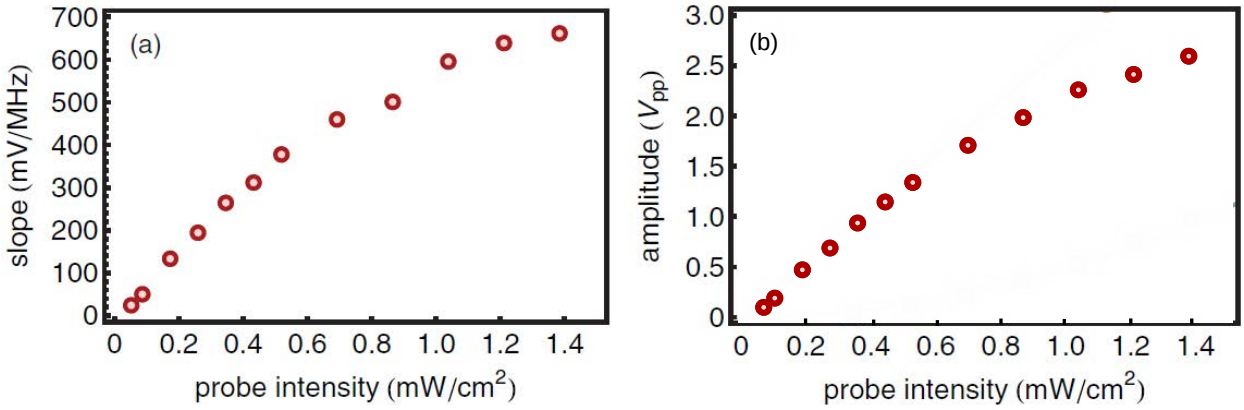

Figure 4.13: Dependence of the MT signal ($F = 2 \rightarrow F'$ feature) on the probe intensity. The pump intensity was kept fixed to 4.2±0.8 mW/cm^2. (a) The trend for feature slope. (b) The trend for peak to peak amplitude.

The pump intensity dependence of the MT signal is illustrated in figure 4.12. As expected, both the slope and amplitude of the MT feature first increase with increasing pump intensity and follow a linear trend near low powers. The slope peaks around 10 mW/cm^2 and then starts falling down due to line broadening as already explained for DM. In contrast to DM, the MT signal amplitude saturates at much higher pump

intensity and the slope is almost ten times bigger.

Figure 4.13 shows the trends of slope and amplitude of MT feature versus probe intensity at fixed pump intensity of 4.2±0.8 mW/cm^2. Both the slope and peak-peak amplitude first increase linearly with increase in probe intensity and then start saturating.

4.3 Modulation-free spectroscopies

There are many popular modulation-free spectroscopies widely used for laser stabilisation such as polarisation spectroscopy [109, 38, 91, 72]; Doppler broadened [50] and sub-Doppler magnetic dichroism [105, 73, 99, 39]; and Sagnac interferometry [82, 106]. In section 4.3.1, potassium polarisation spectroscopy is described. Firstly, we compare two error signals separately obtained by using a non-polarising beam splitter (NPBS) or a gold mirror in the experimental set-up. Then, the dependence of the amplitude and slope of the error signal on pump and probe intensities is described. Section 4.3.2 includes the discussion of two types of sub-Doppler spectroscopies using a newly modified set-up which are based on induced magnetic dichroism. Later, the sensitivity of the error signal to magnetic field and pump/probe intensity is described and a simple theoretical model is proposed to explain these trends.

4.3.1 Polarisation spectroscopy

Polarisation spectroscopy (PS) is based on the principle of inducing an optical anisotropy in the atomic medium by passing through a circularly polarised pump beam. This causes an asymmetric population distribution in the different Zeeman states of an atomic hyperfine level. A clever detection of the counter-propagating linearly polarised probe beam measures this anisotropy and generates sub-Doppler dispersion signals.

The schematic of our experimental set-up for PS is shown in figure 4.14. The pump and probe beams are derived from the same laser and are counter-propagating through the K-cell. The pump beam acquires circular polarisation after passing through a quarter wave plate (QWP). A small uniform magnetic field (B=22.8 mG) along the optical axis is produced using a solenoid wrapped around the potassium cell. This cancels out the effect of residual/stray magnetic fields and gives a flat background for the signal. A right circularly polarised pump beam will lead to σ_+ transition (with Δm_F=+1) This shifts the atomic population to higher m_F Zeeman sub-states of a ground level[1] [5]. Hence, a non-uniform re-population of the ground

[1]A m_F sub-state is the projection of total angular momentum quantum number F along the quantisation direction.

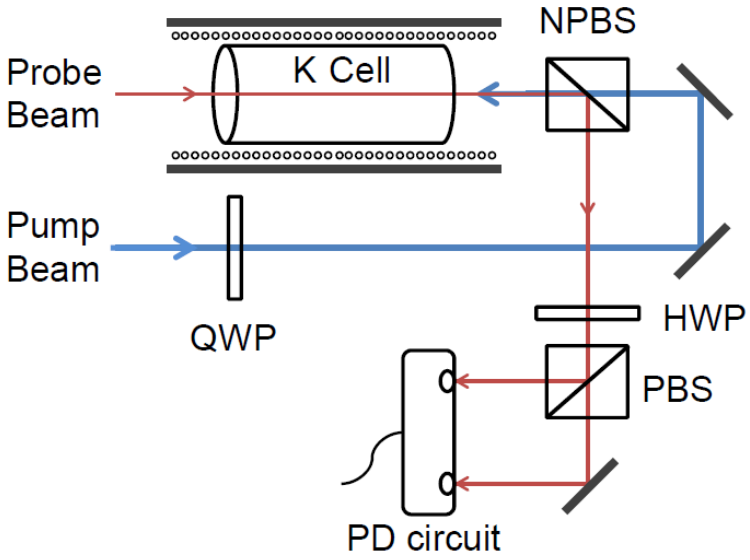

Figure 4.14: Schematic of the polarisation spectroscopy. A solenoid is wound around the K-cell and placed inside a magnetic shield. NPBS: non polarising beam splitter.

state Zeeman sub-levels takes place in the presence of a circularly polarised pump. This makes the atomic medium dichroic and birefringent. The counter-propagating linearly polarised probe beam is composed of two components of equal amplitudes but opposite circular polarisations. While passing through the atomic medium, the two circular components experience different absorptions and phase shifts due to pump-induced dichroism and birefringence. In the original PS by Hänsch and Wieman [109], the set-up consisted of a pair of crossed polarisers and a single photodiode for probe detection. Such a detection set-up gives PS features on a small Doppler background but with no zero crossing. Later, a different experimental set-up was introduced [72] in which the crossed polarisers were replaced by a HWP[1] and PBS to generate larger signal with zero crossing. Our set-up is similar to the later one. The HWP is used to set the axis of polarisation of the linearly polarised probe beam at 45^0 with respect to the axis of PBS. The two orthogonal outputs of PBS are then subtracted and amplified electronically by a homebuilt photodiode differentiating circuit to generate a difference signal. This circuit consists of two photodiodes, the difference of current passing through them is amplified with a transimpedance of 100 kΩ and design bandwidth of 720 kHz. In the absence of the pump beam there is no anisotropy and hence, the two outputs of the PBS are equal. This gives us a zero difference signal. However, in the presence of the circularly polarised pump beam, the medium becomes anisotropic and there exists a differential absorption $\Delta\alpha = \alpha_+ - \alpha_-$ and a differential refractive index $\Delta n = n_+ - n_-$ corresponding to induced circular dichroism and birefringence, respectively. Here $\alpha_\pm$

[1]We used 780 nm wave plates in our experimental set-ups for all the spectroscopies described in this chapter. These wave plates might have affected the polarisation states of pump and probe beams near potassium D_2 transition (≈ 767 nm).

and $n_{\pm}$ are the absorption coefficients and refractive indices, respectively, for the two circularly polarised components of the probe beam. The induced dichroism ($\Delta\alpha$) of the medium changes the polarisation of the probe beam from linear to elliptical, whereas the induced birefringence (Δn) rotates the axis of polarisation of the probe beam. Hence, the x- and y-components exiting from the PBS are different and one detects a difference signal with a zero crossing. The detected PS signal for a particular resonance and a weak probe beam has the form [72]:

$$\Delta V = V_0 e^{-\alpha L}\left(L\Delta\alpha_0 \frac{x}{1+x^2}\right), \tag{4.14}$$

In this expression, the birefringence in the cell windows is assumed to be negligible. Here $\alpha = \frac{1}{2}(\alpha_+ + \alpha_-)$, L is the length of the K-cell, $x = (\omega - \omega_0)/\Gamma$ is normalised detuning in units of the transition linewidth (Γ) which can be greater than natural linewidth γ due to power, transit-time and/or other broadening effects, V_0 depends on the intensity of the probe before entering the K-cell and amplification of the signal by the photodiode circuit, $\Delta\alpha_0$ is the value of $\Delta\alpha$ at the resonance transition frequency ω_0 which can be written as:

$$\Delta\alpha_0 = \alpha_+(\omega_0) - \alpha_-(\omega_0) \tag{4.15}$$

According to equation 4.14, the PS signal has a dispersive shape which crosses zero volts at the resonance frequency and returns to zero at large detuning on both sides of resonance.

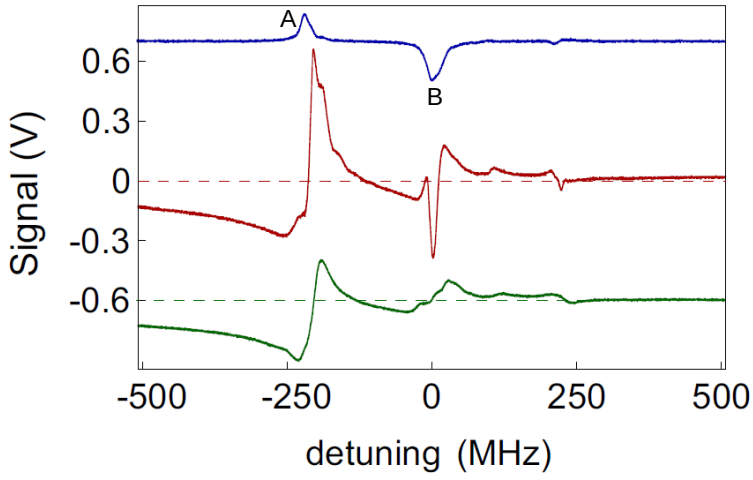

Figure 4.15: A comparison between the PS signals recorded with a NPBS (red trace) verses a gold mirror (green trace) in the set-up. A saturated absorption signal (blue trace) is shown on the top for reference. The blue and green traces are shifted up and down respectively for clarity.

Figure 4.15 shows the observed PS signal for potassium D_2 line. This spectrum has three main dispersion

shaped features with zero background. The blue trace is saturated absorption signal used as a reference here. The PS feature corresponding to the C feature is very tiny as expected. The other two features at $F = 2$ and the crossover are useful error signals for laser stabilisation. Therefore, we will only focus on these two features for rest of the discussion. The kinks in these features appear due to the internal structure of A and B as explained previously. The $F = 2$ feature is very large in comparison to the one at the crossover. This is because the $F = 2 \rightarrow F' = 3$ transition is a closed transition for a circularly polarised pump beam [72]. Both of these features have good capture ranges, reasonable slopes and peak to peak amplitudes and are therefore suitable for locking the laser.

Initially, we used a NPBS (50:50 splitter) in our optical set-up, as shown in figure 4.15. This allowed complete overlap of the counter-propagating pump and probe beams inside the K-cell. We found out that the NPBS (Thorlabs BS011) was not perfectly non-polarising as its design wavelength was in range 450-700 nm. This affected the polarisation state of reflected and transmitted beams and hence could have distorted the resulting PS signal. To solve this issue, we replaced the NPBS with a gold coated mirror. For the use of the gold mirror in the set-up, the pump and probe beams were required to be crossing each other at small angle inside the K-cell. We found this crossing angle to be 40 mrad in our set-up. Figure 4.15 shows a direct comparison between the polarisation spectra for the two set-ups under the same experimental conditions. The data for these signals were taken with probe intensity 3.8 ± 0.7 mW/cm^2 and pump intensity 5.6 ± 1.0 mW/cm^2. Including the gold mirror in the set-up solves polarisation issues but the crossing angle between pump and probe beams can lead to two potential problems. First is the residual Doppler broadening (estimated to be $\Delta_{\text{eff}} = (\theta/2)\Delta$) in the PS signal which is a function of crossing angle θ and single beam Doppler broadening ($\Delta = 2\pi \times 390$ MHz) for potassium-39 at room temperature. This comes out to be 8 MHz for a crossing angle of 40 mrad in the present case. This Doppler broadening is significant in our case considering the compact frequency structure of our features. Second, the smaller effective area of pump-probe overlap which results in an overall decrease in the signal in comparison to the one obtained by NPBS set up. With the gold mirror set-up, the $F = 2$ feature is very small and the crossover feature almost disappears. It is evident from this comparison that the signal looks much better using the NPBS instead of a gold mirror. Therefore, the rest of the analysis for PS uses the NPBS set-up.

The analysis of slope and peak to peak amplitude versus probe and pump intensities has been carried out for the F=2 and crossover features of polarisation spectra. Figure 4.16 shows the behaviour of the polarisation spectrum as a function of pump intensity with probe fixed at 1.9 ± 0.3 mW/cm^2. For small intensities, both the slope at the zero crossing and peak to peak amplitude increase linearly with increase

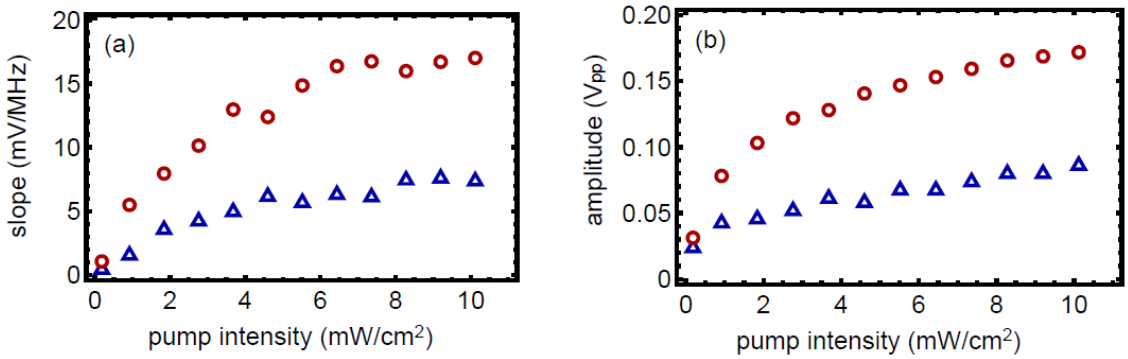

Figure 4.16: Dependence of the polarisation spectroscopy signal on the pump beam intensity for fixed probe beam intensity of 1.9±0.3 mW/cm^2. (a) Variation of slope at zero crossing for features A (red circles) and B (blue triangles). (b) Variation of peak to peak amplitude for A (red circles) and B (blue triangles) features.

in pump/probe intensity. For higher intensities, power broadening leads to an increase in linewidth Γ of the saturated absorption features. As a result, the PS signal amplitude saturates and the slope rolls over. The amplitude and slope of the $F = 2$ feature are almost double those of the crossover. This shows that the PS signal is dominated by the cycling transition. Here, we don't see any clear sign of amplitude saturation in the crossover feature.

Figure 4.17 shows the trends for varying probe intensity at fixed pump intensity of 5.6±1.0 mW/cm^2. The slope and amplitude follow similar trends as explained for varying pump intensities for both the features.

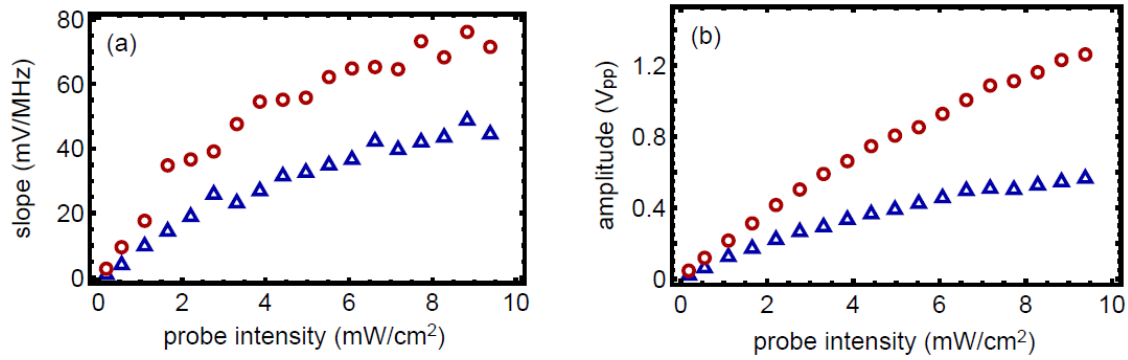

Figure 4.17: Dependence of the polarisation spectroscopy signal on the intensity of the probe beam for fixed pump beam intensity of 5.6±1.0 mW/cm^2. (a) Variation of slope at zero crossing for A (red circles)and B (blue triangles) features. (b) Variation of peak to peak amplitude for A (red circles)and B (blue triangles) features.

4.3.2 Magnetically-induced dichroism

Magnetically-induced dichroism (MD) exploits the Zeeman shift of m_F-dependent atomic sub-states by the application of a uniform longitudinal magnetic field. This splitting gives rise to a frequency dependent dichroism in the atomic medium. A linearly polarised probe beam is composed of $\sigma\pm$ components of circular polarisation. When it is passed through a dichroic medium, the two absorption profiles, corresponding to $\sigma\pm$ components of the probe, are frequency shifted in opposite directions. The amount of shift depends linearly on the applied magnetic field. If the Zeeman shift is of the order of absorption linewidth, the subtraction of transmitted $\sigma\pm$ signals gives a dispersion shaped signal. In the absence of a magnetic field the different m_F sub-states are degenerate, so the two transmitted signals are equal and the subtraction signal is zero. The idea of locking a laser using magnetic dichroism was first introduced by Corwin *et al.* for Doppler broadened absorption lines of rubidium [50]. A large magnetic field ($\sim$100G) is required for the Doppler broadened lines as their linewidth is of the order of few 100s of MHz. The resulting dispersion error signal has a huge capture range (of the order of Doppler linewidth) and generally the laser lock is very robust, but it suffers from undesirable frequency drifts (few MHz) due to magnetic field shifts. One can obtain a sub-Doppler magnetic dichroism signal with reduced fluctuations but relatively smaller capture range by introducing a counter-propagating linearly polarised pump beam. Moreover, a smaller magnetic field can generate this sub-Doppler spectrum as it requires a Zeeman shift of magnetic sub-states to be of the order of the natural linewidth (only a few MHz). Sub-Doppler magnetic dichroism was first reported by Shim *et al.* in 1999 [99]. In this work, sub-Doppler dispersive signals were obtained for ^{85}Rb using a small magnetic field of $\sim$3 G. Later in 2002 this technique was presented by Wasik *et al.* for D_1 lines of Na and Rb [105]. The following year, this method was demonstrated by Petelski *et al.* for ^{85}Rb and ^{87}Rb [73].

We attempted sub-Doppler magnetic dichroism for potassium but could not get a good error signal. The spectrum we obtained had small sub-Doppler dispersive features sitting on a large Doppler broadened background. The background was so dominant that the features were located much below the zero crossing. When we tried to obtain a flat background by tweaking the probe polarisation, the voltage offset of the error signal became very large. Therefore, these features were not found suitable for laser locking. This technique was subsequently presented for potassium by Pitchler *et al.* [76]. In their work, they obtained a MD spectrum on a relatively flat background with a nice dispersive feature at crossover. We believe that the large Doppler background of our signal was a result of the polarisation impurities caused by the wave-plates we used in our set-up. The design wavelength of these wave-plates is 780 nm (recall that our operating wavelength is 767 nm) and were chosen because of low cost and easy availability.

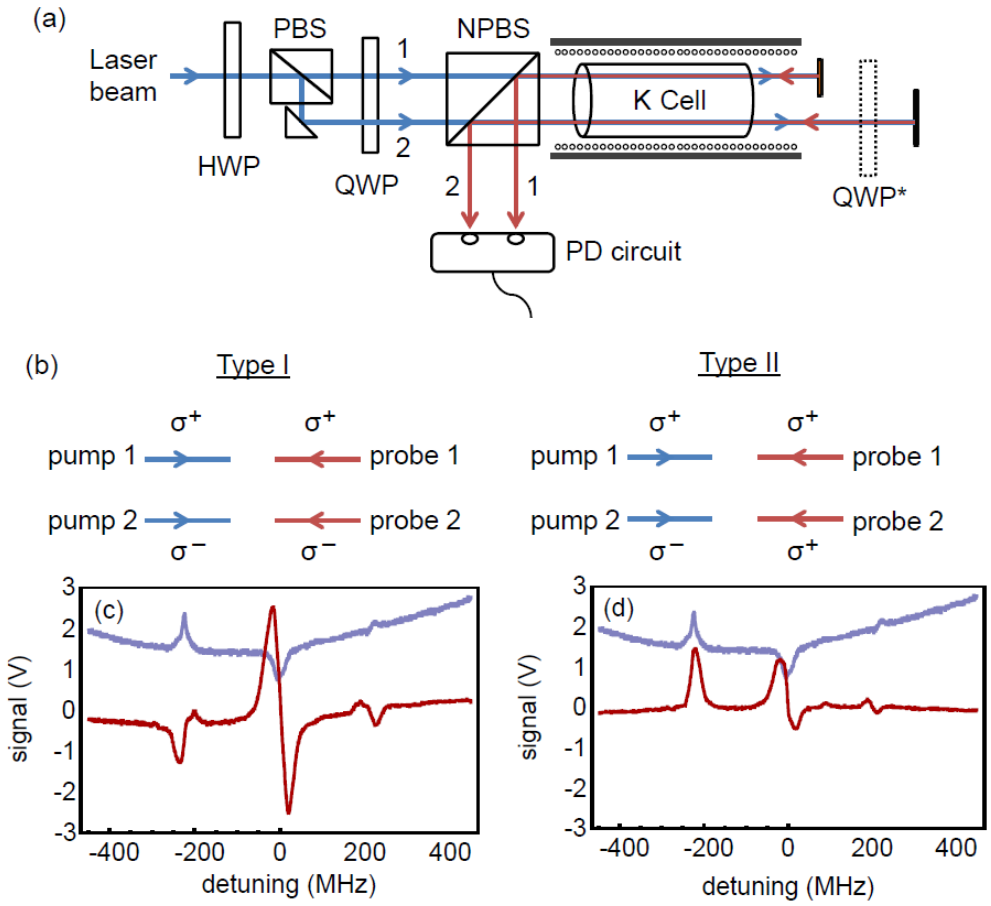

Figure 4.18: (a) Schematic for newly modified split-beam MD spectroscopy. For Type-1 spectroscopy, the QWP* is not included in the set-up whereas for type-2 spectroscopy it is introduced. (b) Representation of the polarisation states of pump and probe beams for Type-1 and Type-2 schemes. (c) Type-1 MD signal (red coloured) and saturated absorption spectroscopy signal (blue coloured). (d) Type-2 MD signal (red coloured). These signals are recorded for pump intensity of 7.3±1.5 mW/cm^2 in each pair and a magnetic field of 10.3 G.

In order to improve this sub-Doppler MD signal, we could either increase the anisotropy in the medium or reduce the Doppler background. Both could be achieved by using two pairs of spatially separated pump and probe beams. The idea of using pairs rather than single beams was taken from reference [98]. The simplified experimental set-up of this modified scheme is shown in figure 4.18(a). There are counter-propagating pairs of pump and probe beams passing through the cell. A solenoid wrapped around the cell produces a longitudinal magnetic field along the length of the cell. The magnitude of the magnetic field can be varied by varying the current through the solenoid. The subtraction photodiode circuit is used to detect the probe beam pair and generate a modified magnetic dichroism signal. We get two different type of signals depending on the polarisation configuration of the pump-probe pairs as shown in figure 4.18(b). When the dotted quarter wave

plate (QWP*) is not used in the set-up, we get a signal which we denote Type-1. Introducing the QWP* gives the Type-2 signal.

In conventional single-beam magnetic dichroism, both the pump and probe beams are linearly polarised. The pump generates a symmetrical atomic distribution among the various m_F levels of the ground state. The $\sigma_\pm$ components of the linearly polarised probe induce $\sigma_\pm$ transitions (here $\sigma_\pm$ refers to transition corresponding to $\Delta m_F = \pm 1$) giving rise to absorption signals. In our modified set-up, the presence of two $\sigma_\pm$ pump beams increases the dichroism in the medium by shifting the atomic population towards larger $|m_F|$ sub-states. In Type-1 configuration, each of the probe beams has the same circular polarisation as that of the corresponding pump beam. Therefore, an enhanced absorption takes place when probe beams undergo $\sigma_\pm$ transitions (see figure 4.19(a)). Although, there exists a background because of differential Doppler absorption. In Type-2, the Doppler background is diminished by using two probe beams of the same circular polarisation (let say σ_+). However, the dispersive features are asymmetric in this case because of the different Clebsch-Gordan coefficients (see figure 4.19) for the two σ_+ transitions involving different m_F ground states for the two probe beams (see figure 4.19(b)).

Example spectra for these two types of MD are shown in figure 4.18(c) and (d). It is clear that the Type-1 spectrum has almost symmetrical features on a small Doppler background and particularly, the crossover feature has very large amplitude due to the role of hyperfine optical pumping [89]. In contrast, the Type-2 spectrum has relatively small and asymmetric features on a flatter background. We therefore restrict our attention to the Type-1 crossover feature for the rest of this study.

Here, we describe a simple model to understand Type-1 MD spectroscopy. Consider two 2-level atomic systems, each of which corresponds to one of the completely overlapping pump-probe pairs. For a weak probe beam, the photodiode signal is proportional to $e^{-\alpha}$, where α is the absorption coefficient of the probe beam. Let's say the two probe beams have absorption coefficients α_+ and α_- and their values can be written as:

$$\begin{aligned} \alpha_+ &= \alpha_{\mathrm{D}+}(1 - L_+), \\ \alpha_- &= \alpha_{\mathrm{D}\text{-}}(1 - L_-), \end{aligned} \tag{4.16}$$

where $\alpha_{D\pm}$ are the Doppler-broadened absorption coefficients for two probes, and $L_\pm = A_\pm/(1 + (x \pm \delta)^2)$ are the Lorentzian functions. Here, $A_\pm$ are the amplitudes of the Lorentzian functions, $x = (\omega - \omega_0)$ is the laser frequency detuning from the atomic transition frequency ω_0 and δ refers to Zeeman frequency shift for a particular transition. Here x and ω are normalised to Γ (power broadened linewidth which is a function of pump and probe intensities). In the presence of external magnetic field, the centres of the two Lorentzians

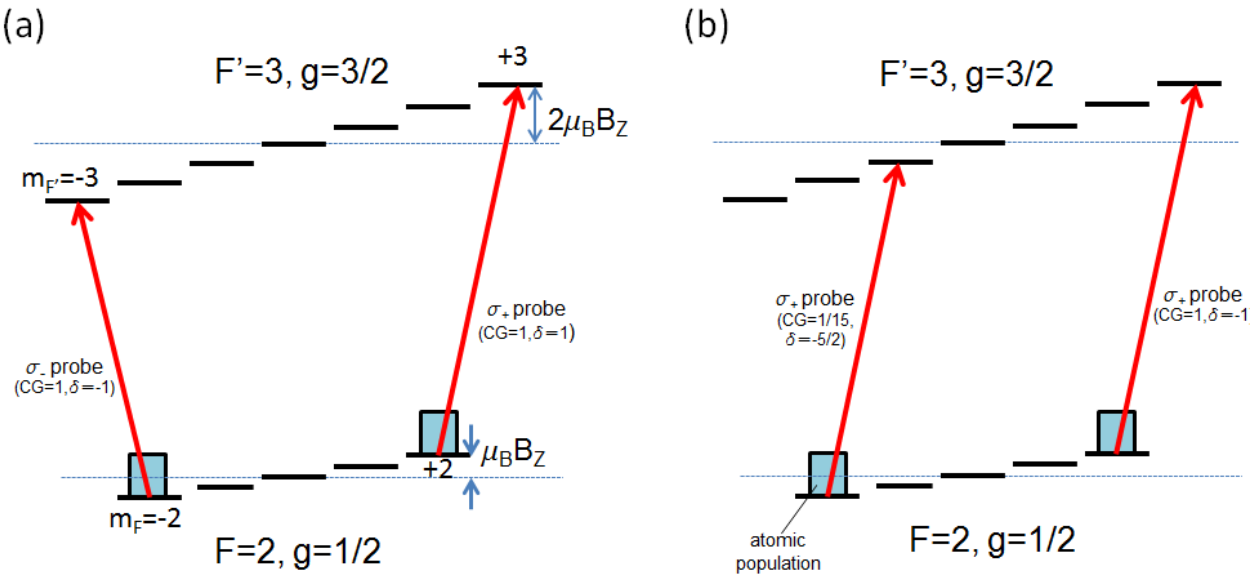

Figure 4.19: An illustration of the Zeeman splitting m_F sub-states and magnetically induced dichroism for the cyclic transition $F = 2 \rightarrow F' = 3$ of potassium-39. Here, δ refers to the Zeeman frequency shift (in the units of $\mu_B B_z$, where μ_B and B_z represent Bohr magneton and longitudinal magnetic field respectively) for a particular transition. Let's say σ_+ pump transfers the atomic population into the $m_F = +2$ state whereas σ_- pump transfers it into $m_F = -2$. (a) For the Type-1 configuration, each of the probes has same circular polarisation as its respective counter-propagating pump beam. So, σ_+ probe causes transition from $m_F = +2 \rightarrow m_{F'} = +3$ and σ_- probe causes $m_F = -2 \rightarrow m_{F'} = -3$ transition. (b) For type-2, both the probe beams are σ_+ therefore $m_F = +2 \rightarrow m_{F'} = +3$ and $m_F = -2 \rightarrow m_{F'} = -1$ transitions take place. These two transitions have different CG coefficients which explains the asymmetry of the Type-2 dispersion signal.

are Zeeman shifted in the opposite directions. The magnitude of this frequency shift δ depends linearly on the strength of the magnetic field. The difference signal is given by:

$$\Delta V = e^{-\alpha_+} - e^{-\alpha_-} \approx \alpha_- - \alpha_+, \tag{4.17}$$

where $\alpha << 1$. The amplitudes for the two Lorentzian features are equal because both the pump beams depopulate the ground states to the same extent and both the probe beams undergo transitions of equal strengths for a two level system. Hence, symmetry allows $A_+ = A_-$. Assuming that the Zeeman shift δ is of the order of Γ, the two Doppler profiles are almost the same and we can say that $\alpha_{D+} \approx \alpha_{D-}$. Therefore the final signal becomes

$$\Delta V = A \left[\frac{1}{1 + (x - \delta)^2} - \frac{1}{1 + (x + \delta)^2} \right]. \tag{4.18}$$

For small Zeeman shifts, the signal looks like the derivative of a Lorentizian signal. The equation 4.18 can be used to calculate the equations for the slope S of the signal at resonance and is given as:

$$S = \frac{4A\delta}{(1+\delta^2)^2}. \tag{4.19}$$

For small magnetic fields the signal slope increases linearly with increase in δ, becomes maximum for $\delta_0 = 3^{-1/2} \approx 0.6$, and then starts decreasing. The equations of signal amplitude and capture range can also be calculated but they become very complicated so they are not discussed here.

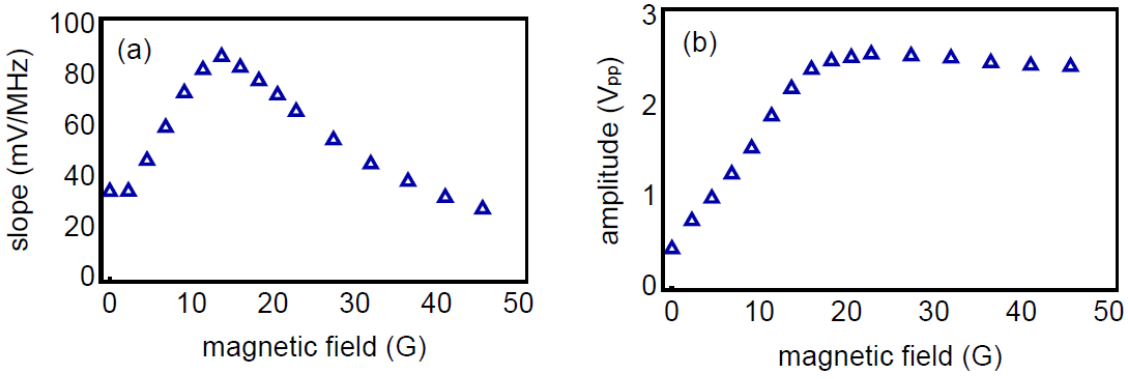

Figure 4.20: The variation of (a) the slope at the zero crossing and (b) the peak to peak amplitude of the Type-1 MD crossover feature with respect to the applied magnetic field. The fixed pump beam intensity in each pair is 2.7±0.5 mW/cm^2.

Figure 4.20 presents the magnetic field dependence for Type-1 crossover signal. There is a small signal even at zero applied magnetic field. This can be attributed to the presence of residual/stray magnetic fields and pump/probe polarisation impurities. As predicted from the two level model, the slope first increases for small magnetic fields and then rolls over. This is because after a certain magnetic field, the amplitude remains almost constant whereas the capture range still goes on increasing. It's important to mention that the signal in the decreasing slope wing is not useful for locking as its spectrum has a kink near the zero-crossing. The peak to peak amplitude follows the expected trend as well. It first increases linearly for small magnetic fields and then becomes constant when the Lorentzian peaks separate completely. This Type-1 crossover signal is mainly dominated by two transitions (see figure 4.21); $(F, |m_F|) = 1 \rightarrow (F', |m_{F'}|) = 2$ and $(F, |m_F|) = 2 \rightarrow (F', |m_{F'}|) = 3$ as they have the large transition strength in comparison to other possible transitions. The optimum magnetic field from these trends is around 14 G which gives a frequency shift of 35 MHz for the $F = 1 \rightarrow F' = 2$ transition and 19 MHz for the $F = 2 \rightarrow F' = 3$ transition. These frequency shifts are broader than natural linewidth γ because of composite nature of the A and B features. Moreover,

we are using large total pump intensity (5.4 mW/cm^2 for figure 4.20, which is about three times bigger than the saturation intensity), this causes power broadening of these features leading to the requirement of large frequency shifts (δ).

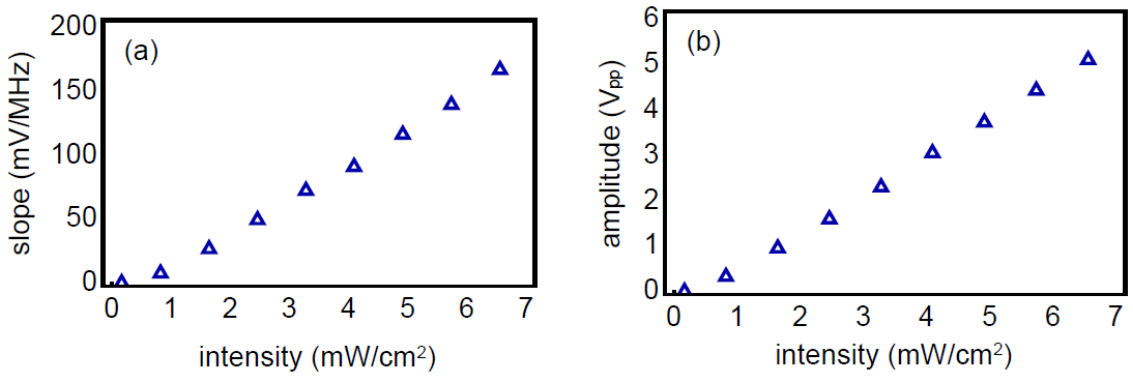

Figure 4.21: The variation of (a) slope and (b) amplitude of the Type-1 MD crossover feature with respect to total beam intensity in the both pairs. A fixed magnetic field of 10.3 G was used for these measurements.

Figure 4.21 shows the observed dependence of crossover slope and amplitude on beam intensity. In our set-up, we have used retro-reflected pump beams so separate measurement of pump/probe intensities is not feasible. Hence we record and optimise the total intensity in both pairs of beams. It is evident that both the slope and amplitude grow linearly all the way to the maximum beam intensity we have tried, limited by photodiode saturation. There is no sign of signal saturation in these trends even well above the saturation intensity I_{sat}. This suggests that there is little or no broadening of the absorption lines.

4.4 Comparison between different spectroscopy signals

Our main interest is to stabilise our master laser to either the A or B feature of potassium D_2 spectrum by using a suitable error signal and then to use this laser as a frequency reference for the rest of the MOT laser system. So here we make a comparison between the different spectroscopies investigated.

Among modulation based techniques, despite the similar set-ups, the DM and MT signals look very different from each other. The DM signal has two useful features at A and B. Although either of these two can be used to lock the laser, the feature A looks much more reliable in comparison to B, which is complicated by the kink. The shape of these features roughly look like derivatives of their corresponding saturated absorption features and are broad due to their composite nature. On the other hand, the MT signal has only one dominant feature near the $F = 2 \rightarrow F' = 3$ line of ^{39}K which is much bigger and steeper than DM features. Therefore, the MT signal is useful for locking the laser near the cycling transition. However it

has a very weak crossover signal, which is a disadvantage if one wants to lock near the crossover transition. The MT signal is generated by non-linear four wave mixing process which leads to a dispersive like feature on a very stable, flat background independent of changes in absorption caused by fluctuations in temperature or laser intensity. Also, the centre of the zero crossing exactly falls on the centre of the sub-Doppler resonance and its position is independent of changes in magnetic field or polarisation fluctuations. In contrast, the DM signal sits on a Doppler broadened background.

In modulation-free methods, the PS provides a large $F = 2$ signal for laser locking as it is dominated by the effect of the cycling transition. On the other hand, the MD prefers the crossover feature due to strong absorptive lines which are a result of hyperfine optical pumping. This difference between PS and MD has already been observed for Rb [39]. Both of these methods will be sensitive to temperature dependent fluctuations in polarisation and drifts in ambient magnetic fields. The PS method requires zero or very small magnetic field (∼20 mG in our set-up) whereas MD uses much larger fields (we use an optimised field of 14 G) and hence will be less sensitive to the ambient fields.

Table 4.2: Comparison between various potassium spectroscopies along with the values of important parameters for laser stabilisation.

Spectroscopy	Pump/probe intensity mW/cm^2	Slope V/MHz	Amplitude V_{PP}	Capture Range MHz	Noise mV_{rms}	Bandwidth kHz
DM ($F = 2$)	4.5/1.4	100	0.4	15	15	200
MT ($F = 2$)	4.2/1	600	3	5	15	200
PS ($F = 2$)	5.6/8	80	1.2	56	7	750
MD (crossover)	6.7 (total)	170	5.1	36	20	750

For locking a laser, a very important parameter is the slope of the error signal near the zero voltage crossing. This parameter sets one of the gain terms in the locking chain without limiting the bandwidth. In contrary, the servo has a limited gain-bandwidth product (this is an intrinsic property of the electronic components), increasing the servo gain limits its bandwidth. Therefore we aim for an error signal with large slope which will enable us to have higher overall gain. The other important figure of merits include peak to peak signal amplitude, capture range, signal noise and bandwidth. Table 4.4 shows the values of various parameters and gives a comparison between different methods. The MT signal has the largest slope out of all, at the expense of a reduced capture range of 5 MHz. Therefore, this method could be advantageous for experiments requiring very tight locks. However, the lock would not be very robust to perturbations. A large capture range provides more stability against frequency fluctuations. The MD signal has the maximum amplitude which is almost 4 times larger than PS and MT signals, and 13 times larger than the DM signal. Although, its capture range is slightly smaller than the PS signal. For all of the methods, the signal noise is

below 20 mV_{rms} (root mean square voltage) with PS having the minimum value of 7 mV_{rms}. The selection of a spectroscopy method for laser stabilisation depends on the particular requirements of any given experiment. We chose MD method to stablise our master laser using a home built PID feedback circuit (designed by J Goldwin). We have been using this method in our experiment for more than two years and have found it very stable and robust, as our laser system remains locked for many days without any readjustments or relocking.

CHAPTER 5

LASER SYSTEM

A stabilised laser system is a key ingredient to obtain a MOT in an experiment. This chapter focuses on the set-up of our MOT laser system and its stabilisation in detail. In addition to the MOT laser system, we want to have a second independent laser system for locking and probing of our ring cavity. The cavity locking and probing laser system is still under construction and more details on it can be found in the thesis [62] of another student on the same experiment.

The structure of this chapter is as follows. Section 5.1 describes the set-up and stabilisation chain of the MOT laser system. This system consists of master, cooling and repump lasers. Section 5.2 explains the frequency offset locking of the repump and cooling laser. Finally, section 5.3 describes the design, assembly and characterisation of the tapered amplifier system which is required to amplify the power of our cooling and repump lasers.

5.1 MOT laser system

For laser cooling and trapping of neutral atoms in a MOT, we require three orthogonal pairs of laser beams and a suitable magnetic field gradient. Each pair consists of two counter-propagating beams with opposite circular polarisation. We require our MOT light to consist of two different frequencies, one near the cooling transition ($F = 2 \rightarrow F' = 3$) and the other near the repump transition ($F = 1 \rightarrow F' = 2$) of the ^{39}K D_2 spectrum. The repump light is required to maintain the atomic population in the cooling transition cycle by pumping atoms from $F = 1$ to $F = 2$ state. The cooling and repump lasers need to be stabilised slightly red detuned from their respective transitions. The red-detuning of a few MHz is required for the proper functioning of the MOT as explained in chapter 2. Another 'Master' laser is used in our set-up which provides the frequency reference for the whole stabilisation chain.

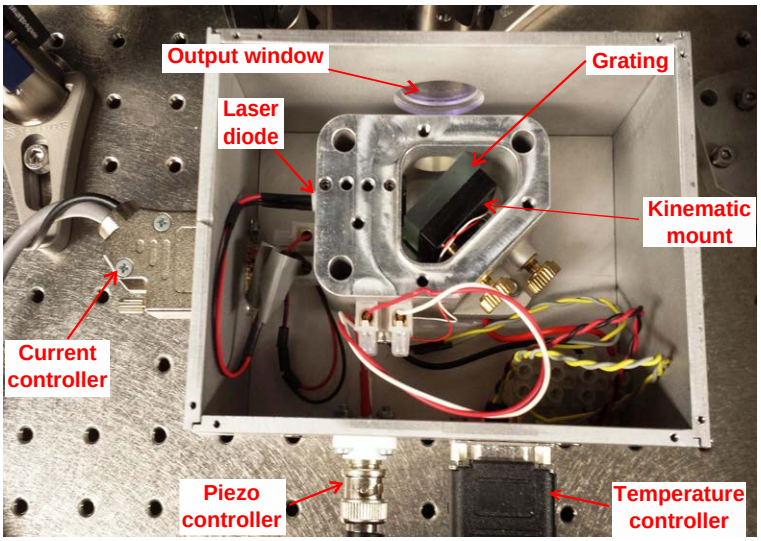

Figure 5.1: A photograph of the master laser showing various internal components.

Frequency tunable diode lasers are a standard piece of equipment in a typical cold atoms experiment [110]. Our laser system consists of master, cooling and repump lasers. All three of these are home built, extended cavity diode lasers (ECDL) in Littrow configuration. These are operating near 766.7 nm wavelength which is the D_2 transition frequency of ^{39}K. These lasers should be highly stable, narrow linewidth and frequency tunable in order to achieve atom cooling down to the order of micro-Kelvin temperatures. Our laser design is similar to that described in reference [70]. We use a GaAs semiconductor diode with an anti-reflection coating and a central wavelength of 770 nm (Eagleyard, EYP-RWE-0790-04000-0750-SOT01-00001). The diode is held inside a lens tube with a collimating lens (Thorlabs: C240TME-B) placed in front of it. A diffraction grating is used to extend the cavity which is mounted on a kinametic mirror mount (Radient Dyes, MNI-H-2). There are two knobs on the mirror mount for fine-adjustments of the horizontal and vertical tilts of the grating. The horizontal knob changes the frequency supported by the laser cavity. A piezoelectric transducer (Thorlabs, AE0203D04F) is pressed between the horizontal knob and back surface of the mirror mount, this allows us to move the grating by applying a voltage across the piezo and hence scan the laser frequency. The adjustment of vertical position of the grating changes the first order feedback to the laser diode. It is set to achieve a low value of the threshold diode current. The laser cavity is enclosed inside an aluminium housing which sits on a flat peltier cooler (RS Components, 490-1525) and a small thermistor (Thorlabs, TH10K) is used to measure the temperature of this cavity housing. The temperature of the system is maintained at 291 K with a stability of 0.7 mK. The peltier and thermistor are connected to a temperature control unit which stabilises the temperature of the system. A diode controller is used control the current fed to the laser diode.

This typically runs at ∼70 mA which gives ≈18-20 mW of laser output power. For the master laser, we use the Thorlabs diode (LDC202C) and temperature control modules (TED200C). For our cooling and repump lasers, we use the Wavelength Electronics diode (MPL250) and temperature control modules (PTC2.5K-CH, stability of 2 mK). The typical linewidth of our master laser is below 1 MHz which is estimated by our home-built fibre ring cavity. The beam coming out of the laser is elliptical and an anamorphic prism pair (Thorlabs, PS877-B) is used to make it circular. The circular beam is then passed through a Faraday isolator (Laser 2000, I80T-4L) to avoid unwanted feedback to the laser.

Figure 5.8 shows a simplified schematic of our MOT laser system. The process of laser stabilisation involves generating a suitable error signal and then sending it to the locking servo system. The locking servo controls the current through the laser diode and voltage across the piezo transducer. This locks the laser to the frequency corresponding to the zero voltage of the error signal. The master laser is locked at the crossover (or B) feature of the Type-1 MD spectroscopy as discussed in chapter 4. The lower limit of frequency fluctuations for the master laser is ∼120 kHz. This is calculated using the error signal slope (170 mV/MHz) and root mean squared (rms) noise level (∼20 mV_{rms}) measured far away from the lock point. This limit is a measure of the minimum frequency fluctuations achievable with the servo. The inloop measurement (while laser is locked) of the rms noise (∼50 mV_{rms}) near the lock point gives frequency fluctuations of ∼300 kHz. The stabilised master laser is then used to lock the repump laser at repump transition frequency. Following this, the cooling laser is locked at cooling transition frequency with respect to the repump laser. The locking error signals for the cooling and repump lasers are generated by frequency offset locking scheme which is described in details in the following section.

5.2 Frequency offset lock

The frequency offset locking (FOL) scheme used to lock the repump laser with respect to the master laser (already stabilised) is demonstrated by the schematic as shown in figure 5.2 [81]. First of all a beat note is generated between the master and repump laser beams by coupling them both into a single mode fibre. The beat note frequency is given by $\omega_B = \omega_1 - \omega_2$, where ω_1 and ω_2 are the frequencies of the master and repump lasers respectively. The beat note is detected on a fast photodiode (Hamamatsu Photonics, G4176-03). The photodiode requires a power supply of +7 V and ground which is fed to it through the DC port of a Bias Tee (Minicircuits, ZFBT-4R2GW-FT+). A home made voltage regulator circuit is used to convert the standard +12 V output of a commercial power supply into regulated +7 V. The RF output of the Bias Tee is then fed to an amplifier (Minicircuit, ZFL-500LN+) of 20 dB gain. The amplified output is split into two parts

using a coupler (Minicircuits, Z30-13-5-75+). The weaker part of the splitter output is used to detect the beat note on a spectrum analyser and the stronger output is fed to a mixer (Minicircuits, ZFM-2+) where it mixes with a reference signal generated by a voltage controlled oscillator (VCO). The reference signal is of frequency $\omega_r \approx 370$ MHz. This frequency is chosen to generate an error signal whose lock point is ≈ 206 MHz blue detuned with respect to the master laser lock. One can change this frequency offset by changing the reference signal frequency ω_r. The output of the mixer is filtered through a low pass filter (LPF, Minicircuits,

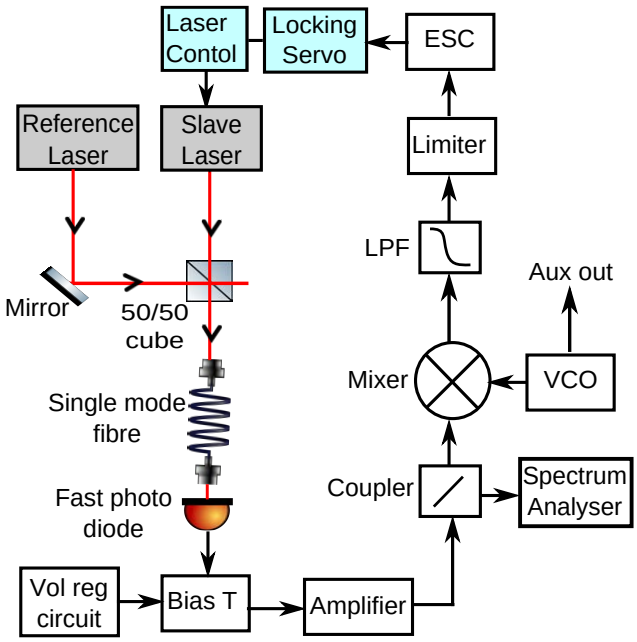

Figure 5.2: The schematic of the frequency offset lock system. The reference laser is the one which is already stabilised and the slave laser is the one to be stabilised. LPF = low pass filter, VCO = voltage controlled oscillator, ESC = error signal circuit.

ZX75LP-158-S+) to filter out the higher frequency component ($\omega_B + \omega_r$) from the signal and lets the low frequency component ($\omega_B - \omega_r$) pass through it. After this, a limiter (Minicircuits, VLM-33-S+) is used which attenuates the signal power if it gets larger than its saturation limit of 11.4 dBm. Since the incoming signal amplitude is high enough to saturate the limiter, this gives us a constant beat signal of amplitude 11.4 dBm which is independent of the power fluctuations in the original beat signal detected at the photodiode. This ensures that there are no frequency drifts in the final error signal due to the power fluctuations in the original beat note. The output of the limiter is fed to an error signal circuit (ESC) which is used to generate an error signal by exploiting the frequency dependent attenuation response of a high pass filter (HPF). The resulting error signal has a lock point near the frequency corresponding to the 3dB point of the HPF. This circuit design is from reference [81]. The schematic of the ESC is shown in figure 5.3(a) and its function

to generate an error signal is explained as below. An input signal of frequency $\omega_{in} = (\omega_B - \omega_r)$ enters the

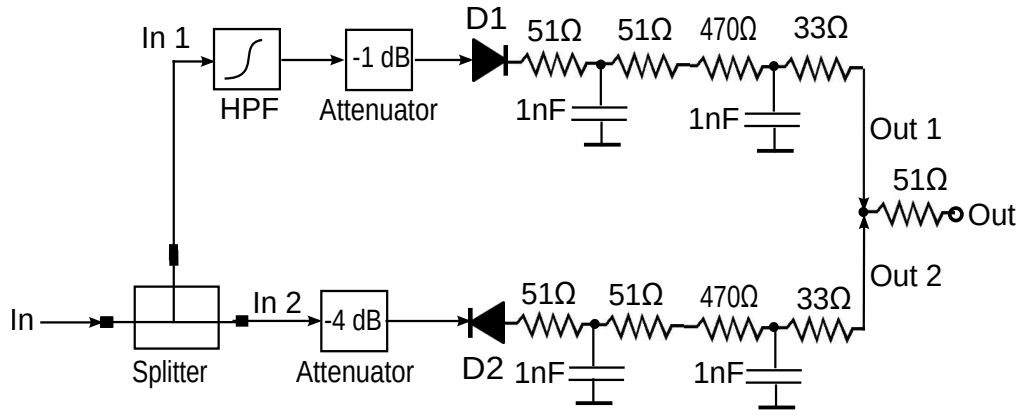

Figure 5.3: Schematic of the error signal circuit (ESC). HPF = high pass filter.

ESC and splits into two equal parts using a 50:50 splitter (Minicircuits, MSC-2-5+). The first half of the signal which is labelled as 'In 1' goes to a HPF. The HPF (Minicircuit, PHP-200+) has a 3 dB attenuation at ω_{3dB}=164 MHz. The 'In 1' signal undergoes a frequency dependant attenuation when passing through the HPF. Further, the use of a -1 dB attenuator (Minicircuit, LAT-1+) reduces the signal amplitude by one dB at all frequencies. After this a rectifying circuit consisting of a Schottky diode and RC filters is used to rectify the signal. The DC output signal which is labelled as 'out 1' of this branch has a frequency dependant amplitude. The second half of the input signal 'In 2' is fed to two attenuators (Minicircuit, LAT-3+ and LAT-1+) in series which provides a total of -4 dB of amplitude attenuation at all frequencies. This then passes through a rectifying circuit similar to the one used in the first branch but having opposite polarity. This produces a positive DC output signal 'Out2'. Combining these two outputs gives an error signal. When $\omega_{in} > \omega_{3dB}$, the error signal has a positive voltage amplitude whereas for $\omega_{in} < \omega_{3dB}$ it has a negative voltage amplitude. For $\omega_{in} = \omega_{3dB}$, the two outputs exactly balance which gives the zero crossing of the error signal. The frequency corresponding to the zero volts of the error signal depends on the reference frequency ω_r fed to the mixer and 3 dB frequency $\omega_{3\text{dB}}$ (fixed for a particular choice of filter) of the HPF. Hence, one can easily shift the lock point by changing ω_r from the VCO. Figure 5.4 contains the error signal for repump laser locking. The lock point is $\approx$ 206 MHz blue detuned to the master laser lock point. This error signal is used to stabilise the repump laser via the servo control loop.

Further, the cooling laser can be stabilised using the same scheme as explained above. In this case, a beat signal is generated between the repump and cooling laser beams. A reference signal of frequency $\omega_r \sim$ 286 MHz is mixed down with the beat signal, which then passes through the ESC circuit. The final error

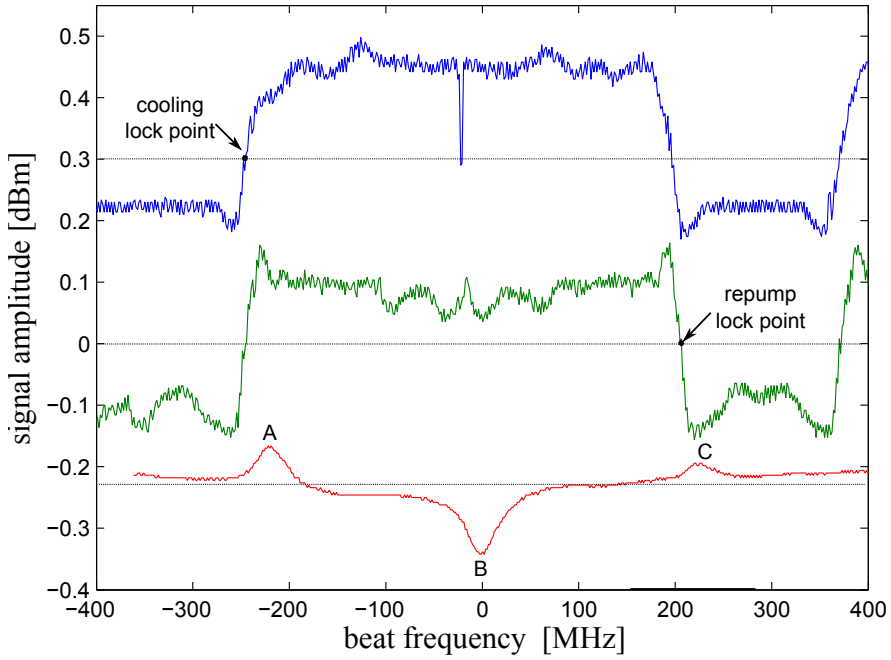

Figure 5.4: The error signals for cooling (blue trace) and repump (green trace) lasers generated by using frequency offset locking scheme. The saturation absorption spectroscopy (red trace) is shown for the reference. The blue and red signals are shifted up and down respectively for the sake of clarity. The cooling and repump laser lock points are a few MHz red detuned to the A and C features respectively. These traces are recorded separately and presented together in a single graph to provide a good visualisation of different lock points.

signal has a lock point at $\approx$ 450 MHz red detuned to the repump laser lock point, which is around the cooling transition frequency. Figure 5.4 shows the FOL error signals used to stabilise the repump and cooling lasers. A background subtracted saturated absorption signal is used as reference. The lock point of these error signals can easily be shifted by changing their respective VCO reference frequency.

The frequency offset locking of both the repump and cooling lasers is very robust and stable against drifts. Generally, the lasers remain locked for the entire day without any need of relocking. The beat note between master and repump lasers has a Gaussian FWHM of 1.02 MHz at 0.04 sec. For the repump and cooling lasers this linewidth is 1.01 MHz at 0.04 sec.

5.3 Master oscillator power amplifier system

The MOT beams require a high optical power of around 10-15 mW in each of the six beams. As MOT beams are retro-reflected so $\sim$ 60 mW of maximum power is required to make a MOT. Our home build ECDL lasers can generate a limited power of $\sim$ 18-20 mW which is not sufficient to achieve a MOT. In this section, I describe the design, construction and characterisation of our home built Master Oscillator Power Amplifier

(MOPA) system which amplifies the cooling and repump laser powers without altering their linewidth and stabilisation. The amplified output is used to generate the MOT beams. For the understanding of the MOPA working and assembly, see references [32, 49, 75]. This MOPA system has a GaAs chip (M2K Laser, M2K-

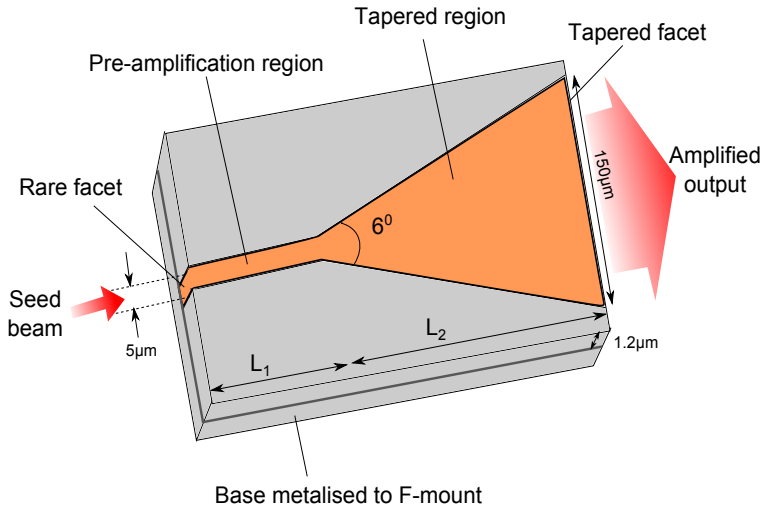

Figure 5.5: A simplified schematic of the Tapered Amplifier chip. Here L_1 and L_2 are lengths of the pre-amplification and tapered regions respectively. The tapered angle θ=6^0 is designed to fill the entire tapered region with optical power coming from the pre-amplification region.

TA-0765-1000, DHP-F packaging). A simplified schematic of the Tapered Amplifier (TA) chip is illustrated in figure 5.5. The chip consists of: the rear facet, pre-amplification region, tapered region and taper facet. For the normal single pass operation of the MOPA, a seed laser beam (in our case it is a combination of cooling and repump laser beams) is focused on the rear facet from where it enters the pre-amplification region. The size of the rear facet in the transverse direction is very small 5×1.2 μm, this allows the spatial filtering and amplification of only the TEM_{00} component of the seed laser beam. After pre-amplification, the light enters the tapered region where it gets highly amplified and finally comes out from the taper facet. The taper facet is larger in size (150×1.2 μm) to avoid any damage to the chip in case of high amplification in the gain medium. The TA cavity length is $L=L_1+L_2 \approx 2.5$ mm and L_1 and L_2 are the lengths of the pre-amplification and tapered regions respectively. The chip comes installed at the centre of a metal F-mount which acts as the heat sink. The TA chip has a very large tunable spectrum range (765-790 nm) which is narrowed down by using a stablised seed laser. The amplified output retains the linewidth and stabilisation of the seed. The chip has an anti-reflection coating (<0.1%) on both the rear and taper facets to avoid laser action by the TA chip itself. An external current source is used to provide the electrical pumping of the gain medium. The chip consists of closely spaced gold wires to make a uniformly distributed electrical contact from the cathode

connector to its top surface. The base of the chip is in direct contact with the F-mount which acts as an anode.

5.3.1 MOPA design and assembly

Our MOPA system consists of the TA chip, input and output lenses, and current and temperature control elements. All this is enclosed in a custom designed metallic housing as shown in figure 5.6 with lid removed. The TA chip is very fragile and sensitive to sudden changes in the injection current, temperature and mechanical shocks. Also, the output power can fluctuate greatly for tiny changes in injection current, seed power and temperature. We use a current controller unit (Thorlabs, LDC 240C) which provides a constant current with 0.1% accuracy. Under normal working conditions, a TA chip is operated at >1A current and it generates a large optical power (∼1 W). This generates a lot of thermal energy and it needs to be cooled down otherwise it will be damaged within a minute. So, a peltier cooler (RS Components, 490-1317) is placed underneath the TA chip body with a copper plate sandwiched between the two. The copper plate is used to increase the heat conduction from the chip mount to the peltier cooler. A thermistor (Thorlabs, TH010K) is installed in the chip frame to record its temperature. Both the peltier and thermistor are connected to temperature control unit (Thorlabs, TEDE 200C). Using this TA chip, a 30 mW of seed power and 2.7 A of current can produce a maximum of 1 W of output power. However, to increase the life of the chip we use much lower operating current and seed power.

In the MOPA set-up, it is important to precisely couple the seed beam into the chip to get a maximum output power. As the rear facet is only 5×1.2 μm in size we need to use a suitable lens l_1 (aspherical, C240TME-B, f=4.51 mm) to focus the seed beam on this facet. The tapered facet has rectangular area of size 150×1.2μm and the outcoming beam from this facet is divergent and elliptical in shape. As shown in figure 5.6(b),(c) the divergance of the amplified beam coming out of the tapered facet in the xz and yz planes are different. In the xz plane (top view of the MOPA), the output beam appears to be originating from a virtual source present inside the chip at a distance L_2/n_l from the tapered facet. The angle of divergence in this plane is $\theta \times n_l$, where $\theta = 6^\circ$ is the tapered angle which is designed to fill the whole tapered region with optical power coming out of the pre-amplification region. Here n_l is the lateral refractive index of the medium. The divergence angle in the yz plane (side view of the MOPA) is $\approx 45^\circ$. Therefore the output beam is astigmatic as its divergence is very high along the y-axis in comparison to the x-axis. Therefore, we need to use two lenses; an aspherical lens l_2 (Thorlabs, C230TME-B, f=8.0 mm) and a cylindrical lens l_3 (f=-50 mm) for collimation at the output end. The lens l_2 collimates the beam along x-direction whereas

it converges it along y-axis. The cylindrical lens l_3 collimates the beam along y-axis. The lenses l_1 and l_2 are mounted in three dimensional translational stages (Newfocus, LP-1A-XYZ) for their positioning with few μm precision. The cylindrical lens is directly glued on a mount which can slide on cage system attached to the wall of the MOPA housing.

5.3.2 Optical set-up and characterisation

The right hand side portion of the figure 5.8 shows the optical set-up to generate MOT beams. As input of the TA chip, we use a seed beam which consists of almost equal power contribution from each of the cooling and repump lasers. The amount of power amplification depends on the input seed power, seed coupling efficiency and injection current. The amplified and collimated beam coming out of the MOPA set-up is elliptical in shape ($\omega_y : \omega_x \approx$4:1, where $\omega_{x,y}$ represents the output beam size along x- and y-axis respectively). To make it circular, we use a telescope which consist of two cylindrical lenses of focal length 100 mm and 25 mm (along y-axis), placed 12.5 cm apart. The chip is very sensitive to back-reflection of light into it. This can lead to permanently damage the chip so we use a Faraday isolator (Thorlabs, IO-5-780-HP, isolation 38-44 dB, transmission 90%). During the operation of the MOPA, we detected the back reflection from the rear facet of the chip into the lasers which was affecting their performance. To avoid this, we use a Faraday isolator on the input side (Thorlabs, IO-3D-780-VLP). The amplified ouput beam is divided into three equal parts and then coupled into three single mode, polarisation maintaining fibers. The outputs of these fibres are then used as three of the MOT beams each retroreflected to form all six MOT beams. The full desctription of the MOT beams has already been desribed in section 2.2.3. A tiny part of the amplified output is sent to our home built transfer cavity. This is used to observe the contribution of the cooling and repump powers in the MOT beams. The cooling to repump power ratio in the seed beam is adjusted to achieve 1:1 power ratio at the output.

The amount of amplification achieved from a MOPA set-up depends mainly on the seed power, seed coupling and injection current. Using high injection current with lower seed power and poor coupling reduces the life of the TA chip. Figure 5.7(a) shows the variation of the output power with seed power at a constant injection current of 1.5 A. There is a linear increase in output power at low seed powers (< 8 mW) and then it starts saturating after that. For these measurements, we could only go up to a maximum of 11 mW of the seed power. This is because of limited power available from the ECDLs. Figure 5.7(b) shows the variation of the output power with the injection current at a constant seed power of 11 mW. Currently, we are operating

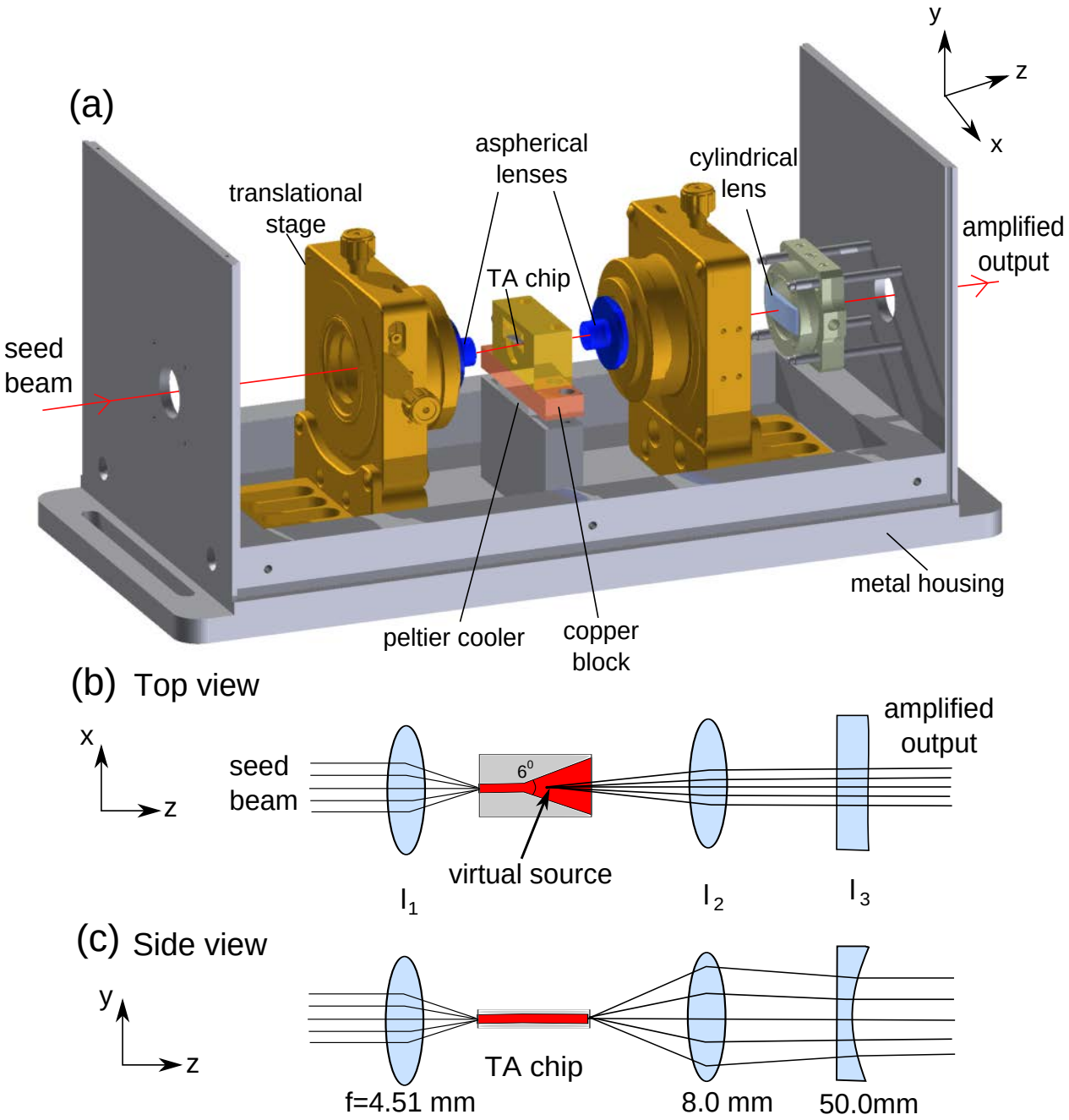

Figure 5.6: (a) Inventor design of the MOPA system. The aspherical lenses are actually placed very close to the TA chip but here they are shown away from it for the sake of clarity. The front, back and top walls are not shown to give a better view of the internal components. (b) The top view of the MOPA set-up showing the virtual origin of the output beam in xz plane. The lens l_1 focuses the seed onto the rear facet of the chip and lens l_2 collimates the amplified output beam in this plane. (c) The side view of the MOPA set-up showing the large divergence in yz plane. The cylindrical lens l_3 collimates the beam in the horizontal plane. The MOPA output beam shape is elliptical with aspect ratio of 4:1 and fast (long) axis along y-direction.

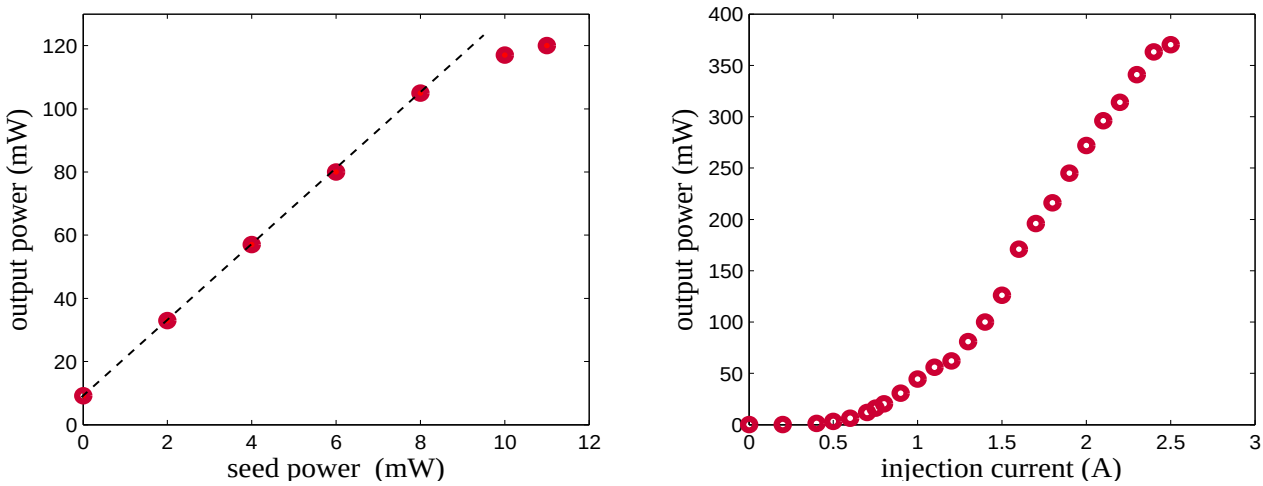

Figure 5.7: The characterization of MOPA system showing (a) variation of the output power with seed power at constant injection current of 1.5 A. Here error bars on the data points are very small and are estimated from the precision of the power meter (Thorlabs PM100D, 0.5% accuracy) used for these measurements. The linear fitting to the data set shows a saturation in the output power after 8 mW of the input power. (b) variation of the output power with injection current at constant seed power of 11 mW. Here seed has 1:1 power contribution from the cooling and repump lasers.

our MOPA at 11 mW of seed power and 2.0 A of injection current. This gives us ∼300 mW of output power which is reduced to half after coupling into polarisation maintaining, single mode fibres but still it is more than enough for the MOT beams.

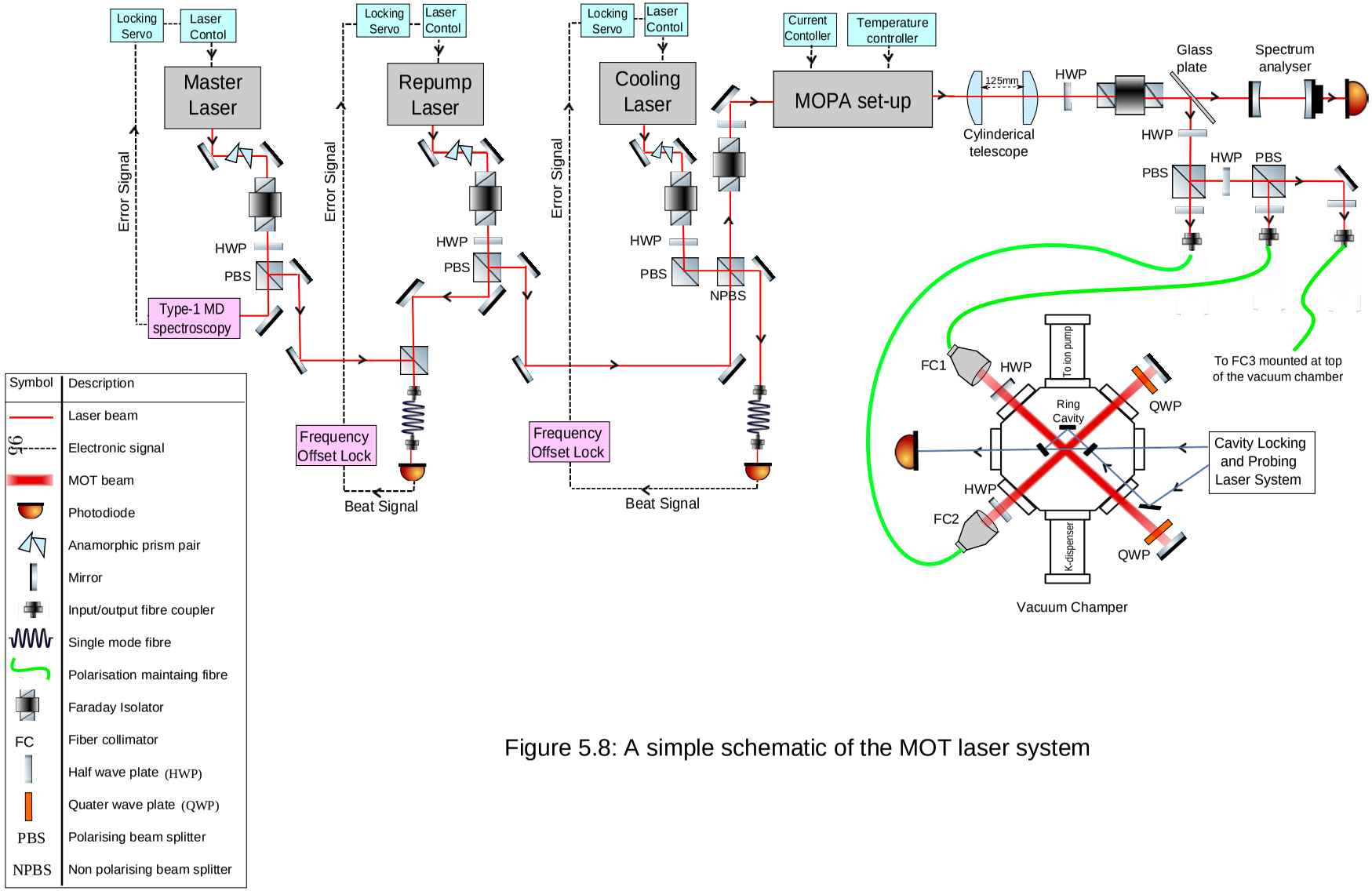

Figure 5.8: A simple schematic of the MOT laser system

CHAPTER 6

MOT FLUORESCENCE AND IMAGING SYSTEM

There are two popular imaging techniques to analyse and characterize a MOT. One of these two is fluorescence imaging and another is absorption imaging. In fluorescence imaging, light scattered by the cold atomic cloud is collected by a sensitive digital camera/photodiode, whereas in absorption imaging technique, atomic cloud is probed with a weak resonant beam and outgoing beam is collected by a sensitive detector. The outgoing beam has a weakened intensity due to absorption of photons by atoms. In this chapter, I discuss fluorescence imaging technique to measure size, shape and number of atoms of our ^{39}K MOT. Also, the MOT optimisation for magnetic field gradient and MOT beams detuning will be discussed in detail.

When an atom is subjected under a nearly resonant light, the photons are absorbed and then emitted spontaneously in random directions. The power of light emitted by the MOT is proportional to the total excited state fraction (given by $\gamma_{\rm sc}$) of atoms present inside the MOT and can be calculated with the following equation.

$$P_{\rm mot} = \gamma_{\rm sc} N_{\rm mot} E, \tag{6.1}$$

where $\gamma_{\rm sc}$ is the scattering rate per atom, $N_{\rm mot}$ is the total number of atoms in the MOT and $E = hc/\lambda$ is the energy of each photon which is 2.6×10^{-19}W/s at λ=766.66 nm.

The light scattered by the cloud of atoms in the MOT is collected by a CCD camera (Allied vision technologies Pike F-145) and the camera images are used to extract MOT parameters. Figure 6.1 shows the CCD image of the ^{39}K MOT captured by our CCD camera. The spatial dimensions of this picture are 3×5 cm, which are determined by calibrating the dimensions of a single pixel with respect to the diameter of the cavity mirror i.e. 6 mm.

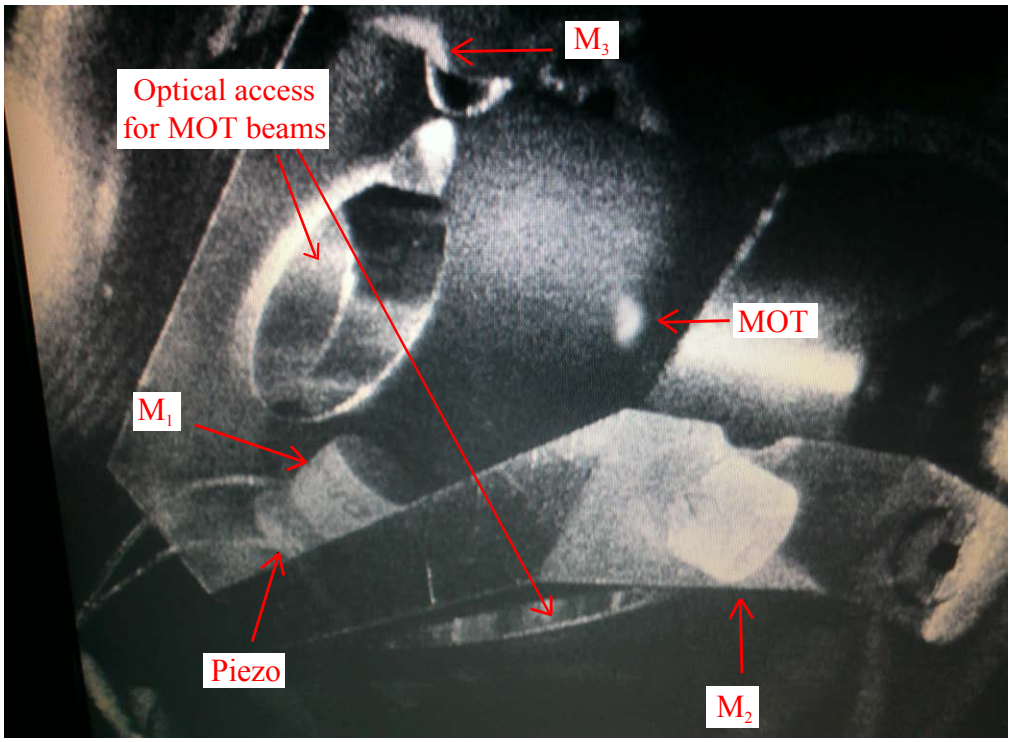

Figure 6.1: CCD camera image of the MOT loaded inside the ring cavity. M_1, M_2 and M_3 shown in the picture are cavity mirrors. The wires seen behind M_1 are connected to the pizeo which is glued at the back of it.

6.1 Imaging Hardware

The imaging hardware as shown in figure 6.2 is used to image the MOT onto the camera. We use a single bi-convex lens of focal length $f = 75$ mm in between camera chip and MOT. A mirror has been used to reflect the fluorescence light coming from the MOT onto the chip because of space issues underneath the vacuum chamber. The positioning of camera and lens with respect to MOT is determined by thin lens formula:

$$\frac{1}{f} = \frac{1}{u} + \frac{1}{v}, \tag{6.2}$$

where $u = 22 \pm 2$ mm and $v = 11 \pm 2$ cm are separations between lens and the MOT, and lens and camera respectively. We have chosen f, u and v in such a way that we get a suitable demagnification and solid angle for MOT imaging.

Firstly, the spatial size of our MOT is enormous as compared to usual MOT sizes, and secondly, the time of flight imaging (not included in this thesis) requires the expansion of the atomic cloud, therefore the demagnification of the MOT onto the CCD camera is required. In theory, we should get a demagnification

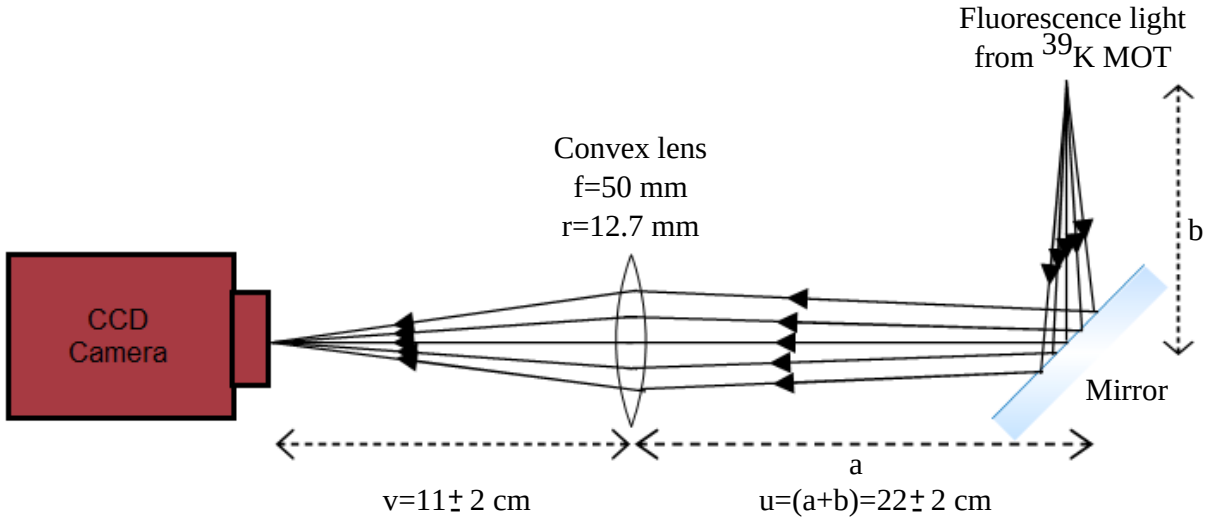

Figure 6.2: Geometry of imaging hardware system.

$d = u/v = 2 \pm 0.5$, here errors are estimated from the uncertainties in measuring u and v. In practice the magnification is ≈ 1.60 which is measured by calibrating the scale of actual CCD images using known size of the cavity mirror.

The atomic cloud is fluorescing uniformly in all the directions and only a fraction of this light in solid angle $d\Omega$ enters the camera chip. The radius r of the convex lens limits the solid angle. For small values of r, the fractional solid angle is determined by the following equation:

$$d\Omega = \frac{\pi r^2}{4\pi u^2} = (8 \pm 1.5) \times 10^{-4}. \tag{6.3}$$

6.2 MOT Analysis

6.2.1 Size and shape of MOT

The camera is positioned in such a way that it records the information in a plane containing the elongated axis (let's say z-axis) of the MOT. The CCD images are recorded with and without MOT and are then subtracted in order to get rid of the background light. This subtracted image is then fitted to a tilted two dimensional elliptical Gaussian function, assuming that the atomic distribution in a MOT is in accordance with the Gaussian distribution in all the three dimensions. The fitting results give the root-mean-squared widths σ's of the MOT along y- and z- axis. There is a symmetry along x- and y- axes, hence we assume

that the MOT size is almost same along these two directions.

$$\sigma_x = 0.31 \pm 0.03 \text{ mm}, \tag{6.4}$$

$$\sigma_y = 0.31 \pm 0.03 \text{ mm}, \tag{6.5}$$

$$\sigma_z = 0.52 \pm 0.04 \text{ mm}, \tag{6.6}$$

where errors in MOT dimesions are estimated from the Gaussian fits as shown in figure 6.3.

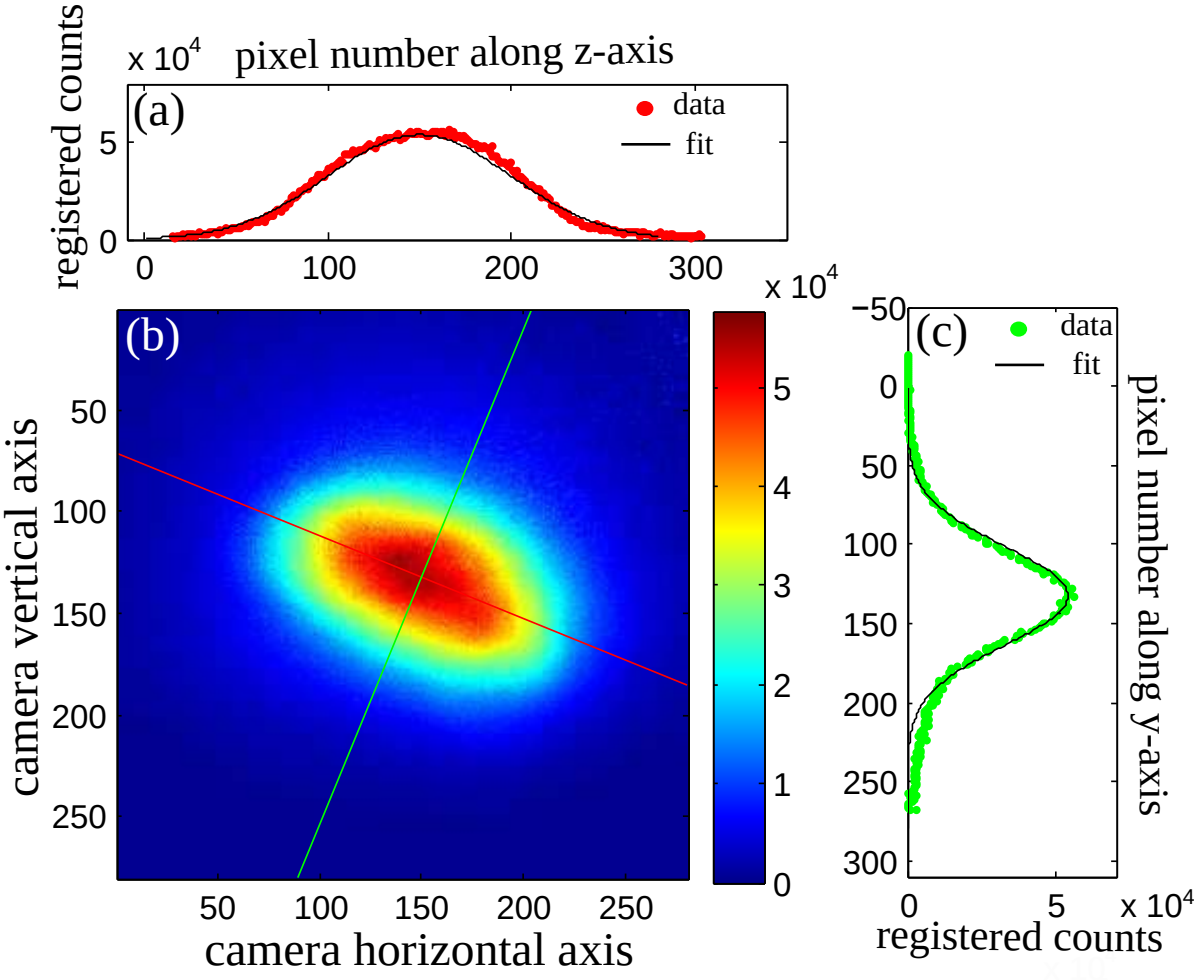

Figure 6.3: The results obtained by fitting the MOT image using an elliptical gaussian function, (b) CCD image of the MOT, the red and green lines are the longitudinal and transverse axes of the MOT respectively, (a) red data points are the registered counts (proportional to the atomic density) versus pixel number along longitudianal/z-axis of the MOT and black curve is the gaussian fitting along this direction, (c) green data points are the registered counts versus pixel number along transverse/y-axis of the MOT and black curve is the gaussian fit along this axis.

6.2.2 Camera calibration

This section describes the procedure to estimate the value of quantum efficiency coefficient η of the camera, which is a useful quantity to convert the registered pixel counts into number of photons collected. We calibrate the camera by shining a weak laser beam of known power onto the chip and recording the CCD images for different laser power values. Figure 6.4 shows the linear relationship between the registered counts and laser power, and η is calculated using the slope of the linear fit.

$$\eta = \frac{\text{slope} \cdot \text{E}}{t_{\text{exp}}} \approx (2.17 \pm 0.02) \times 10^{-3} \text{ counts/photon} \tag{6.7}$$

where $t_{\text{exp}} = 1038$ μs is the exposure time of the camera and slope=$(8.7 \pm 0.1)\times 10^3$ counts/nW. Here error estimation is carried out from the linear fitting as shown figure 6.4.

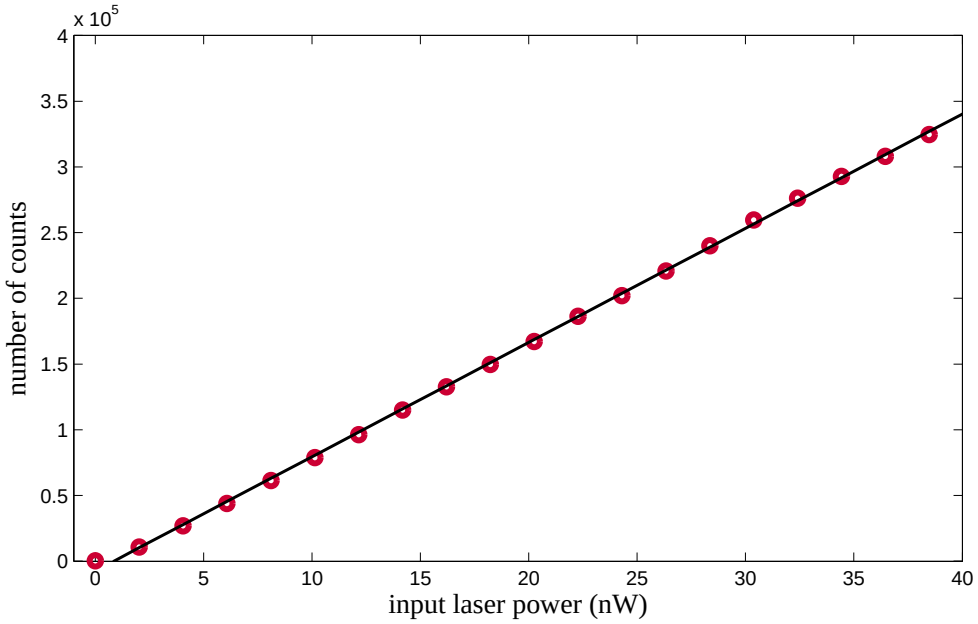

Figure 6.4: This plot shows the linear relationship between the registered pixel counts with respect of power of the laser beam falling on the camera chip. The red circles are the data points and the black line the linear fit of the data giving a slope of $(8.7 \pm 0.1)\times 10^3$ counts/nW

6.2.3 Scattering rate

This section describes the 6 level model used to estimate the scattering rate γ_{sc} of ^{39}K atoms, which is needed to calculate N_{mot} from fluorescence imaging technique.

In potassium, the excited state hyperfine splitting for $P_{3/2}$ state is very small ($\approx$ 34 MHz for ^{39}K) in

comparison to rubidium and cesium (few hundreds of MHz). With cooling laser of frequency ν_1 on (refer to fig-6.5), the atoms should undergo a transition from $F = 2 \rightarrow F' = 3'$. But, in addition to that they can easily jump to wrong excited states ($F' = 1', 2'$) because of narrow excited state splitting. Therefore, optical re-pumping required for potassium is very large in comparison to other alkalis with large excited state splitting. For instance, in case of ^{87}Rb the ratio of repump and cooling laser intensity is ≈1:1000 whereas, for ^{39}K, this is ≈1:1. Due to weak repumping requirements, an atom with large excited state splitting can be treated as a two level system. And, the excited state population for such a simplified system is given by equation-6.8. Here, the presence of weak repump laser has been ignored to calculate excited state fraction ρ_e.

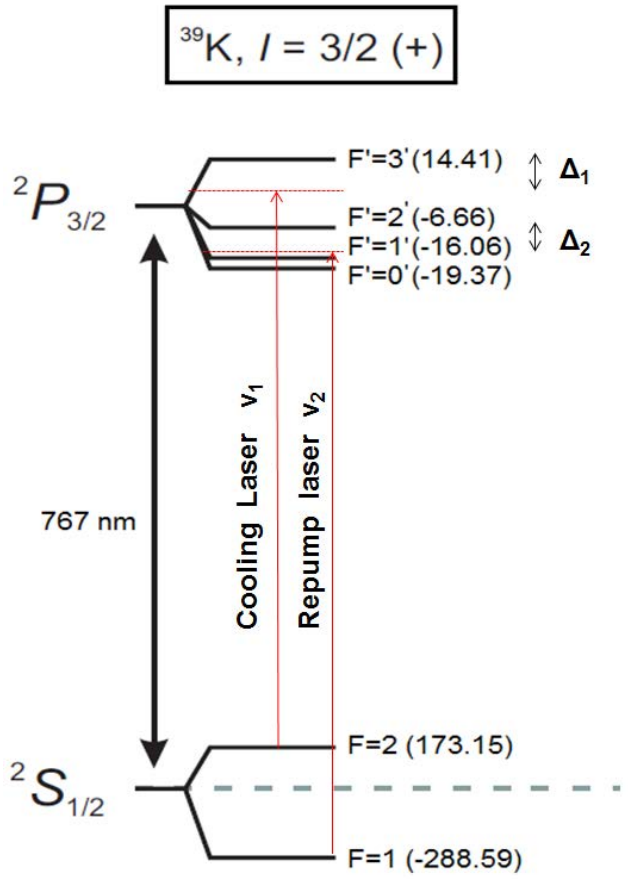

Figure 6.5: The energy level diagram of ^{39}K for D2 transition, where $F = 1, 2$ and $F' = 0' - 3'$ represent the ground and excited state hyperfine levels respectively.

$$\rho_e = \left(\frac{I/I_s}{1 + I/I_s + (2\Delta/\gamma)^2} \right), \tag{6.8}$$

Table 6.1: Various parameters of the MOT and the corresponding values.

Parameter	Value
Measured Detuning	Δ_1=-11.5±1 MHz Δ_2=-2±1 MHz
MOT beam radius	r=3.75 mm
Total MOT intensity	P_{total}=75.0 mW $I_{\text{total}} = 2P_{\text{total}}/(\pi r^2)$=1.7 mW/mm^2
Saturation Intensity I_{s}	I_{s}=3.6 mW/cm^2
Natural linewidth	$\gamma/2\pi$=6.035 MHz

where I is the total intensity of MOT beams, I_{s} is the saturation intensity, Δ is the frequency detuning of the cooling laser from the resonance frequency.

For potassium both cooling and repumping lasers contribute towards the excited state population and hence the scattering rate. Therefore, for an accurate estimate of ρ_e, one needs to use a 6 level model. Figure 6.5 shows the level diagram of ^{39}K, with two ground states $F = 1, 2$ and four excited states, $F' = 0' - 3'$ for potassium D_2 line. The cooling and repump laser frequencies are ν_1 and ν_2 respectively and Δ_1 and Δ_2 are their respective detunings. The cooling and repump frequencies can be written as in following equations.

$$\nu_1 = \nu_{23'} + \Delta_1, \tag{6.9}$$

$$\nu_2 = \nu_{12'} + \Delta_2, \tag{6.10}$$

where $\nu_{FF'}$ corresponds to $F \rightarrow F'$ transition. The populations of all the ground and excited states are calculated using rate equations and 6-level model described in this reference [45]. Table 6.1, gives our MOT parameters, where P_{total} is the total power of all the six MOT beams, the saturation intensity I_{sat} and the natural linewidth γ are for D2 line and referred from [97]. The rate equation for the excited state levels is given by:

$$p_{F'} = R_{F'1}(p_1 - p_{F'}) + R_{F'2}(p_2 - p_{F'}) - p_{F'}, \tag{6.11}$$

where p_1 and p_2 are the lower state populations, $R_{F'F}$ is the excitation rate between ground (F) and excited (F') states and is given by the following equation.

$$R_{F'F} = \frac{C_{F'F}\gamma_{F'F}}{2}\left[\frac{I_F/I_{\text{s}}}{1 + 4(\frac{\nu_F - \nu_{F'F}}{\gamma})^2}\right], \tag{6.12}$$

where $C_{F'F}$ represents clebsch gordan coefficient, $\gamma_{F'F} = b_{F'F}\gamma$, $b_{F'F}$ is the branching ratio from F' to F. All

of the six MOT beams consist of both cooling and repumping laser light. Also, I_1 and I_2 are the intensities of cooling and repump laser beams respectively. For a steady state one can easily find out the upper state populations. The excited state fraction ρ_{e} is given by summing over the normalised populations of all the excited states $p_{F'}$s and is given as following:

$$\rho_e = \sum_F p_{F'}, \tag{6.13}$$

and the scattering rate is given by the following equation.

$$\gamma_{\mathrm{sc}} = \gamma \rho_{\mathrm{e}}. \tag{6.14}$$

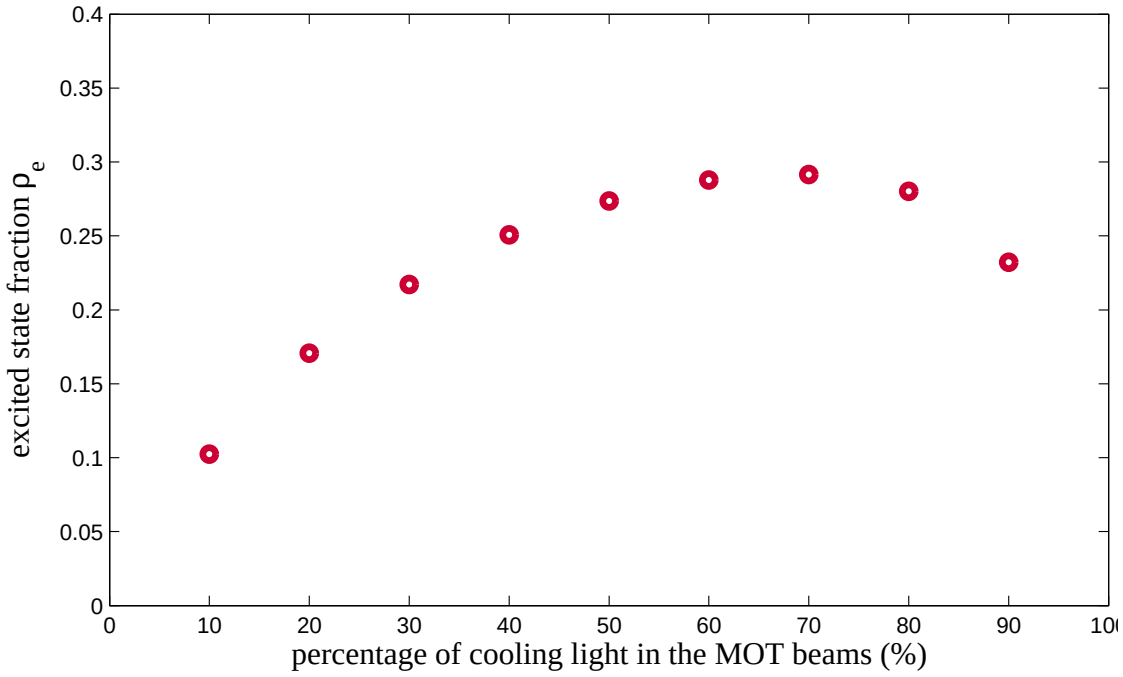

Figure 6.6: The calculated excited state fraction values for different cooling percentage in the MOT beams.

Figure 6.6 shows that ρ_{e} is maximum when repump fraction is 30% of the total intensity of MOT beams. In practice, we have set-up a confocal fabry parot cavity to measure the fractions of cooling and repump intensities in the MOT beams. The MOT atom number calculations in the next section are described for $50:50$ cooling to repump fraction.

6.2.4 Number of Trapped Atoms and density of MOT

The amount of power scattered by the atomic cloud P_{MOT} is directly proportional to atom number N_{mot} inside the MOT. But, the number of photons collected by the camera is only a fraction of the total scattered light by the MOT which is determined by the fractional solid angle $d\Omega$ given by equation 6.3 and exposure time t_{exp}. Hence, the number of photons collected by the camera is given by:

$$N_{\mathrm{camera}} = N_{\mathrm{mot}} d\Omega t_{\mathrm{exp}} \gamma_{\mathrm{sc}}. \tag{6.15}$$

The number of photons estimated from the CCD image of the MOT is given by:

$$N_{\mathrm{camera}} = N_{\mathrm{counts}}/\eta, \tag{6.16}$$

where N_{counts} is the total number of registered pixel counts in the CCD image of the MOT and η, the quantum efficiency constant is given by equation 6.7.

By using equations 6.15 and 6.16 one can estimate the total number of atoms in the MOT and which is given by the following equation.

$$N_{\mathrm{atom}} = N_{\mathrm{count}}/d\Omega\gamma_{\mathrm{p}} t_{\mathrm{exp}} \eta. \tag{6.17}$$

The total number of camera counts N_{count} is calculated by adding all counts of the pixels within the area of the MOT. Using values of all the known parameters, equation 6.17 gives an estimation of the atom number. Here, I describe two different cases to calculate atom number N_{atom} under different conditions.
(a) Lower limit of MOT atom number: If we assume that the intensity of MOT beams is much larger than I_{sat}, in that case the excited state and ground state populations are almost equal. Hence, in this simplified case, we can say that ρ=0.50, which means $\gamma_{\mathrm{sc}} = \frac{1}{2}\gamma$. This gives us the lower limit of the MOT atom number as follows.

$$N_{minimum} = (3.2 \pm 0.1) \times 10^7. \tag{6.18}$$

(b) Estimate of atom number from 6-level model: For our experimental cooling to repump ratio i.e. 1:1, $\gamma_{\mathrm{sc}} = 0.2727\gamma$ described in section 6.2.3. This provides the estimate of actual number of atoms inside our potassium-39 MOT.

$$N_{\mathrm{mot}} = (5.8 \pm 0.3) \times 10^7. \tag{6.19}$$

Now we focus on calculating the density of the MOT. Considering that the atomic density distribution $n(r)$ in a MOT is in accordance with Gaussian distribution, therefore we can write:

$$n_{(\mathrm{x,y,z})} = n_0 e^{-\frac{1}{2}(\frac{x^2}{\sigma_\mathrm{x}^2}+\frac{y^2}{\sigma_\mathrm{y}^2}+\frac{z^2}{\sigma_\mathrm{z}^2})}, \tag{6.20}$$

where n_0 is the peak density of the MOT and can be calculated by integrating this distribution. Here $\sigma_{\mathrm{x,y,z}}$ are the RMS size of the MOT.

$$N_\mathrm{mot} = \int n_{(\mathrm{x,y,z})} d\sigma_\mathrm{x} d\sigma_\mathrm{y} d\sigma_\mathrm{z}, \tag{6.21}$$

which gives,

$$n_0 = \frac{N_\mathrm{mot}}{(2\pi)^{3/2}\sigma_\mathrm{x}\sigma_\mathrm{y}\sigma_\mathrm{z}}. \tag{6.22}$$

Using the values of σ's and N_{mot}, the MOT peak density comes out to be $n_0 = (7.4 \pm 0.2) \times 10^{10}$ atoms/cm^3. The effective number of atoms N_eff is an important parameter to determine the amount of collective strong coupling of atoms with the cavity field. As calculated in the section 1.2.4, its value is given by:

$$N_\mathrm{eff} = 0.03 \times N_\mathrm{mot} \approx (1.75 \pm 0.1) \times 10^6 \mathrm{atoms}. \tag{6.23}$$

Therefore the effective number of atoms in our cavity mode are $\approx 1.75 \times 10^6$, this is much bigger than the minimum atom number required (i.e. 3.3×10^4 atoms) to see the phenomenon of vacuum Rabi splitting in our experiment.

6.3 MOT optimisation

The number of atoms in the MOT as calculated in the previous section can be improved by optimising the MOT with respect to a number of parameters. These parameters include, dispenser's current, detunings of cooling and repump lasers and magnetic field gradient etc. In the present section, I will describe the dependence of MOT atom number on magnetic field gradient and detuning of MOT beams.

6.3.1 B-field optimization

The magnetic field gradient of the MOT can be changed by changing the current through the antihelmholtz rectangular coils. The trends of MOT atom number N_mot, MOT peak density n_0 and effective atom number

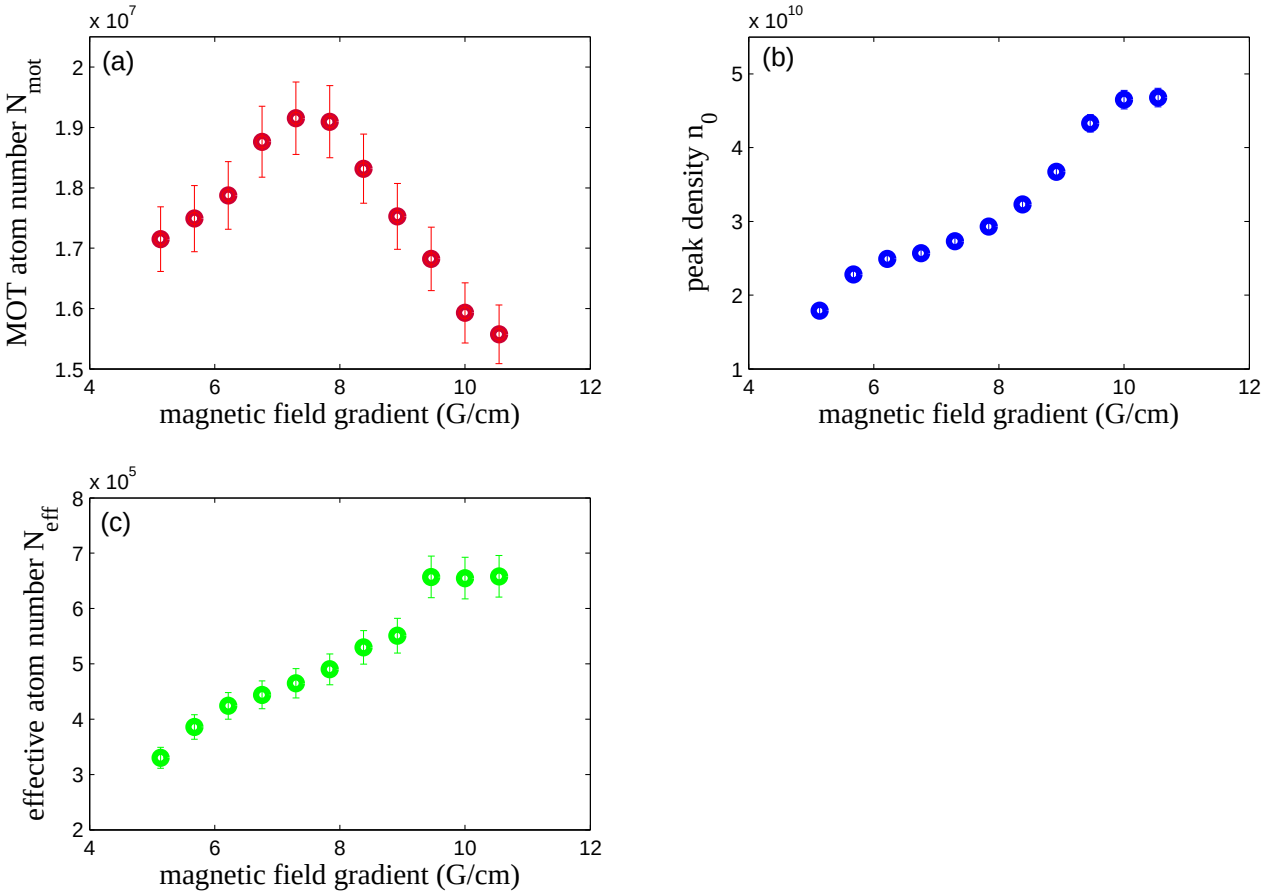

Figure 6.7: The plot of the magnetic field gradient verses (a) total number of atoms in the MOT $N_{\rm mot}$, (b) density of the MOT n_0, and (c) effective number of atoms in the cavity mode $N_{\rm eff}$. This data was taken at cooling and repump detunings of -11±1 MHz and -2±1 MHz respectively and a total intensity of 1.7 mW/mm^2 in the MOT beams. Here error estimations in $N_{\rm mot}$, n_0 and $N_{\rm eff}$ are calculated from uncertainties in measurements of solid angle, MOT dimensions and quantum efficiency.

$N_{\rm eff}$ against the magnetic field gradient is shown in figure 6.7. These graphs illustrate that with increasing gradient, the MOT atom number $N_{\rm mot}$ first increases, becomes maximum for a gradient of 7.6 G/cm which corresponds to a current of 28 A through the coils. After this point the $N_{\rm mot}$ starts decreasing. As expected, the size of MOT decreases along the axes perpendicular to the cavity axis ($\sigma_{\rm x,y}$ decrease and $\sigma_{\rm z}$ is almost constant) with increasing magnetic field gradient. Hence the MOT number decreases after 7.6 G/cm and the density increases linearly all the way up to the maximum achievable gradient of 10.5 G/cm. The $N_{\rm eff}$ first increases linearly for smaller values of gradient and then saturates for a gradient beyond 9.5 G/cm. There are two effects contributing together for this saturation: one is the linear increase in the MOT density and another is decrease in the MOT atom number for large gradients. It is important to note that the MOT size remains almost constant in the elongated direction due to zero gradient along that axis. One can further

increase the MOT density by increasing the magnetic field gradient through increasing the gradient beyond what we can achieve with our current system but the effective atom number will not improve much after 9.5 G/cm of gradient.

6.3.2 Detuning optimisation

To optimise the cooling and repump detunings for large N_{mot} and N_{eff} we first need to find a reference to precisely determine these detunings. The reference point is set by passing a low intensity independent laser beam (near 766.66 nm) through the MOT. This beam is slowly scanned in frequency to find a point where it destroys the MOT completely. The frequency of this reference point corresponds to the cooling transition frequency ($F = 2 \rightarrow F' = 3'$) and is found by detecting its beat note with the cooling laser. Figure 6.8 shows the graphs for the cooling and repump laser detuning versus the MOT atom number N_{mot} and the effective atom number N_{eff}. It is interesting to note that the MOT size and shape changes with detuning variation. For a constant repump detuning of -2 MHz, the MOT atom number and effective atom number peak around -8 MHz and -13 MHz of cooling detunings respectively. Both these parameters peak around -2 MHz of repump detuning for a constant cooling detuning of -11 MHz. As we care the most about having a large N_{eff} in the cavity so the optimised values of cooling and repump detunings are -13 and -2 MHz respectively. The cooling and repump detunings in figure 6.8 refer to their respective VCO's voltages used for frequency offset locks. There is ± 1 MHz frequency uncertainty associated with detuning values because of finite linewidth of our lasers. In addition to this, there is a systematic error in these detuning values due to uncertainty in determining the reference point using beat signal as explained in previous paragraph. Therefore there can be an offset of ± 10 MHz in laser detuning values however the trends shown in figure 6.8 remain the same irrespective of the systematic error in our measurements.

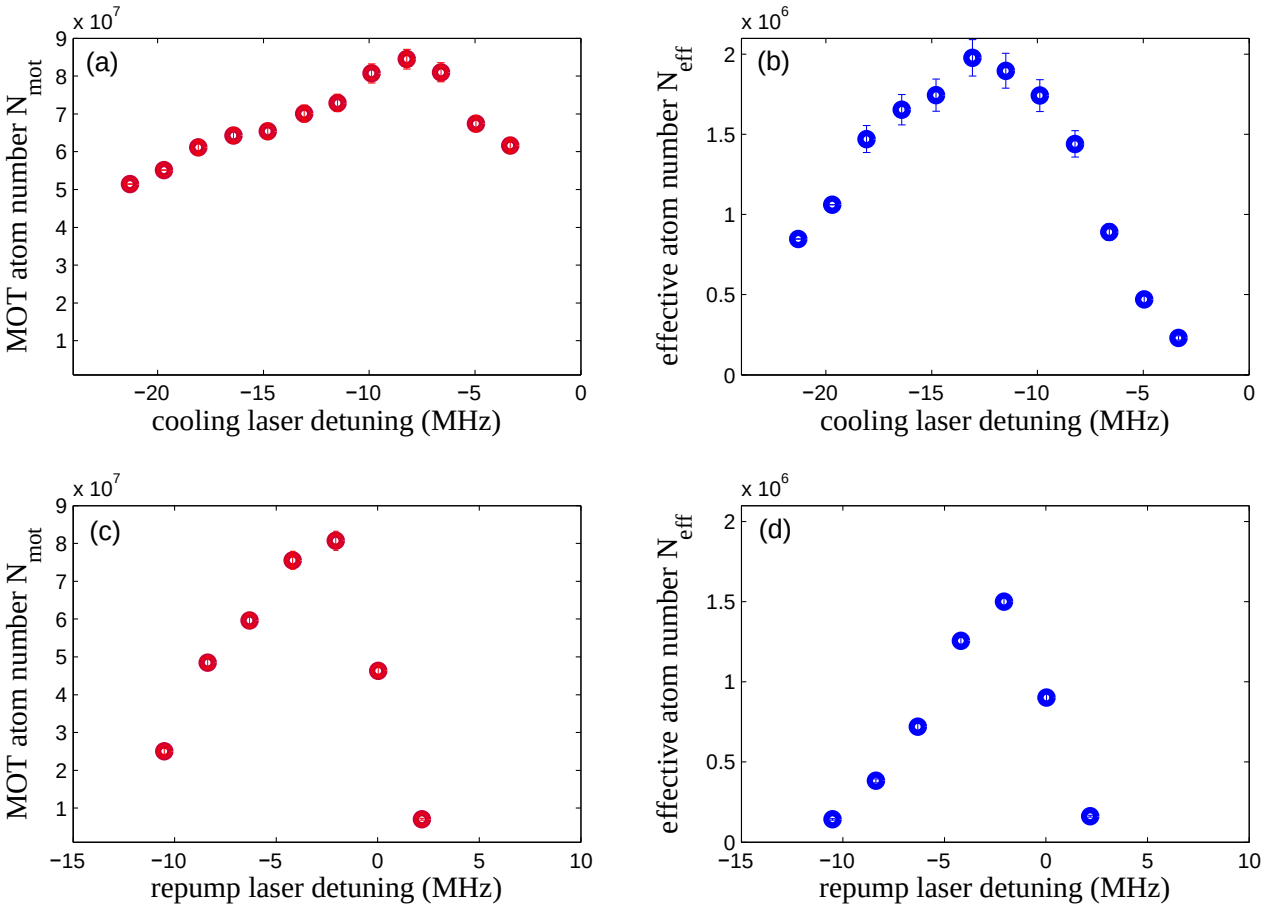

Figure 6.8: Detuning dependence of the MOT atom number N_{mot} and effective atom number N_{eff}. (a) Variation of N_{mot} and (b) N_{eff} with the cooling detuning Δ_1 at a constant repump detuning of $\Delta_2 = -2$ MHz. (c) Variation of N_{mot} and (d) N_{eff} with the repump detuning Δ_2 at a constant cooling detuning of $\Delta_1 = -11$ MHz. This optimisation data was recorded for a total intensity of 1.7 mW/mm^2 in the MOT beams and a magnetic field gradient of 8 G/cm. Here error estimations in N_{mot} and N_{eff} are calculated from uncertainties in measurements of solid angle, MOT dimensions and quantum efficiency.

CHAPTER 7

OUTLOOK

This thesis presented the design and construction of an experiment for the study of strong collective coupling of potassium atoms in a ring cavity. One of the main aims of this experiment is to realise the vacuum Rabi splitting phenomena. A second goal is to study cavity cooling of ^{39}K inside the ring cavity beyond the temperature limit induced by cavity linewidth. The work presented in this thesis has been focused to progress towards fulfilling these goals, especially towards developing and building the MOT laser system, magnetic coil system, MOT imaging system and ultra high vacuum system.

The various spectroscopy methods for the D_2 line of potassium-39 were performed and based on laser locking parameters magnetic dichroism method was chosen to stabilise the master laser. The tapered amplifier system was constructed for the simultaneous amplification of the cooling and repump laser light by a factor of 40. The MOT laser system and ultra-high vacuum system were developed, and potassium atoms were cooled and captured at the center of the ring cavity mode. The imaging system was constructed to analysis and characterise the MOT and we have an effective atom number of the order of $\sim 10^6$ in the cavity mode. The theoretical calculations presented in section 1.2 suggests that these parameters are good enough to realise the vacuum Rabi splitting in the ring cavity. The initial results on experimental observation of the vacuum Rabi splitting are presented in the following section.

7.1 Preliminary results

To observe the atom light interaction in the ring cavity, the cavity needs to be locked and should be resonant with the atomic transition frequency. In addition to this, a probe beam scanning near the atomic resonance is required to be coupled to the cavity. The cavity locking and probing system has been developed, and the ring cavity has been stabilised during the course of this script writing. During the attempts to couple the probe

light into the ring cavity, we found that the cavity mirror M_3 was not glued at the exact position. Therefore, we removed the ring cavity from the vacuum and replaced this flat mirror with a new curved mirror of similar reflectivity. The curved mirror was chosen specifically to allow an alignment degree of freedom as moving a curved mirror (in the plane of the surface to which it is glued) is equivalent to tilting a flat mirror. The cavity was placed back into the vacuum chamber and probe light was successfully coupled into the cavity. The probe beam enters into the cavity from mirror M_3 and the cavity transmission signal (of a few nW) through mirror M_2 is observed on a sensitive photodiode (Laser Components, LCSA500-03).

The first milestone of the experiment has recently been achieved by the non-destructive detection of the vacuum Rabi splitting in our ring cavity. Figure 7.1 shows the plot of cavity normalised transmission signal versus probe frequency detuning from the atomic or cavity resonance ($\delta_{\rm ac}$=0). The probe beam was scanned near $F = 2 \rightarrow F'$ transition. At the time of recording this data, our ring cavity length was not stabilised yet. The cavity resonance was tuned to atomic resonance by tuning cavity length by changing voltage across the piezo stack glued at the back of central mirror. The preliminary analysis gives a Rabi splitting of $\sim 2\pi\times20$ MHz for the cavity linewidth of $\sim 2\pi\times8$ MHz (this is greater than the design linewidth of $2\pi \times 2$ MHz (FWHM). It was widened because of potassium getting stuck to the mirror surfaces). Further analysis and characterization has to be completed yet. The experimental data shows good agreement with theory fits as shown in figure 7.1. The theory curves are plotted using equation 1.26 from chapter-1. These preliminary results prove the existence of collective strong coupling in our atom-cavity system.

7.2 Further improvements and work

7.2.1 Further MOT analysis and characterization

As described in chapter 6, we use florescence imaging method to calculate the MOT atom number $N_{\rm mot} \sim 10^7$, atom density $n \sim 10^{10}$ atoms/cm^3 and effective number of atoms in the cavity mode $N_{\rm eff} \sim 10^6$. The detuning and magnetic field gradient characterisation have been completed as well. Further analysis and characterisation of the MOT are important to be undertaken. We could not do it because we did not have a reliable computer control at that time. Firstly, an analysis should be done to see how the atom number in the cavity mode varies with the varying the ratio of cooling to repump power in the MOT beams. Secondly, the temperature measurements of the MOT are important to be calculated.

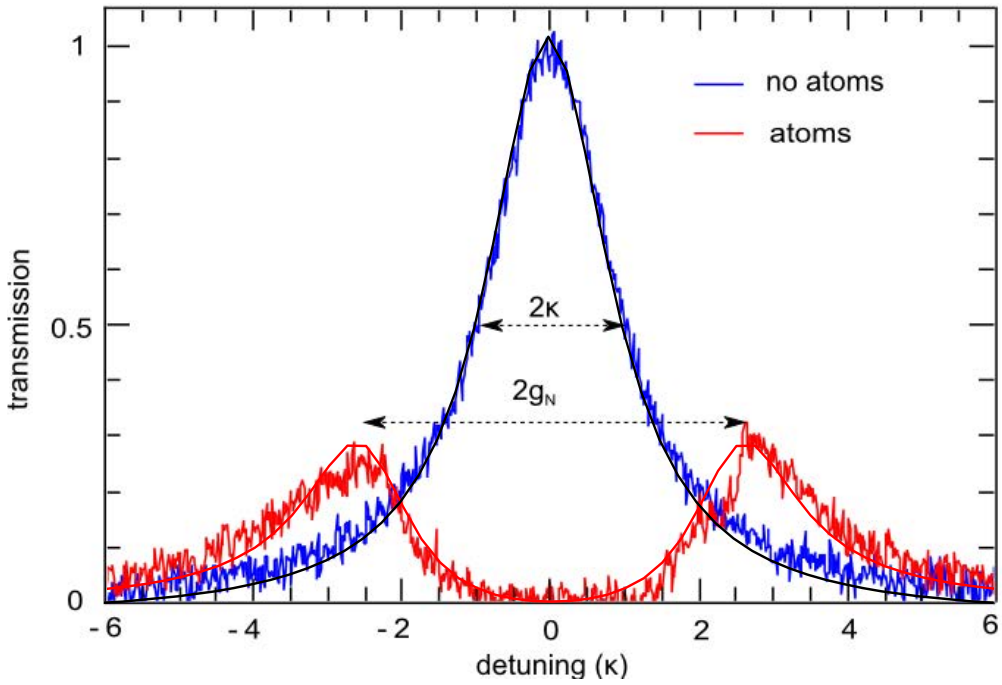

Figure 7.1: The plot of ring cavity transmission signal verses cavity probe beam illustrating the vacuum Rabi splitting. The blue curve is cavity transmission signal without any atoms and this peak gives the cavity linewidth of $\sim 2\pi\times 8$ MHz (FWHM). The red curve is the transmission in the presence of atoms in the cavity waist showing two peaks separated by $\sim 2\pi\times 20$ MHz. Here black (no atoms) and red (with atoms) smooth curves show theory curves fitted to the experimental data.

7.2.2 Elongated MOT

As described in chapter 2, we could achieve a magnetic field gradient of 10.5 G/cm (maximum achievable) using our current coil design. The coil system is capable of providing sufficient magnetic field gradient. However we did not see an elongated MOT with this coil system and discussions with the Du group at Hong Kong university (the idea of this coil system was inspired by their publication [114]) did not elucidate any explanation for this. Recently, we have been able to see an elongated MOT using only one pair of coils (this introduces a small magnetic field gradient along cavity axis) and bigger MOT beams size (∼14 mm). Currently, the effects of beam size and coil geometries are under study to find out why we could not get an elongated MOT with previous magnetic field and beam size parameters.

7.2.3 Introducing a 2D MOT chamber

In the present design of the vacuum system we have only one chamber which consists of the ring cavity. The potassium MOT is made directly at the centre of the cavity mode. This system provides simplicity but there

are a number of improvements which needs to be made. In the present system, the chamber is filled with the potassium gas released by dispensers and the MOT is loaded from a high background pressure. This limits the number of atoms in the MOT and hence in the cavity mode. The second problem which is the major concern for us is that the cavity linewidth increases drastically once the dispensers are on. We believe that this is happening because of potassium atoms sticking to the mirrors surfaces and reducing their reflectivities and hence increasing the cavity linewidth. The cavity linewidth was measured to be $2\pi\times1$ MHz outside the vacuum chamber. It can slowly grow up to $2\pi\times30$ MHz depending on the duration for which it is exposed to the dispensers. In the present situation, it is hard to see a large vacuum Rabi splitting or collective strong coupling for such a large cavity linewidth. We tried taking the cavity out of the vacuum to clean the mirrors surfaces. However, because of design constraints of the cavity frame, it is extremely hard to clean the them without removing from the cavity frame. The next plan is to connect a 2D MOT chamber to the present chamber using a narrow nipple and a valve. A 2D MOT [26] will be made in the new 2D MOT chamber. The atoms will be pushed into the already existing main chamber using a pushing beam and a 3D MOT will be formed inside the ring cavity. In this way, the main chamber would not be directly exposed to the dispensers and there will be relatively less potassium in the background. This will save the cavity mirrors from getting dirty and maintain a decent value of cavity linewidth.

7.2.4 Modifications in the ring cavity design

For the further experiments, we also need to modify the design of the ring cavity. In the present design, the mirrors are directly glued into the grooves on the cavity frame and there is no room to clean the mirror surfaces without removing them from the frame. In the next generation of the cavity design there will be a couple of improvements over the old version and these are stated below:

1. All mirrors will be attached directly to steel surfaces, which will be machined in a single shot. This will make them easier to position, easier to remove, and will give them good thermal contact to the frame which will be heated through the flange to try to keep background potassium atoms from sticking.

2. It will be mounted inside the science chamber in such a way that the cavity mirrors will not be directly facing the atomic beam. This will help protecting the mirrors from potassium.

3. There will be more optical access to have bigger sized MOT beams (not just holes for the MOT beams.

4. Unlike the old design, it will be possible to clean all mirror surfaces without removing any mirrors.

7.3 Future Goals of the Experiment

Long term goal of the present experiment is to build a ring laser. The initial work in this direction will permit the study of electromagnetically induced transparency (EIT) [12, 61] in a ring cavity. The phenomenon of EIT is based on making the atomic medium transparent to electromagnetic radiation in a small window of an atomic transition line. Within the transparency window the intracavity refractive index of the medium can be tuned to two different regimes: *slow light regime* and *fast light regime*. In the slow light regime, the group refractive index of the medium inside the cavity is made large which corresponds to a small group velocity. This can potentially act as an active optical clock [18, 19, 104] with high insensitivity to mechanical and thermal noise of the laser cavity.

In the fast light regime, the group index of the medium is made vanishingly small corresponding to a very large group velocity. The laser frequency in this regime becomes extremely sensitive to rotations through large Sagnac effect. Our experiment will focus on making a superluminal ring laser [85] in this regime which will act as a very precise Gyroscope (a rotational sensor for navigations).

The setup realised in this thesis is so versatile that it opens up many interesting path ways including observing Bloch oscillation in a cavity for precision metrology, and realisation of quantum qubits which are fundamental building block for a quantum computer and quantum information.

APPENDIX A

A.1 Radia code for magnetic field simulations

In this appendix, the Radia software code is given which simulates our rectangular magnetic field coil system to estimate the geometry and magnetic field gradients as shown in figures 2.7 and 2.8. This script is written to achieve a magnetic field gradient of 8-10 G/cm with $I * N = 1200$ amp-turns. Here we consider that each of the four rectangular coils has single turn and 1200 A of current flowing through it. This system is similar to having 40 turns and 30 A of current. The current density of the system is j=8.6 A/mm^2 where cross sectional area for each coil is assumed to be 14×10 mm^2 (a coil forty turns of copper strap (14 mm×0.25 mm) has the same cross-sectional area). In the following code, bold text lines refer to the code and plain text lines are comments.

RadUtiMem[];

j=8.6; (*Current density in amp-turns/mm^2*)

(*Important parameters for coil presentation *)

nQ=16; (*No. of bends in each coil corner*)

cQ=1,0,0; (*Centre of the top coil*)

thcn=0.001;

(*Creating rectangular coils (all lengths in mm)*)

a=316; (*Length along y-axis*)

b=156; (*Length along x-axis*)

t1=10; (*Thickness of the 40 turns*)

```
t2=14;      (*Width of the copper strip*)
d1=184;     (*Coil separation along vertical direction*)
d2=184;     (*Coil separation in horizontal direction*)

Q1=radObjRaceTrk[{0.,0.,(d2+t2)/2},{0,t1},{b,a},t,nQ,j,"man","z"];
radObjDrwAtr[Q1,cQ,thcn];      (*Coil 1*)
Q2=radObjRaceTrk[{0.,0.,-(d2+t2)/2},{0,t1},{b,a},t,nQ,-j,"man","z"];
radObjDrwAtr[Q2,cQ,thcn];      (*Coil 2*)
Q3=radObjRaceTrk[{(d1+t2)/2,0.,0.},{0,t1},{a,b},t,nQ,-j,"man","x"];
radObjDrwAtr[Q3,cQ,thcn];      (*Coil 3*)
Q4=radObjRaceTrk[{-(d1+t2)/2,0.,0.},{0,t1},{a,b},t,nQ,j,"man","x"];
radObjDrwAtr[Q4,cQ,thcn];      (*Coil 4*)

(*Grouping together the above coils*)
Grp=radObjCnt[{Q1,Q2,Q3,Q4}];

(*Displaying the geometry*)
RadPlot3DOptions[];     (*Some options for plotting*)

dr=radObjDrw[Grp]; (*Saving the geometry in "dr"*)

(*Drawing the geometry of the grouped coils*)
Show[Graphics3D[dr,PlotLabel→ "SCW",BaseStyle → {14, FontFamily → "Times"}]]

(*Plotting the magnetic field in three cartesian axes and its contour plot*)
RadPlotOptions[];
Plot[{10^4*radFld[Grp,"Bz",{0,0,z}]},{z,-10,10},AxesOrigin→ {0,0},FrameLabel→ {"x [mm]","Bx
[G]","Y = Z = 0"," "}]
Plot[{10^4*radFld[Grp,"Bx",{x,0,0}]},{x,-10,10},AxesOrigin→ {0,0},FrameLabel→ {"y [mm]","By
[G]","X = Z = 0"," "}]
Plot[{10^4*(radFld[Grp,"Bx",{0,y,0}]^2+radFld[Grp,"By",{0,y,0}]^2+radFld[Grp,"Bz"
```

,{0,y,0}]^2)$^{1/2}$},{y,-10,10},AxesOrigin→0,0,FrameLabel→ {"z [mm]","B[G]","X = Y = 0"," "}]

ContourPlot[{10^4*(radFld[Grp,"Bx",{x,0,z}]^2+radFld[Grp,"By",{x,0,z}]^2+radFld[Grp,"Bz"

,{x,0,z}]^2)$^{1/2}$,{z,-50,50},{x,-50,50},Contours→Table[10 i,{i,0,15}] ,AxesOrigin→0,0

,ContourShading→True,FrameLabel→"y [mm]","x [mm]","B [G]"," "]

10^4∗(radFld[Grp,"Bx",{1,0,0}]^2+radFld[Grp,"By",{1,0,0}]^2+radFld[Grp,"Bz",{1,0,0}]^2)$^{1/2}$G/mm

(*Magnitude of the gradient along x-axis*)

10^4∗(radFld[Grp,"Bx",{0,1,0}]^2+radFld[Grp,"By",{0,1,0}]^2+radFld[Grp,"Bz",{0,1,0}]^2)$^{1/2}$G/mm

(*Magnitude of the gradient along y-axis*)

10^4∗(radFld[Grp,"Bx",{0,0,1}]^2+radFld[Grp,"By",{0,0,1}]^2+radFld[Grp,"Bz",{0,0,1}]^2)$^{1/2}$G/mm

(*Magnitude of the gradient along z-axis*)

LIST OF REFERENCES

[1] G S Agarwal. Spectroscopy of strongly coupled atom-cavity systems: a topical review. *Journal of Modern Optics*, 45(3):449–470, 1998.

[2] K J Arnold, M P Baden, and M D Barrett. Self-organization threshold scaling for thermal atoms coupled to a cavity. *Phys. Rev. Lett.*, 109:153002, 2012.

[3] H A Bachor and T C Ralph. *A guide to experiments in quantum optics*. Wiley-Vch Verlag GmbH & Co. KGaA, 2003.

[4] J F Barry, D J McCarron, E B Norrgard, M H Steinecker, and D DeMille. Magneto-optical trapping of a diatomic molecule. *Nature*, 512:286289, 2014.

[5] P R Berman and V S Malinovsky. *Principles of Laser Spectroscopy and Quantum Optics*. Princeton University Press, 2011.

[6] F Bernardot, P Nussenzveig, M Brune, J M Raimond, and S Haroche. Vacuum rabi splitting observed on a microscopic atomic sample in a microwave cavity. *Europhysics Letters*, 17:33, 1992.

[7] S Bernon. *Trapping and nondemolition measurement of cold atoms in a high-finesse ring cavity*. PhD thesis, Laboratoire Charles Fabry Institut dOptique Graduate School, April 5, 2011.

[8] K M Birnbaum. *Cavity QED with Multilevel Atoms*. PhD thesis, California Institute of Technology, Pasadena, California, 2005.

[9] G C Bjorklund. Frequency-modulation spectroscopy: a new method for measuring weak absorptions and dispersions. *Opt. Lett.*, 5:15–17, 1980.

[10] A T Black, H W Chan, and V Vuletic. Observation of collective friction forces due to spatial self-organization of atoms: From rayleigh to bragg scattering. *Phys. Rev. Lett.*, 91:203001, 2003.

[11] E D Black. An introduction to pound drever hall laser frequency stabilization. *American Journal of Physics*, 69(1):79–87, 2001.

[12] K J Boller, A Imamoglu, and S E Harris. Observation of electromagnetically induced transparency. *Phys. Rev. Lett.*, 66, 1991.

[13] V P Itkin C B Alcock and M K Horrigan. Vapor pressure equations for the metallic elements: 298-2500k. *Canadian Metallurgical Quarterly*, 23:309–13, 1984.

[14] H J Carmichael. *Statistical Methods in Quantum Optics 1.* Springer Verlag, 1999.

[15] L G Carpenter. *Vacuum Technology, 2nd Edition.* Hilger, 1970.

[16] A Chambers, R K Fitch, and B S Halliday. *Basic Vacuum Technology.* Institute of Physics, 1998.

[17] H W Chan, A T Black, and V Vuletic. Observation of collective-emission-induced cooling of atoms in an optical cavity. *Phys. Rev. Lett.*, 90:063003, 2003.

[18] J B Chen. Active optical clock. *Chin Sci Bull*, 54, 2009.

[19] J B Chen and X Z Chen. Optical lattice laser. *Proceedings of International Frequency Control Symposium, Vancouver, Washington DC*, 54, 2005.

[20] S Chu, L Hollberg, J E Bjorkholm, A Cable, and A Ashkin. Three-dimensional viscous confinement and cooling of atoms by resonance radiation pressure. *Phys. Rev. Lett.*, 55:48–51, 1985.

[21] P W Courteille, C von Cube, B Deh, D Kruse, A Ludewig, S Slama, and C Zimmermann. The collective atomic recoil laser. *AIP Conference Proceedings*, 770:135–143, 2005.

[22] G Mller D Meschede, H Walther. One-atom maser. *Physical review letters*, 1985.

[23] J Dalibard and C Cohen-Tannoudji. Laser cooling below the doppler limit by polarization gradients: simple theoretical models. *J. Opt. Soc. Am. B*, 6:2023–2045, 1989.

[24] W Demtroder. *Laser Spectroscopy 2nd edn.* Berlin:Springer, 1998.

[25] R H Dicke. Coherence in spontaneous radiation processes. *Phys. Rev.*, 93:99–110, 1954.

[26] K Dieckmann, R J C Spreeuw, M Weidemuller, and J T M Walraven. Two-dimensional magneto-optical trap as a source of slow atoms. *Phys. Rev. A*, 58:3891–3895, 1998.

[27] M Ducloy and D Bloch. Theory of degenerate four-wave mixing in resonant doppler-broadened media, doppler-free heterodyne spectroscopy via collinear four-wave mixing in two- and three-level systems. *J. Physique*, 43:57–65, 1982.

[28] T Elsasser, B Nagorny, and A Hemmerich. Optical bistability and collective behavior of atoms trapped in a high q ring cavity. *Phys. Rev. A*, 69:033403, 2004.

[29] S Falke, E Tiemann, C Lisdat, H Schnatz, and G Grosche. Transition frequencies of the d lines of ^{39}K, ^{40}K, and ^{41}K measured with a femtosecond laser frequency comb. *Phys. Rev. A*, 74:032503, 2006.

[30] C J Foot. *Atomic Physcis.* Oxford University Press), year = 2005, pages = 178-194.

[31] K M Fortier, S Y Kim, M J Gibbons, P Ahmadi, and M S Chapman. Deterministic loading of individual atoms to a high-finesse optical cavity. *Phys. Rev. Lett.*, 98:233601, 2007.

[32] M Fuchs. Development of a high power stabilized diode laser system. Master's thesis, University of Oregon, June, 2006.

[33] M Gangl and H Ritsch. Cold atoms in a high q ring cavity. *Phys. Rev. A*, 61:043405, 2000.

[34] J M Goldwin. *Quantum Degeneracy and Interactions in the 87Rb -40K Bose-Fermi Mixture.* PhD thesis, Graduate School of the University of Colorado, 2005.

[35] A Griessner, D Jaksch, and P Zoller. Cavity-assisted nondestructive laser cooling of atomic qubits. *Journal of Physics B: Atomic, Molecular and Optical Physics*, 37:1419, 2004.

[36] T W Hansch, M D Levenson, and A L Schawlow. Complete hyperfine structure of a molecular iodine line. *Phys. Rev. Lett.*, 26:946–949, 1971.

[37] T W Hansch and A L Schawlow. Cooling of gases by laser radiation. *Opt. Comm.*, 13:68–71, 1975.

[38] M L Harris, C S Adams, S L Cornish, I C McLeod, E Tarleton, and I G Hughes. Polarization spectroscopy in rubidium and cesium. *Phys. Rev. A*, 73:8, 2006.

[39] M L Harris, S L Cornish, A Tripathi, and I G Hughes. Optimization of sub-doppler davll on the rubidium d2 line. *Journal of Physics B: Atomic, Molecular and Optical Physics*, 41(8):085401, 2008.

[40] D J Heinzen, J J Childs, J E Thomas, and M S Feld. Enhanced and inhibited visible spontaneous emission by atoms in a confocal resonator. *Phys. Rev. Lett.*, 58:2153–2153, 1987.

[41] W C Hilton, V Vladan, and T B Adam. Cooling of cesium atoms by collective emission inside an optical resonator. pages 91–98.

[42] C J Hood, M S Chapman, T W Lynn, and H J Kimble. Real-time cavity qed with single atoms. *Phys. Rev. Lett.*, 80:4157–4160, 1998.

[43] P Horak, G Hechenblaikner, K M Gheri, H Stecher, and H Ritsch. Cavity-induced atom cooling in the strong coupling regime. *Phys. Rev. Lett.*, 79:4974–4977, 1997.

[44] M Hummon, M Yeo, B Stuhl, A Collopy, Y Xia, and J Ye. 2d magneto-optical trapping of diatomic molecules. *Physical Review Letters*, 110(14):143001+, 2013.

[45] R S Williamson III. *Magneto-optical trapping of potassium isotopes.* PhD thesis, Uuniversity of Wisconsin, Madison, 1997.

[46] E T Jaynes and F W Cummings. Comparison of quantum and semiclassical radiation theories with application to the beam maser. *Proceedings of the IEEE*, 51:89–109, 1963.

[47] W Jhe, A Anderson, E A Hinds, D Meschede, L Moi, and S Haroche. Suppression of spontaneous decay at optical frequencies: Test of vacuum-field anisotropy in confined space. *Phys. Rev. Lett.*, 58:666–669, 1987.

[48] Y Kaluzny, P Goy, M Gross, J M Raimond, and S Haroche. Observation of self-induced rabi oscillations in two-level atoms excited inside a resonant cavity: The ringing regime of superradiance. *Phys. Rev. Lett.*, 1983.

[49] J Kangara. Design and construction of tapered amplifier systems for laser cooling and atom trapping experiments. Master's thesis, Miami University, Oxford, Ohio, 2012.

[50] L C Kristan, L Zheng-Tian, F H Carter, J E Ryan, and E W Carl. Frequency-stabilized diode laser with the zeeman shift in an atomic vapor. *Appl. Opt.*, 37:3295–3298, 1998.

[51] D R Leibrandt, J Labaziewicz, V Vuletic, and I L Chuang. Cavity sideband cooling of a single trapped ion. *Phys. Rev. Lett.*, 103:103001, 2009.

[52] V S Letokhov. *Laser Control of Atoms and Molecules.* Oxford University Press, 2007.

[53] M Lewenstein and L Roso. Cooling of atoms in colored vacua. *Phys. Rev. A*, 47:3385–3389, 1993.

[54] Y W Lin, H C Chou, P P Dwivedi, Y C Chen, and Yu I A. Using a pair of rectangular coils in the mot for the production of cold atom clouds with large optical density. *Opt. Express*, 16:3753–3761, 2008.

[55] H Mabuchi and A C Doherty. Cavity quantum electrodynamics: Coherence in context. *Science*, 298(5597):1372–1377, 2002.

[56] P Maunz, T Puppe, I Schuster, N Syassen, P W H Pinkse, and G Rempe. Cavity cooling of a single atom. *Nature*, 428:1098–1130, 2004.

[57] P L W Maunz. *Cavity cooling and spectroscopy of a bound atomcavity system.* PhD thesis, Technische Universität at München, MPQ, 2005.

[58] D J McCarron, S A King, and S L Cornish. Modulation transfer spectroscopy in atomic rubidium. *Measurement Science and Technology*, 19(10):105601, 2008.

[59] H J Metcalf and P Straten. *Laser Cooling and Trapping.* Springer-Verlag, 1999.

[60] T W Mossberg, M Lewenstein, and D J Gauthier. Trapping and cooling of atoms in a vacuum perturbed in a frequency-dependent manner. *Phys. Rev. Lett.*, 67:1723–1726, 1991.

[61] M Mucke, E Figueroa, J Bochmann, C Hahn, K Murr, S Ritter, C J Villas-Boas, and G Rempe. Electromagnetically induced transparency with single atoms in a cavity. *Nature*, 465, 2010.

[62] L Mudarikwa. PhD thesis, Midlands Ultra-cold Atom Research Center, The University of Birmingham, To be submitted yet.

[63] L Mudarikwa, K Pahwa, and J Goldwin. Sub-doppler modulation spectroscopy of potassium for laser stabilization. *Journal of Physics B: Atomic, Molecular and Optical Physics*, 45:065002, 2012.

[64] V Negnevitsky. Modulation transfer spectroscopy for fast, accurate laser stabilisation, 2009.

[65] H Noh, S E Park, L Z Li, J Park, and C Cho. Modulation transfer spectroscopy for 87rb atoms: theory and experiment. *Opt. Express*, 19:23444–23452, 2011.

[66] S Nubmann, M Hijlkema, B Weber, F Rohde, G Rempe, and A Kuhn. Submicron positioning of single atoms in a microcavity. *Phys. Rev. Lett.*, 95:173602, 2005.

[67] S Nubmann, K Murr, M Hijlkema, B Weber, A Kuhn, and G Rempe. Vacuum-stimulated cooling of single atoms in three dimensions. *Nature Physics*, 1:122, 2005.

[68] J F O'Hanlon. *A User's Guide to Vacuum Technology, 2nd Edition.* Wiley, 1988.

[69] K Pahwa, L Mudarikwa, and J Goldwin. Polarization spectroscopy and magnetically-induced dichroism of the potassium d2 lines. *Opt. Express*, 20:17456–17466, Jul 2012.

[70] S B Papp. *Experiments with a two-species Bose-Einstein condensate utilizing widely tunable interparticle interactions.* PhD thesis, University of Colorado, Boulder, 2001.

[71] P G Pappas, M M Burns, D D Hinshelwood, M S Feld, and D E Murnick. Saturation spectroscopy with laser optical pumping in atomic barium. *Phys. Rev. A*, 21:1955–1968, 1980.

[72] C P Pearman, C S Adams, S G Cox, P F Griffin, D A Smith, and I G Hughes. Polarization spectroscopy of a closed atomic transition: applications to laser frequency locking. *Journal of Physics B: Atomic, Molecular and Optical Physics*, 35:5141, 2002.

[73] T Petelski, M Fattori, G Lamporesi, J Stuhler, and G M Tino. Doppler-free spectroscopy using magnetically induced dichroism of atomic vapor: a new scheme for laser frequency locking. *Eur. Phys. J. D*, 22(2):279–283, 2003.

[74] D Peter and R Helmut. Mechanical effects of light in optical resonators. *J. Opt. Soc. Am. B*, 20:1098–1130, May 2003.

[75] P Phoonthong. *State-insensitive traps for caesium atoms.* PhD thesis, University College London, 2012.

[76] M Pichler and D C Hall. Simple laser frequency locking based on doppler-free magnetically induced dichroism. *Optics Communications*, 28:50 – 53, 2012.

[77] E M Purcell. Spontaneous emission probabilities at radio frequencies. 340:839–839, 1995.

[78] E L Raab, M Prentiss, A Cable, S Chu, and D E Pritchard. Trapping of neutral sodium atoms with radiation pressure. *Phys. Rev. Lett.*, 59:2631–2634, 1987.

[79] J M Raimond, P Goy, M Gross, C Fabre, and S Haroche. Collective absorption of blackbody radiation by rydberg atoms in a cavity: An experiment on bose statistics and brownian motion. *Phys. Rev. Lett.*, 49:117, 1982.

[80] M G Raizen, R J Thompson, R J Brecha, H J Kimble, and H J Carmichael. Normal-mode splitting and linewidth averaging for two-state atoms in an optical cavity. *Physical review letters*, 63:63, 1989.

[81] G Ritt, G Cennini, C Geckeler, and M Weitz. Laser frequency offset locking using a side of filter technique. *Applied Physics B*, 79(3):363–365, 2004.

[82] N P Robins, B J J Slagmolen, D A Shaddock, J D Close, and M B Gray. Interferometric, modulation-free laser stabilization. *Opt. Lett.*, 27(21):1905–1907, 2002.

[83] A Roth. *Vacuum Technology.* Elsevier Science B.V., Amsterdam, 1990.

[84] R J Schulze, C Genes, and H Ritsch. Optomechanical approach to cooling of small polarizable particles in a strongly pumped ring cavity. *Phys. Rev. A*, 81:063820, 2010.

[85] M S Shahriar, G S Pati, R Tripathi, V Gopal, M Messall, and K Salit. Ultrahigh precision absolute and relative rotation sensing using fast and slow light. *Physical Review A*, 75, 2007.

[86] Z Shanchao, J F Chen, C Liu, S Zhou, M M T Loy, G K L Wong, and S Du. A dark-line two-dimensional magneto-optical trap of 85rb atoms with high optical depth. *Review of Scientific Instruments*, 83, 2012.

[87] J H Shirley. Modulation transfer processes in optical heterodyne saturation spectroscopy. *Opt. Lett.*, 7:537–539, 1982.

[88] S Slama, S Bux, G Krenz, C Zimmermann, and P W Courteille. Superradiant rayleigh scattering and collective atomic recoil lasing in a ring cavity. *Phys. Rev. Lett.*, 98:053603, 2007.

[89] D A Smith and I G Hughes. The role of hyperfine pumping in multilevel systems exhibiting saturated absorption", journal = American Journal of Physics, year = 2004, volume = 72, number = 5, pages = 631-637.

[90] J J Snyder, R K Raj, D Bloch, and M Ducloy. High-sensitivity nonlinear spectroscopy using a frequency-offset pump. *Opt. Lett.*, 5(4):163–165, 1980.

[91] V Stert and R Fischer. Doppler-free polarization spectroscopy using linear polarized light. *Applied Physics*, 17:151–154, 1978.

[92] G W Series T W Hnsch, A L Schawlow. The spectrum of atomic hydrogen. *Scientific American*, 240, 1979.

[93] M Tavis and F W Cummings. Exact solution for moleculeradiation-field hamiltonian. *Phys. Rev.*, 170:379–384, 1968.

[94] M Tavis and F W Cummings. Approximate solutions for an n-molecule-radiation-field hamiltonian. *Phys. Rev.*, 188:692–695, 1969.

[95] R J Thompson, G Rempe, and R J Kimble. Observation of normal-mode splitting for an atom in an optical cavity. *Physical review letters*, 68:1132, 1992.

[96] T G Tiecke. Properties of potassium. 2010.

[97] T G Tiecke. *Properties of Potassium.* PhD thesis, An Der Waals-Zeeman institute, University of Amsterdam, 2010.

[98] V B Tiwari, S Singh, S R Mishra, H S Rawat, and S C Mehendale. Laser frequency stabilization using doppler-free bi-polarization spectroscopy. *Optics Communications*, 263(2):249 – 255, 2006.

[99] J-A Kim U Shim and W Jhe. Frequency-stabilized diode laser with the zeeman shift in an atomic vapor. *J. Kor. Phys. Soc.*, 35:222225, May 1999.

[100] A Vukics and P Domokos. Simultaneous cooling and trapping of atoms by a single cavity-field mode. *Phys. Rev. A*, 72:031401, 2005.

[101] A Vukics, W Niedenzu, and H Ritsch. Cavity nonlinear optics with few photons and ultracold quantum particles. *Phys. Rev. A*, 79:013828, 2009.

[102] V VuletiC and S Chu. Laser cooling of atoms, ions, or molecules by coherent scattering. *Phys. Rev. Lett.*, 84:3787–3790, 2000.

[103] H Walther. Experiments on cavity quantum electrodynamics. *Physics Reports*, 219(36):263 – 281, 1992.

[104] H Wang, P L Gould, and W C Stwalley. Long-range interaction of the 39k(4s)+39k(4p) asymptote by photoassociative spectroscopy. i. the 0g pure long-range state and the long-range potential constants. *The Journal of Chemical Physics", year = 1997, volume = 106, pages = 7899-7912.*

[105] G Wasik, W Gawlik, J Zachorowski, and W Zawadzki. Laser frequency stabilization by doppler-free magnetic dichroism. *Applied Physics B: Lasers and Optics*, 75:613–619, 2002.

[106] F Wei, D Chen, Z Fang, H Cai, and R Qu. Modulation-free frequency stabilization of external-cavity diode laser based on a phase-difference biased sagnac interferometer. *Opt. Lett.*, 35:3853–3855, 2010.

[107] A Wickenbrock, M Hemmerling, G R M Robb, C Emary, and F Renzoni. Collective strong coupling in multimode cavity qed. *Phys. Rev. A*, 87:043817, 2013.

[108] A Wickenbrock, P Phoonthong, and F Renzoni. Collective strong coupling in a lossy optical cavity. *Journal of Modern Optics*, 58:1310–1316, 2011.

[109] C Wieman and T W Hansch. Doppler-free laser polarization spectroscopy. *Phys. Rev. Lett.*, 36:1170–1173, May 1976.

[110] C E Wieman and L Hollberg. Using diode lasers for atomic physics. *Rev. Sci. Instrum.*, 62, 1991.

[111] D Wineland and H Delhmelt. Proposed $10^{14}\delta\nu/\nu$ laser fluorescence spectroscopy on tl^+ mono-ion oscillator. *Bull.Am.Phys.Soc.*, 20:637, 1975.

[112] D J Wineland and W M Itano. Laser cooling of atoms. *Phys. Rev. A*, 20:1521–1540, 1979.

[113] M Wolke, J Klinner, H Kebler, and A Hemmerich. Cavity cooling below the recoil limit. 337(6090):75–78, 2012.

[114] J Zhang, D Wei, C Xie, and D Peng. Characteristics of absorption and dispersion for rubidium d2 lines with the modulation transfer spectrum. *Opt. Express*, 11:1338–1344, 2003.